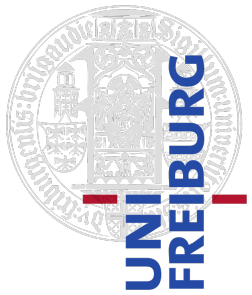

Interactions between metallic impurities and extended defects in silicon from first-principles

by

Robert-Alexander Benedikt-Vincent Ziebarth

Submitted to the Faculty of Mathematics and Physics
of the Albert-Ludwigs-Universität
Freiburg im Breisgau
in partial fulfillment of the requirements
for the degree of a

Doctor rerum naturalium

Dekan:	Prof. Dr. Kröner
Erstgutachter:	Prof. Dr. Elsässer
Zweitgutachter:	Prof. Dr. Schumacher
Datum der mündlichen Prüfung:	18.01.2016

Zusammenfassung

In der hier vorliegenden Dissertation werden metallische Verunreinigungen in polykristallinem Photovoltaik-Silizium mit quantenmechanischen First-Principles-Methoden studiert. Dafür werden Eisen und Natrium als unterschiedliche Vertreter-Elemente ausgewählt und untersucht.

Heutzutage werden siliziumbasierte Solarzellen vorwiegend aus kostengünstigem polykristallinem Silizium hergestellt, welches sowohl eine hohe Konzentration von Fremdatomen als auch eine große Dichte von ausgedehnten Defekten, beispielsweise Korngrenzen oder Versetzungen, beinhaltet. Seit langer Zeit ist bekannt, dass vor allem Eisenverunreinigungen zu hohen Effizienzverlusten in siliziumbasierten Solarzellen führen. Eisenatome wechselwirken mit ausgedehnten Defekten im Silizium, was zur Einlagerung von Eisenatomen führen kann. Diese Einlagerung ändert die elektronischen Eigenschaften der ausgedehnten Defekte. Ziel des ersten Teils der Arbeit ist es, diese Wechselwirkungen in drei unterschiedlichen Szenarien besser zu verstehen. Dazu werden mithilfe atomistischer Simulationen die Wirkung von Großwinkelkorngrenzen, mechanischen Spannungs- bzw. Dehnungsfeldern und Versetzungen mit Eisenverunreinigungen untersucht. Dabei stellt sich heraus, dass mechanische Dehnungsfelder nicht zu einer Anhäufung von Eisenatomen in bestimmten Bereichen führen, jedoch deren Diffusion maßgeblich beeinflussen. Im Gegensatz dazu zeigt sich, dass nur in manchen Großwinkelkorngrenzen eine Einlagerung von Eisenatomen möglich ist. Bei allen in dieser Arbeit betrachteten Versetzungskernen kommt es zu einer Einlagerung von Eisen. Es zeigt sich insgesamt, dass eingelagertes Eisen die elektrischen Eigenschaften der ausgedehnten Defekte stark beeinflusst.

Der zweite Teil der Arbeit befasst sich mit der kürzlich entdeckten Potential-induzierten Degradation von Solarzellen und den in diesem Zusammenhang auftretenden Natrium-dekorierten Stapelfehlern im Silizium. Experimentelle Studien kamen zur Annahme, dass neuartigen Defekte den pn-Übergang im Silizium lokal kurzschließen und somit die Effizienz der Solarzelle drastisch verringern. In der hier vorliegenden Arbeit wird ein atomistisches Modell eines Natrium-dekorierten Stapelfehlers entwickelt und dessen elektrische und thermodynamische Eigenschaften untersucht. Dabei stellt sich heraus, dass die Einlagerung von Natrium zu einer starken Aufweitung des Stapelfehlers führt. Die dabei verlängerten Silizium-Bindungen führen zu elektrisch aktiven Defektzuständen in der Bandlücke des Siliziums, was ein Kurzschließen des pn-Übergangs ermöglicht. Darüber hinaus wird die thermodynamische Stabilität des Defekts – insbesondere im Hinblick auf die für die Potential-induzierte Degradation relevanten Materialsysteme (Antireflexionsschicht, Siliziumoxidschicht, etc.) – untersucht.

Abstract

In this thesis, metallic impurities in polycrystalline photovoltaic silicon are studied using first-principles methods. To this end iron and sodium have been chosen and investigated as distinct representative elements.

Nowadays, most silicon-based solar cells are produced from polycrystalline silicon which contains both large concentrations of impurity atoms and large densities of extended defects such as grain boundaries and dislocations. The detrimental influence of iron impurities on the efficiency of silicon-based solar cells is known for long time. In addition, iron atoms interact with extended defects. The electrical properties of those extended defects can be influenced by the segregated iron impurities. The goal of the first part of this work is to extend the knowledge of this interaction in three different scenarios. With the help of atomistic simulations, the influence of large-angle grain boundaries, mechanical stress and strain fields, and dislocations on iron impurities is studied. It turns out, that mechanical strain fields which are caused for instance by extended defects do not lead to an accumulation of iron atoms in specific regions but instead alter their diffusion properties significantly. In contrast, the segregation of iron impurities is possible in some large-angle grain boundaries and in the cores of all considered dislocations. In all cases the segregation of iron strongly influences the electronic properties of the extended defects.

The second part of the current work is dedicated to the recently discovered potential-induced degradation of solar cells and to sodium-decorated stacking faults which are suspected to play an important role in this context. From experimental studies it is assumed that such novel stacking faults lead to a local short-circuit of the pn-junction of the silicon and thus lower drastically the efficiency of the solar cell. In this work, an atomistic model of a sodium-decorated stacking fault is created and its electronic and thermodynamic properties are studied. The decoration of sodium leads to a large widening of the stacking fault. The elongated silicon bonds induce electrically active defect states in the band gap which can cause the short-circuiting of the pn-junctions. In addition, the thermodynamic stability of the sodium-decorated stacking fault is studied with special care of the material systems (anti-reflection coating, silicon oxide layer, etc.) that are relevant to the problem of potential-induced degradation.

Erklärung

Hiermit erkläre ich Folgendes:

1. Die vorliegende Arbeit wurde selbstständig und ohne die unzulässige Hilfe Dritter verfasst. Insbesondere habe ich hierfür nicht die entgeltliche Hilfe von Vermittlungs- beziehungsweise Beratungsdiensten (Promotionsberater/-beraterinnen oder anderer Personen) in Anspruch genommen.
2. Es wurden keine anderen als die angegebenen Quellen und Hilfsmittel benutzt. Wenn immer Teile der hier dargestellten Ergebnisse durch die Mitarbeit anderer Personen entstanden sind, wird dies entsprechend gekennzeichnet.
3. Die Arbeit wurde bisher weder im In- noch im Ausland in gleicher oder ähnlicher Form einer Prüfungsbehörde vorgelegt.
4. Die Bestimmungen der Promotionsordnung der Universität Freiburg für die Fakultät für Mathematik und Physik sind mir bekannt; insbesondere weiß ich, dass ich vor der Aushändigung der Doktorurkunde zur Führung des Doktorgrades nicht berechtigt bin.

Freiburg, 15.10.2015

. . . . . .

(**Benedikt Ziebarth**)

List of publications

Parts of this thesis are already or will be published in peer-reviewed journals:

- **B. Ziebarth**, M. Mrovec, C. Elsässer and P. Gumbsch, *Segregation of interstitial iron impurities at cores of dissociated dislocations in silicon from first-principles*, submitted for publication to Physical Review B.
- **B. Ziebarth**, M. Mrovec, C. Elsässer and P. Gumbsch, *Influence of dislocation strain fields on the diffusion of interstitial iron impurities in silicon* , Physical Review B **92**, 115309 (2015) [1].
- **B. Ziebarth**, M. Mrovec, C. Elsässer and P. Gumbsch, *Interstitial iron impurities at grain boundaries in silicon: A first-principles study*, Physical Review B **91**, 035309 (2015) [2].
- **B. Ziebarth**, M. Mrovec, C. Elsässer and P. Gumbsch, *Potential-induced degradation in solar cells: Electronic structure and diffusion mechanism of sodium in stacking faults of silicon*, Journal of Applied Physics **116**, 093510 (2014) [3].

Contributions to conferences:

- Frühjahrstagung der Deutschen Physikalischen Gesellschaft (2015) Berlin
  Talk: *Iron segregation at dislocations in silicon from first-principles*
- 7th International Conference on Multiscale Materials Modeling (2014) Berkeley
  Poster: *A study of iron impurities interacting with grain boundaries in photovoltaic silicon using density functional theory*
- Materials Science and Engineering (2014) Darmstadt
  Talk: *A study of iron impurities interacting with grain boundaries in photovoltaic silicon using density functional theory*
- Hermes Materials Modeling Summer School (2014) London
  Poster: *A study of iron impurities interacting with grain boundaries in photovoltaic silicon using density functional theory*
- Frühjahrstagung der Deutschen Physikalischen Gesellschaft (2014) Dresden
  Talk: *Conducting monolayers of sodium at stacking faults in silicon*

Awards:

- Best Poster Award for *A study of iron impurities interacting with grain boundaries in photovoltaic silicon using density functional theory* at the 7th International Conference on Multiscale Materials Modeling (2014) Berkeley

Journal publications unrelated to this thesis:

- A. Stoffers, **B. Ziebarth**, J. Barthel, O. Cojocaru-Mirédin, C. Elsässer and D. Raabe, *Complex structure of an asymmetric $\Sigma 9$ grain boundary in silicon*, submitted to Physical Review Letters.
- B. Lang **B. Ziebarth** and C. Elsässer, *Lithium ion conduction in $LiTi_2(PO_4)_3$ and related compounds based on the NASICON structure: a first-principles study*, Chemistry of Materials, **27** (14), 5040–5048 (2015) [4].
- **B. Ziebarth**, M. Klinsmann, T. Eckl and C. Elsässer, *Lithium diffusion in the spinel phase $Li_4Ti_5O_{12}$ and in the rocksalt phase $Li_7Ti_5O_{12}$ of lithium titanate from first principles*, Physical Review B **89**, 174301 (2014) [5].

Contents

1 Introduction

The energy transition from fossil fuel to renewable energy sources is one of the key challenges for mankind to stop climate change and environmental degradation. Photovoltaics plays a crucial role in this context, since it is predicted to outperform fossil fuel energy generation through cost leadership within the next 10 years [6]. Also Swanson's law that states a reduction of the price of solar cells by 20% for every doubling of industrial capacity hints to a further price reduction of photovoltaics [7, 8]. Industrial capacities are currently growing fast since the demand for photovoltaics installations remains high and is even expected to grow by 25% in 2015 [9]. Moreover, companies are making investments to build large facilities with production capacities of up to 500 MW per year [10]. The importance of power production by solar cells is already well recognized for example in Germany where a total capacity of 38.5 GW power production by solar cells has been installed over the last few years. This can already cover up to 50% of the total electric power consumption in Germany on a sunny day of the weekend [11].

Despite the large research interest and a variety in new materials which can be used for photovoltaic applications such as organic [12–15] or perovskite [16–18] compounds, the solar cell production is dominated by silicon wafer based solar cells with up to 90% of the total solar cell production [11]. With a market share of about 55% polycrystalline silicon is still the most used feedstock material for solar cells. Scaling effects and optimization of the silicon value chain by the solar cell producers drive down the total costs and make it difficult for other technologies to challenge the silicon technology for large market shares. Therefore, silicon will remain the most important material in solar cell production for the foreseeable future. Since one third of the costs of a solar cell is the cost of the feedstock [19], companies have started to explore the possibility of using cheaper materials such as metallurgical silicon [20]. However, these materials come with the disadvantage of containing larger amounts of metallic impurities, and these cause efficiency losses due to their action as recombination centers [21–25] or due to the formation of electrically conducting precipitates [26].

While in recent years a lot of work has been dedicated in the refinement of manufacturing techniques and fast analysis methods to control the impurity contamination during the production of solar cells, only little effort has been invested to understand the fundamental behaviour of metal impurities in the microstructure of polycrystalline Si. In this work two different types of metal impurities are considered. Based on macroscopic experimental studies, atomistic model systems are identified and investigated using state-of-the-art quantum-mechanical first-principles methods. The first part of this thesis focuses on iron impurities which have been known for long time to have a most detrimental effect on the efficiency of a solar cell [21, 22, 27]. The second part treats a rather novel phenomenon: the potential-induced degradation [28–30]. This degradation effect was recently discovered in large-scale solar cell plants and was related to sodium-decorated stacking faults but their detailed electrical behaviour is still unclear. In the following, the two parts of the work are concisely summarized.

Iron impurities in photovoltaic silicon In order to improve the solar cell efficiency, different processing techniques are applied for the passivation of iron contaminants in order to reduce their recombination activity. For instance, attractive interactions between extended defects in polycrystalline silicon, namely grain boundaries and dislocations and the diffusing iron atoms are exploited to reduce the recombination activity [31–35]. We consider three differently distorted environments of iron impurities in silicon: grain boundaries, mechanical strain fields and cores of dislocations.

- The first aspect concerns the most natural class of extended defects in a polycrystalline material: grain boundaries. Experimental studies observed iron segregation at some specific grain boundaries [24, 36–38] which indicates that the segregation behavior of iron depends on the misorientation of the two grains. However, recent investigations found that the characterization of the attraction of an iron atom by a grain boundary solely by the misorientation of the grains is not sufficient. The interaction also depends on the inclination of the grain boundary plane [36, 39, 40]. In this work, we therefore address the question how iron atoms segregate at grain boundaries in silicon in section 3.2. For this purpose the energetic stability of iron impurities at various interstitial sites is investigated at a set of symmetrical tilt and twist grain boundaries.

- Another important influence on the behaviour of metallic impurities in a poly-

crystalline material are mechanical strain fields. Mechanical strain can affect impurities in various ways. It may lead to an accumulation of the impurities or to a change of the diffusivity of impurities. Indeed many studies indicate that interstitial iron is affected by strain [41–46]. So far, most conclusions have been drawn from interpretations of macroscopic experiments but direct observations at the atomic scale have not been made yet. Theoretical first-principles calculations allow us to investigate the influence of mechanical strain on iron impurities. The formation energies of various defect configurations of iron in silicon are calculated at finite temperatures and subject to various states of strain. Moreover, the influence of strain on the diffusion of interstitial iron is studied by means of transition state theory combined with kinetic Monte-Carlo simulations. This part of the work is reported in section 3.3.

- The third part on iron impurities in silicon focuses on their interaction with the cores of dislocations. Like grain boundaries, dislocations are known to play an important role for the efficiency of silicon-based solar cells [34, 47–49] but they occur already in single-crystalline silicon which is used for other semi-conductor devices as well [50, 51]. The segregation of metallic impurities at dislocations is of particular interest because the local electronic structure of dislocations is changed by decoration with metal impurities [34, 47, 52, 53]. For iron, various studies indicate an attractive interaction between a dislocation core and an interstitial iron [54, 55] but no clear proof for this behavior exists yet. The complication for experiments to study one dimensional objects like isolated dislocations and the great interest in the electronic structure of dislocations make first-principles methods to a rather ideally suitable tool to study iron impurities at the cores of dislocations. We chose the most important types of dislocation cores, calculated segregation energies of interstitial iron impurities at these cores, and analyzed their electronic densities of states, cf. section 3.4.

Sodium-decorated stacking faults in photovoltaic silicon The second part of the thesis focuses on the atomistic defects which cause the potential-induced degradation of solar cells. While interstitial iron impurities just lower the efficiency of solar cells, other defects affect their reliability and lifetime. Potential-induced degradation is caused by the drift of ions, namely sodium, from the protective glass to

the silicon surface. This drift is caused by an electric potential gradient between the solar cell and the frame of the module [28]. It is build up due to the serial connection of the individual solar cells in a photovoltaic module and can amount to a voltage difference of up to 1000 V. Once the ions have migrated to the surface of the Si wafer they may diffuse into the silicon or stay at the interface between the silicon surface and the anti-reflection coating which is often made of silicon nitride [30]. Experimental observation found that sodium diffuses into stacking faults and covers them completely [56]. Such sodium-decorated stacking faults were identified as the primary reason for potential-induced degradation in silicon solar cells because they lead to local electrical short-circuits of the p-n junctions [28–30, 56, 57]. However, information on their structural, thermodynamic, or electronic properties is limited or even completely lacking. In the second part of the thesis, in section 4, we construct, calculate, and analyze a model system of a sodium-decorated stacking fault in order to answer these open questions rather consistently.

2 Methods

2.1 Density functional theory

The theoretical study of metal impurities in polycrystalline silicon at the atomic scale requires an accurate and predictive as well as sufficiently fast computation method. The latter is required since relatively big atomistic model systems for grain boundaries or dislocations have to be studied which can only be represented by relatively large numbers of atoms. The quantum-mechanical description of a system of many atoms is given theoretically by the Schrödinger equation, but practically for realistic systems such as crystalline solids with structural defects the Schödinger equation cannot be solved even by most powerful computational means. The density functional theory (DFT) has proven to provide a versatile computational framework to study quantum-mechanical properties of many-body problems and it has been successfully applied to virtually countless problems of material science, for instance the charging behavior of electrodes of Li ion batteries [5, 58], the diffusion of H in polycrystalline Ni [59], the prediction of novel crystal structures [60], etc. DFT provides an accurate description of relevant quantities such as total energies and atomic forces which can be used to derive quantities such as formation energies of defects or diffusion constant of impurity atoms. These are highly important quantities to describe the structural and electronic properties of metal impurities in polycrystalline Si. In the following we will compile the key features of DFT. An extensive review of this theory is not in the scope of this thesis. This can be found for instance in [61].

The starting point of our brief introduction to DFT is the Hamiltonian for a system of nuclei and electrons in the Born-Oppenheimer approximation in which the electronic

degrees of freedom have been decoupled from the ionic degrees of freedom,

$$\hat{H} = -\frac{1}{2}\sum_i \nabla_i^2 + \sum_i V_{\text{ext}}(\mathbf{r}_i) + \frac{1}{2}\sum_{i\neq j}\frac{1}{|\mathbf{r}_i - \mathbf{r}_j|} \tag{2.1.1}$$

where

$$V_{\text{ext}}(\mathbf{r}_i) = \frac{1}{2}\sum_{i,I}\frac{Z_I}{|\mathbf{r}_i - \mathbf{R}_I|} \tag{2.1.2}$$

is the external potential of a static distributions of nuclei I with a nuclear charge of Z_I. $\mathbf{r}_i$ and $\mathbf{R}_i$ denote the positions of electrons and nuclei, respectively. Note that we have adopted atomic Hartree units, i.e. $\hbar = m_e = e = 1/4\pi\epsilon_0 = 1$. In principle, the corresponding Schrödinger equation can be solved to obtain energies and other physical observables of the many-particle system of dynamic (light and fast) electrons in the field of static (heavy and slow) nuclei. In practice, the electron-electron interaction (given by the third sum of Eq. 2.1.1) makes this task impossible for realistic system.

Hohenberg and Kohn have recognized in their first theorem that *the ground-state electron density n of any interacting system under the influence of an external potential V_{ext} determines this external potential V_{ext} uniquely (up to a constant) [62].* From this theorem it follows that – in principle – all properties of the whole physical system are determined from the ground-state electron density because the Hamiltonian of the system is determined by the external potential. In their second theorem, Hohenberg and Kohn have proven *the existence of a universal functional of the density $E[n]$ whose global minimum is the ground-state energy of the system and the density which minimizes E is the ground-state density [62].* There are two key points in this theorem. First, the functional $E[n]$ is universal, i.e. it does not depend on a specific system and, hence, it has the same mathematical form for different chemical bindings such as metallic bonds or covalent bonds. Second, the ground-state energy and the ground-state electron density can be obtained by a minimization of the energy functional. Compared to solving the Schrödinger equation, this is a relatively simple task because the electron density ($n : \mathbb{R}^3 \to \mathbb{R}$) is a much simpler object than the multidimensional many-electron wavefunction ($\psi : \mathbb{R}^{3N} \to \mathbb{C}$) of a system with N electrons.
At this stage there is no practical applicability of the theory since the universal energy functional is not known. This shortcoming has been overcome by the approach of Kohn and Sham which is based on the assumption that the ground state-electron density of the

system of interacting electrons is also the ground state-electron density of an auxiliary system of independent quasiparticles [63]. The Schrödinger equation of this auxiliary system reads

$$\hat{H}_{\text{KS}}\,\psi_i = (-\frac{1}{2}\nabla^2 + V_{\text{KS}}(\mathbf{r}))\,\psi_i = \epsilon_i\,\psi_i \tag{2.1.3}$$

with an effective potential $V_{\text{KS}}(\mathbf{r})$. For such a Hamiltonian of a system of independent quasiparticles (conveniently called "electrons" again in the following), the many-body wavefunction is a Slater determinant that is constructed by the one-particles orbitals, $\psi_i(\mathbf{r})$, with the lowest energies. From these orbitals, it is straightforward to obtain the electron density by

$$n(\mathbf{r}) = \sum_{i=1}^{N_{\text{particles}}} |\psi_i(\mathbf{r})|^2. \tag{2.1.4}$$

For this system, the kinetic energy $T[n]$ of the electrons, the classical electrostatic Hartree energy $E_{\text{Hartree}}[n]$ and the external potential energy E_{ext} can be directly expressed in terms of one-particle orbitals, but the explicit form of the contribution for the so-called exchange-correlation energy E_{xc}, which takes Pauli's principle and all further many-electron interactions into account, remains unknown. The energy functional $E[n]$ becomes

$$E[n] = T[n] + E_{\text{Hartree}} + E_{\text{ext}} + E_{\text{xc}} + E_{\text{II}} \tag{2.1.5}$$

with

$$T[n] = \sum_{i=1}^{N} \int d\mathbf{r} |\nabla\psi_i(\mathbf{r})|^2 \tag{2.1.6}$$

$$E_{\text{Hartree}} = \frac{1}{2}\int d\mathbf{r}d\mathbf{r}' \frac{n(\mathbf{r})n(\mathbf{r}')}{|\mathbf{r}-\mathbf{r}'|} \tag{2.1.7}$$

$$E_{\text{ext}} = \int d\mathbf{r} V_{\text{ext}}(\mathbf{r})n(\mathbf{r}) \tag{2.1.8}$$

and the energy contribution from the interaction E_{II} of the nuclei. By variation of the total energy expression, one obtains the expression of the effective potential

$$V_{\text{KS}} = V_{\text{ext}}(\mathbf{r}) + V_{\text{Hartree}}(\mathbf{r}) + V_{\text{xc}} \tag{2.1.9}$$

and

$$V_{\text{Hartree}}(\mathbf{r}) = \int \frac{n(\mathbf{r}')}{|\mathbf{r} - \mathbf{r}'|} d\mathbf{r}' \tag{2.1.10}$$

$$V_{\text{xc}} = \frac{\delta E_{\text{xc}}[n]}{\delta n[\mathbf{r}]} \tag{2.1.11}$$

The four equations 2.1.3, 2.1.10, 2.1.11, and 2.1.4 are known as the Kohn-Sham equations. They need to be solved in a self-consistent way. The exchange-correlation energy has to be approximated and a lot of efforts has been made to construct improved approximations for its description [64–66]. Throughout this thesis, the generalized gradient approximation is used in the parameterization by Perdew, Burke, and Ernzerhof [65] which is widely used in material science. Forces on ions can be calculated from Eq. 2.1.5 using the Hellmann-Feynman theorem according to [67]

$$\mathbf{F}_{\text{I}} = -\frac{\partial E}{\partial \mathbf{R}_{\text{I}}} = -\int d\mathbf{r}\; n(\mathbf{r}) \frac{\partial V_{\text{ext}}(\mathbf{r})}{\partial \mathbf{R}_{\text{I}}} - \frac{\partial E_{\text{II}}}{\partial \mathbf{R}_{\text{I}}} \quad . \tag{2.1.12}$$

With the help of DFT it is now possible for us to calculate intrinsic properties of an atomic system such as the total energy or atomic forces. The computational details are given in the Appendix. In the following we will describe how these quantities can be used to describe the diffusion of impurities by means of transition state theory combined with kinetic Monte-Carlo simulations.

2.2 Diffusion

The movement of particles from regions of high concentrations to those of low concentrations at a continuum scale is described by Fick's first law as a linear response between a gradient of concentration ∇C and a flux of particles $\mathbf{J}$ [68, 69].

$$\mathbf{J} = -D\nabla C \tag{2.2.1}$$

where D is the diffusion coefficient. In the following subsections, we will explain how atomistic simulation can be used to obtain diffusion coefficients. Einstein and Smoluchowski first recognized the link between the diffusion coefficient and motion of the individual particles. They showed that the diffusion coefficient D is proportional to the mean square displacement of the individual particles at the atomic scale [70, 71]. This

relation allows us to obtain the diffusion coefficient of impurities in silicon once we are able to describe their individual movement.

In crystalline solids, diffusion of atomic defects occurs by their migration between sites of the crystal structure either via interstitial- or vacancy-mediated jump processes. Since a single jump of the defect happens much faster than the overall motion of the defects that causes the macroscopic diffusion, one can separate the problem into two different tasks: first, the calculation of the rate of an individual jump which is approached by transition state theory in our study, and second, the calculation of multiple jumps to obtain the diffusion constant which is done by kinetic Monte Carlo simulations in our case.

2.2.1 Transition state theory and the nudged elastic band method

In the following we will limit ourselves to the case of interstitial diffusion in which a defect atom is located at an interstitial site in the crystal structure. At finite temperature, these interstitial atoms vibrate around their equilibrium positions but their vibrations are usually not large enough to overcome the barrier to a neighbouring site. In rare occasions, the interstitial atom has sufficiently large thermal energy to overcome the barrier and to move to a new interstitial site. There it looses its energy to its surrounding and stays there until another rare jump event takes place. The important quantity to describe a series of such rare jump events is the rate at which these occur. Vineyard showed that in the harmonic approximation [72, 73], one can describe this rate Γ by

$$\Gamma = \nu \mathrm{e}^{-\Delta E/k_B T} \tag{2.2.2}$$

in which ν is the frequency factor, ΔE is the energy barrier along the path, k_B is the Boltzmann constant and T is the absolute temperature.

Before we can obtain the energy barrier from DFT calculations, we have to identify the minimum energy path (MEP) that connects two neighbouring stable sites with the lowest energy barrier. One computational technique to determine the MEP is the nudged elastic band (NEB) method [74, 75]. The general idea of the NEB method is to sample the MEP path with a finite number of *images*. The initial images are often obtained from a linear interpolation between the start and end sites of the MEP. The MEP is determined when the forces orthogonal to the tangent of the path are minimized. In addition, spring

forces between the images are introduced to keep the images equidistant. In some cases, the number of images is too small to resolve the precise saddle-point location of the transition state. One way to overcome this problem is to introduce more images along the path. But since NEB calculations which are based on DFT calculations are very costly, it is sometimes too expensive to increase the number of images. In such a case, an additional force parallel to the tangent of the path is given to the image with the largest energy such that it climbs up-hill in the energy landscape until it reaches its maximum along the MEP. This method is called the climbing image nudged elastic band (CI-NEB) method [74]. Once the MEP has been determined, it is straight forward to obtain the energy barrier ΔE as the energy difference between the start position and the transition-state position.

Following Vineyard [72], the frequency factor ν depends on the phonon modes of the system in the stable-site and transition-site configuration. For a given q-point of the phonon Brillouin zone (BZ), it can be obtained from products of phonon frequencies at the stable-site configuration ν^0 and the transition-site configuration $\nu^\dagger$ as following,

$$\nu_q = \frac{\prod_{i=0}^{3N_{\text{atoms}}} \nu_i^0(q)}{\prod_{j=0}^{3N_{\text{atoms}}-1} \nu_j^\dagger(q)}. \tag{2.2.3}$$

In a system of N_{atoms} atoms, for each q-point of the BZ, there are $3N_{\text{atoms}}$ phonon frequencies. In the transition-site configuration, the frequency associated with the unstable mode along the MEP is imaginary and is excluded from the product in Eq. 2.2.3. The overall frequency factor ν is obtained from an average of a sample set of ν_q's evaluated on a Monkhorst-Pack mesh of N_q q-points in the BZ [76]:

$$\nu = \frac{1}{N_q} \sum_{i=0}^{N_q} \nu_q \quad . \tag{2.2.4}$$

It has to be pointed out, that for the calculation of diffusion constants the energy barrier is much more important than the frequency factor since the former enters in the exponent, the latter only as a prefactor in Eq. 2.2.2.

2.2.2 Kinetic Monte Carlo

We now have a description for the rate of individual atomic jumps but our goal is to describe the diffusion coefficient. Diffusion coefficients can be calculated analytically for perfect crystals with only one relevant migration pathway for the diffusing species. However, alloying elements, the presence of structural defects, and the application of external stresses give rise to non-uniform deformations that make the migration pathways in a crystal nonequivalent and multiple. In these cases, more sophisticated approaches such as kinetic Monte Carlo (kMC) simulations [77–81] are needed to extract the diffusion behavior.

Within the kMC approach, the actual crystal system is mapped on a lattice and the trajectory of the diffusing particle is evolved by stochastic events with known jump rates. For the case of interstitial diffusion, the interstitial sites form the kMC lattice on which the migrating atoms can jump according to the jump rates obtained by TST. To evolve such a system for a given configuration, the sum of the rates of all accessible jump events, Γ_{total}, is calculated. Subsequently, a random number r, which is taken from a uniform distribution of real numbers between 0 and 1, is generated and the p-th jump event is chosen according to

$$\sum_{i=0}^{p-1} \Gamma_i < r\Gamma_{\text{total}} \leq \sum_{i=0}^{p} \Gamma_i \qquad . \tag{2.2.5}$$

Since the jump rates are constant and independent of the system's history, the process is a Poisson process [82] and, hence, the evolution for the n-th kMC step in real time is given by

$$t_n = t_{n-1} - \Gamma_{\text{total}} \ \ln r' \qquad , \tag{2.2.6}$$

where r' is another random number, which is again taken from a uniform distribution of real numbers between 0 and 1. From the final trajectory, one can obtain observables such as the diffusivity or the probability to find a particle at a given site. The observables are acquired from averages of an ensemble of trajectories to ensure their statistical significance.

Diffusion constants are obtained from mean square displacements, Δr_i^2, of all the diffus-

ing particles by

$$D = \sum_{i=0}^{N_{\text{particles}}} \frac{\Delta r_i^2}{2N t_{\text{total}}} \quad , \tag{2.2.7}$$

where $N_{\text{particles}}$ is the number of diffusing particles in the system and t_{total} is the total time of the trajectory.

3 Interaction of iron impurities with extended defects in silicon

3.1 Introduction

In the following we will briefly summarize what is known for iron impurities in polycrystalline silicon. The parts which will be covered are sketch in Fig. 3.1.

3.1.1 Iron impurities in silicon

Polycrystalline silicon is the most economical feed-stock material for Si-based solar cells. Due to the very challenging market situation for solar cell production, companies are forced to reduce the costs of their solar modules by using cheaper feed-stock materials like metallurgical silicon [20]. This saving usually comes with the disadvantage of larger amounts of metallic impurities in the material that cause electrical efficiency losses due to their action as recombination centers [21–25] or due to the formation of precipitates [26]. Among these metallic impurities iron (Fe) is known to have a strong detrimental effect on the efficiency of the solar cell [27]. This can be readily seen from Fig. 3.2 that shows the minority carrier diffusion length as a function of the concentration of different transition metals and FeB pairs in bulk-like regions. The shaded area represents the usual minority diffusion length found in common polycrystalline solar cells which can contain interstitial Fe up to a concentration of about $2\times10^{12}\text{cm}^3$ while much larger bulk concentrations of nickel and copper can be tolerated. The strong detrimental effect of Fe impurities makes it essential to be able to control its bulk concentration.

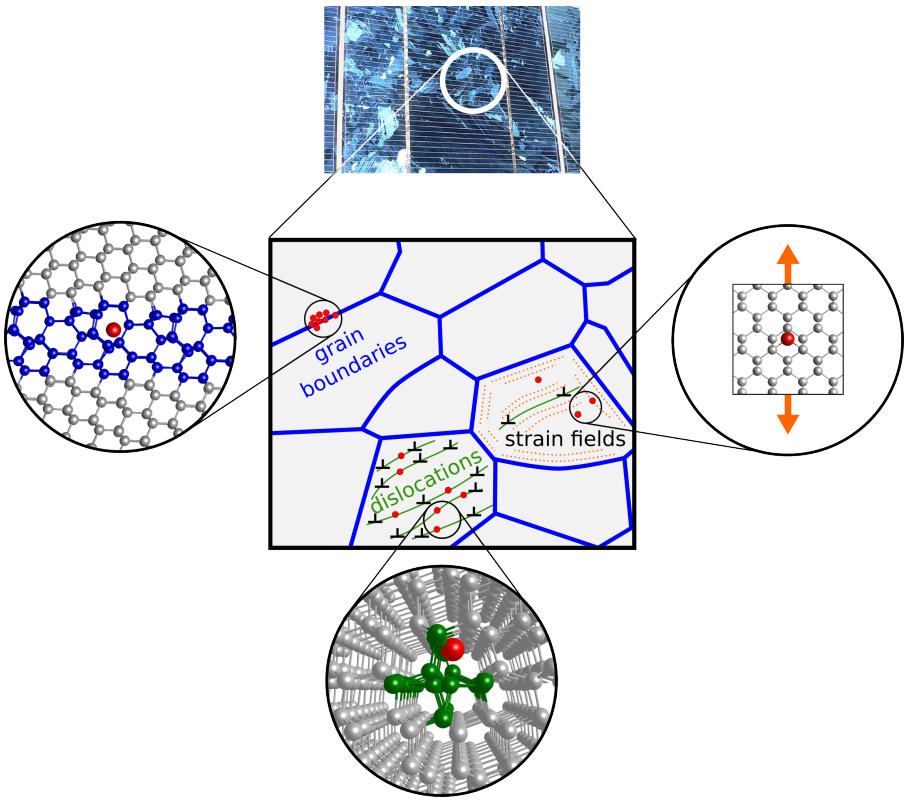

Figure 3.1: The microstructure of polycrystalline silicon includes various different kinds of extended defect structures such as grain boundaries, dislocations and strain fields. Iron impurities are considered in these three different environments in this chapter.

3.1.2 Iron impurities in crystalline bulk silicon

The behavior of impurity Fe atoms in Si bulk crystals has already been studied extensively by both theoretical and experimental means. The Fe impurities in bulk Si are occupying the tetrahedral interstitial sites of the diamond structure of crystalline Si. In p-type doped Si the Fe is positively charged (Fe^{+}) but usually paired with boron (FeB) or other shallow acceptors. In n-typed or non-doped Si the Fe remains uncharged (Fe^{0}) [21, 83]. Interstitial Fe creates a deep donor level at 0.4 eV above the valence band edge of bulk Si which causes the photo-induced charge carriers (electrons and holes) to recombine easily [21]. The electronic behavior of Fe in bulk Si was successfully explained by Ludwig and Woodbury who showed that the two 4s electrons of the bcc Fe atom are both transferred into the 3d orbitals when the Fe atom is embedded in the Si crystal [84]. This simple model is in very good agreement with electron-paramagnetic-resonance measurements and first-principles electronic-structure calculations [83, 85].

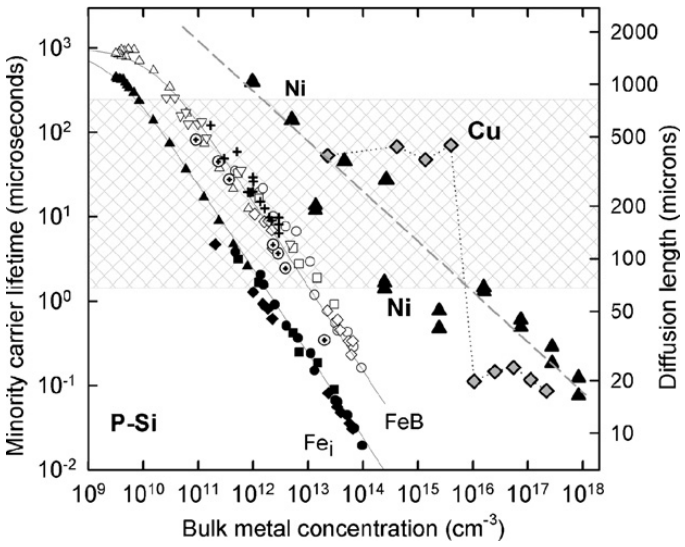

Figure 3.2: Impact of transition metals on minority charge carrier diffusion length in Si. Typical minority carrier diffusion lengths of polycrystalline Si solar cells are highlighted by the shaded area. Picture taken from Ref. [27].

3.1.3 Iron at extended defects in silicon

Importance of extended defects in silicon for iron impurities

Different processing techniques are applied for the passivation of Fe contaminants in order to improve the solar cell efficiency. The gettering of unwanted impurities is one possibilities in which they are removed by providing them an alternative location where they prefer to stay. This can be accomplished by various means. In contrast to extrinsic gettering techniques such as phosphorus gettering [86, 87] or aluminium gettering [86, 88], internal gettering exploits the attractive interaction between extended defects, namely grain boundaries (GBs) and dislocations, and the diffusing Fe atoms [31–35]. Only about 0.1–10% of Fe is interstitially dissolved in the Si matrix due to its limited solid solubility [21, 34] and most of the Fe is present in precipitates, e.g. iron silicides like β-$FeSi_2$ [89, 90]. It is known that iron silicides also act as recombination centers [26, 91]. Even though the Fe concentration in the Fe precipitates is high, the density of these precipitates is much lower than that of the interstitial Fe and thus the overall negative effect of Fe precipitates on the charge carrier life time is limited [34]. Hence, it is beneficial to condense as much interstitial Fe as possible into precipitates. However, in some rare cases an Fe precipitate can also short-circuit the pn-junction, which results in a failure of the solar cell [26]. Another important issue is connected with the electrical

activity of extended defects upon decoration by Fe. It has been noted that some defects such as large-angle GBs [92–94] and dislocations [52] are usually electrically inactive in pure Si, but in Fe contaminated Si the Fe atoms segregate to these GBs and dislocations and make these defects electrically active. Also the role of mechanical stress and strain fields which are induced by GB junctions and in particular by dislocations on interstitial Fe is still unclear and requires further studies [42, 91]. In the following we discuss the specific properties of grain boundaries, dislocations and strain fields in more detail.

Grain boundaries

One of the keys to improve the efficiency of polycrystalline Si solar cells is to understand the electronic activity of GBs. Several studies show that GBs can act as recombination centers for charge carriers [31–35] and also lead to large residual strains [44]. GBs can be classified into random GBs, large-angle GBs and small-angle GBs. In very pure Si, the first two classes of GBs apparently do not lead to any electrical activity [36]. This is most likely due to an effective reconstruction of Si-Si bonds at the GB interface. Unlike the strongly reconstructed GB interface of random and large-angle GBs, small-angle GBs are composed of an array of GB dislocations and therefore may act differently from large-angle GBs and random GBs. Indeed it has been shown that small-angle GBs are electrically active and emit luminescence even in very pure Si [95]. In the case of Fe contaminated Si, however, the large-angle GBs and the random GB exhibit a significant electrical activity [92–94]. In our study, we will focus on highly symmetric large-angle GBs since their electrical activity is mostly determined by their Fe contamination, and their interface structures are better defined than those of random GBs.

The segregation of Fe atoms and the precipitation of Fe silicide particles at large-angle GBs (in the following denoted simply as GBs) have been examined by various experimental studies using methods like photoluminisence (PL) spectroscopy [37, 38, 97] and electron beam induced current (EBIC) measurements [39, 95] in combination with transmission electron microscopy (TEM) [36, 98, 99], scanning electron microscopy (SEM) [36, 39, 94] and electron back scatter diffraction (EBSD) [36, 39, 94]. All these studies indicate that the segregation of Fe at GBs in Si strongly depends both on the misorientation of grains, often denoted by the Σ-value of the coincidence-site-lattice [100]. This can be readily seen in Fig. 3.3, where the metal contamination of the GBs as a function of its Σ value is shown. Despite the clear trend of the average metal content with respect to the Σ-value, the individual data points, however, are strongly scattered. This indicates

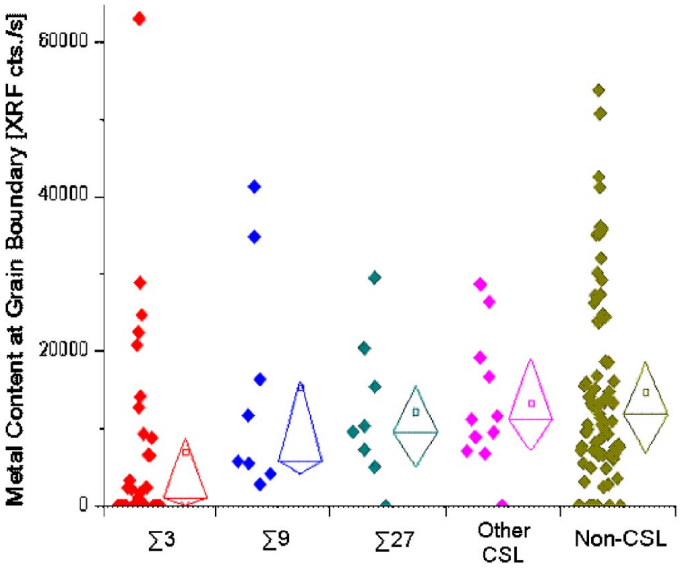

Figure 3.3: Dependence of metal content at grain boundaries (measured by x-ray fluorescence microscopy (XRF)) for different grain boundary characters as obtained from electron backscatter diffraction (EBSD). The open diamonds represent the 25th and 75th percentiles and the median. The mean is represented by the open boxes. Picture taken from Ref. [96].

that a characterization of the gettering efficiency of the GB by its Σ-value only is not sufficient. Another important feature of a GB is its interface inclination which is usually characterized by the interface plane which is labeled by Miller indices (hkl). Its importance can be seen for example in Fig. 3.4. There, it was observed that the Σ 3 (111) GB is not gettering Fe whereas Σ 3 (112) and Σ 3 (110) GBs contain large amounts of segregated Fe [36, 39, 40] once the Si wafer is contaminated with Fe. In order to elucidate this behavior, a systematic investigation of the atomistic mechanisms of Fe segregation at such GBs is required.

Dislocations

Among the predominant extended defects in photovoltaic silicon are dislocations. In particular in scaled-down semiconducting devices at dimensions of less than a few tens of nanometers, dislocations may be generated by high local strains due to lattices misfits between functional thin-film materials like Ge, SiGe or III-V compounds and the Si substrate [50, 51]. On the other hand, the utilization of individual dislocations as active components of semiconductor devices are discussed since they resemble native nanowire-like structures embedded in a Si matrix [101, 102]. Another important aspect

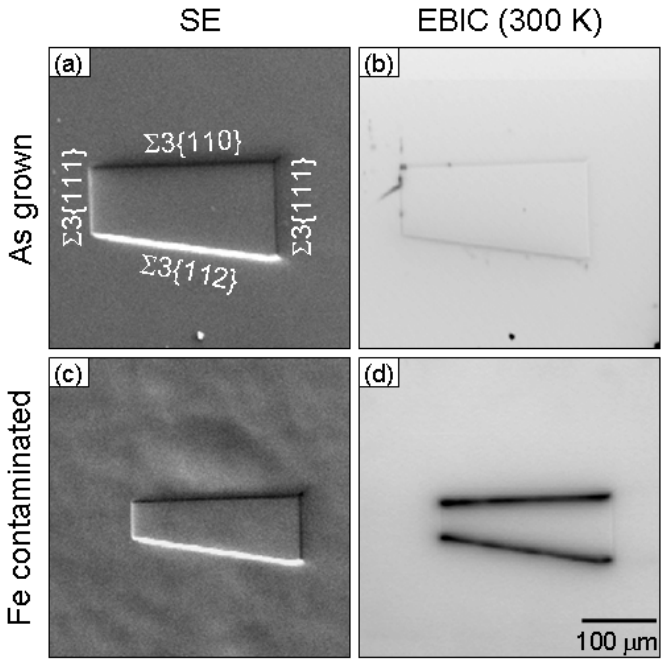

Figure 3.4: Scanning electron microscopy (SEM) and electron beam induced current (EBIC) images of different Σ 3 grain boundaries in clean (as grown) and contaminated (Fe contaminated) Si. Regions with high recombination activity show a black contrast in the EBIC picture. Picture taken from Ref. [36].

are dislocations in the context of Si-based polycrystalline solar cells as they represent one of the principal performance-limiting defects. They are also known to form different kinds of dislocation clusters with dislocation densities up to 10^6-10^7cm^{-2} [52]. Some kinds of such clusters act as seeds for the precipitation of silicides [48, 49]. In Fig. 3.5, photoluminisence images have been correlated with interstitial Fe concentration and dislocation density. The recombination activity measured by photoluminisence spectroscopy is strongly increased at regions of high interstitial Fe concentration. While in most of the regions an increased interstitial Fe concentration is correlated with a large dislocation density, there exists also regions which have large dislocation densities but low Fe concentrations. For instance, the dislocation densities in region A and B are both high, but only region A shows a reduction of the charge carrier lifetime correlated with a higher concentration of interstitial Fe. This hints to the hypothesis that charge carrier recombination is governed by the decoration of the dislocations by Fe impurities [34]. In some cases, dislocations show a strong recombination activity even without the contamination by metal impurities. However, it was shown that this activity is related to the existence of intrinsic defects (e.g. dangling bonds) which can be healed by adjusting

processing parameters for the Si material [52]. Moreover, it has been shown that metallic impurities in combination with Al or P gettering can be exploited to reduce the dislocation density significantly at moderate temperatures [103, 104]. It is therefore essential to extend the knowledge of the interaction between metallic impurities and individual dislocations.

Compared to grain boundaries, dislocations can interact with impurities on two different length scales: the short-range interaction is dominated by the dislocation core which is characterized by an atomic structure that is quite different from that in the bulk material, and the long-range interaction which is governed by a long-ranged stress field which results in a finite strain of the bulk-like region in the surrounding of the dislocation core [105]. In particular, transition metals are considered to segregate in the stress field of dislocations [106], to decorate the dislocation cores [47, 52, 107] and, hence, to alter the deep level spectrum of dislocations [52, 106]. It has also been observed that dislocations act as nucleation sites for metal precipitates such as Fe or Ni silicides [106].

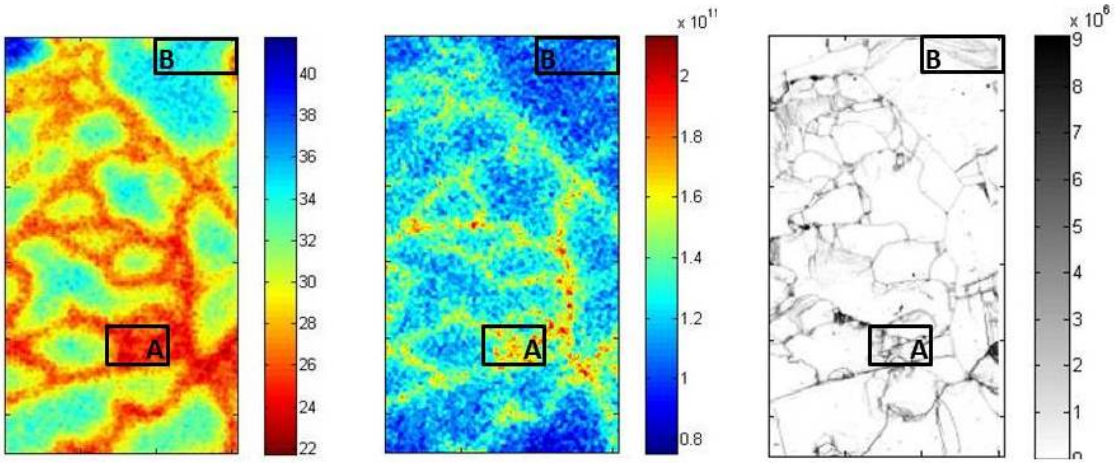

Figure 3.5: Photoluminescence image of the charge carrier lifetime [µs] (left), interstitial Fe concentration [cm^{-3}] (middle) and dislocation density map [cm^{-3}] (right). Dislocation densities have been obtained from etch pit counting. Picture taken from Ref. [34].

While most computational studies of dislocations in Si focus on the atomic arrangement [108–110] and thermodynamics of the dislocation cores [108, 111] as well as their kinetics [108, 112, 113], there also exists a limited number of studies on segregation of impurities at dislocations, e.g. the segregation of hydrogen [114, 115], arsenic [116, 117] and copper [107]. The first two elements are not transition metals and thus cannot be expected to behave similar to Fe. While Cu is a transition metal, the study of Fujita

et al. is limited to substitional Cu only. To the knowledge of the author, no atomistic study on the interaction between interstitial transition metals and dislocation cores exists in spite of its apparent importance.

Strain fields

Most extended defects such as dislocations [43], grain boundaries [44] and other extended defects [41] induce a stress field to their surrounding. In particular dislocations show a very long-ranged stress field which slowly decays as $\propto 1/r$ [105]. The influence of the stress field onto the segregation of metallic impurities is under frequent discussion and is still an open issue. While some studies do not find any correlation between Fe segregation and stress [36], others observe a strong agglomeration of Fe impurities to regions of high stresses [42]. The influence of stress on the diffusion properties of Fe has been investigated recently by Suzuki *et al.* [45, 46] using Mössbauer spectroscopy. In their first study [45], they reported that the energy barrier for interstitial Fe^0 diffusion was decreased from 0.68 eV to 0.33 eV at an applied stress of about 19 MPa stress. Such large change of the energy barrier of interstitial Fe^0 diffusion will result in diffusion constants which are different by several orders of magnitude even at room temperature. This would allow Fe^0 to diffuse throughout a solar cell within a few hours and therefore might alter the way Fe silicide precipitation takes place.

To understand the behaviour of Fe in Si adequately, a systematic study of the influence of strain on the thermodynamics and kinetics of interstitial Fe impurities in Si is necessary and may allow a better interpretation of experimental observations.

3.2 Interstitial iron impurities at grain boundaries in silicon

Our first part of the investigation of interstitial Fe impurities in Si is dedicated to the influence of grain boundaries (GBs). With about 55% market share, polycrystalline Si is the most used feedstock material for commercial solar cells [11]. In such materials, GBs are very abundant and it is confirmed that they are important for the efficiency of solar cells [31–35].

Each GB can be described by its macroscopic degrees of freedom: the orientation of the two grains and the inclination of the GB plane. But many more degrees of freedom exist at the atomic scale. Si atoms prefer to be four-fold coordinated which leads to the rearrangement of atoms at the GB interface and to the reconstruction of Si-Si bonds. This results in a variety of different realizations of reconstruction patterns with various possible interstitial sites which are different from the interstitial sites in the perfect bulk crystal. The different geometries of these interstitial sites may lead to preferred occupations by impurities like interstitial Fe. Such a process is called segregation. Moreover, segregated Fe atoms may change the local electronic structure of the grain boundary and thus affects the recombination activity of the GB which alters the efficiency of the solar cell.

The modeling of GBs by DFT simulations is challenging since we have to restrict ourselves to system sizes of a few hundred atoms. Moreover, most DFT codes require supercells with periodic boundary conditions. To obey these conditions, always two GBs have to be included into the supercell. These limitations require us to restrict ourselves to rather simple and symmetric GBs. Also the reconstruction pattern of the GB plane is difficult to determine and to find the most stable reconstruction pattern is by itself a challenging task. In this study, we rely on reported GB structures found in literature which have been determined using either experimental high resolution transmission electron microscopy or computational atomistic simulation. Although the choice of GBs with high symmetry seems to be too narrow, GBs with low symmetry often reconstruct into segments which can also be found in the highly symmetric GBs. We therefore expect that our results can also be extrapolated to other GBs.

In the following we report our results on the electronic structure and the segregation behavior of interstitial Fe atoms at GBs in Si. We have chosen a set of symmetrical tilt or twist GBs in Si which provides a variety of interface orientations and structures at the atomic scale. The content of this section has been published in [2] (Ziebarth et al., Phys. Rev. B **91**, 035309).

3.2.1 Models of grain boundaries in silicon
([1], Sec. III)

Models for a set of coincidence-site-lattice GBs of types Σ 3, Σ 5 and Σ 9 were created. These GBs differ by the inclination of their GB plane, and their local atomic configura-

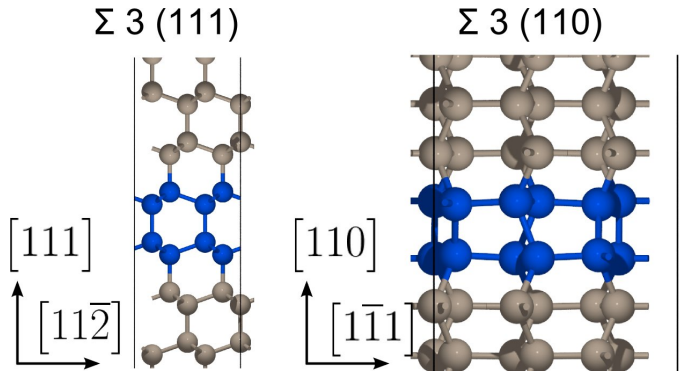

Figure 3.6: Supercell models of a symmetric tilt GB Σ 3 (111) and a symmetric twist GB Σ 3 (110). Due to periodic boundary conditions, there are two equivalent GBs in the supercells but for clarity only half of the supercells is shown with blue atoms highlighting the GB. Tripods indicate crystallographic directions of the cubic diamond structure.

tions. The GBs models were selected from low-energy structures of various computational studies and according to experimental observations. Details for the specific GBs are given in the following and in the discussion.

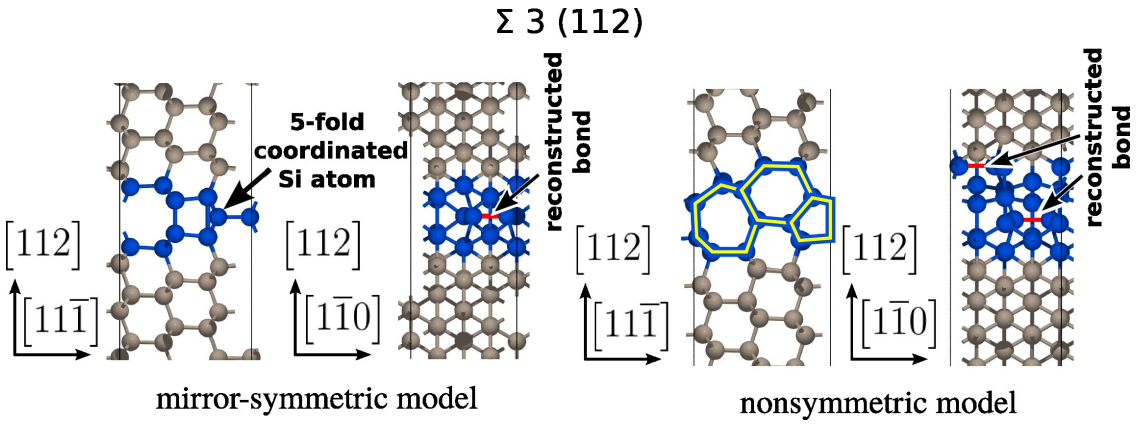

Figure 3.7: Supercell models of two variants of symmetric tilt Σ 3 (112) GBs.

Fig. 3.6 shows two Σ 3 GBs which differ in their interface planes. The supercells contain 96 and 72 Si atoms for the Σ 3 (111) and the Σ 3 (110), respectively. The Σ 3 (111) GB is a symmetric tilt GB with its [112] tilt axis lying in the GB plane. The Σ 3 (110) GB is a symmetric twist GB because the twist [112] axis is perpendicular to the GB plane. All Si atoms in these two GB models are 4-fold coordinated. The Σ 3 (111) GB has been observed in many experiments, see e.g. Ref. [36].

Fig. 3.7 shows the supercell models of another type of the Σ 3 GB, namely Σ 3 (112).

HRTEM investigations[99] showed that this GB can exist in at least two variants termed as mirror-symmetric and nonsymmetric model

The two structures differ in reconstructions of the Si bonds along the [112] direction as indicated by the red bond in Fig. 3.7. 5-fold coordinated Si atoms exist in the mirror-symmetric model whereas all Si atoms are 4-fold coordinated in the nonsymmetric model. The supercells contain 136 and 144 Si atoms for the nonsymmetric and mirror-symmetric model, respectively. The reconstructed GB consists of a series of 5-, 7- and 6-fold Si-rings which are indicated by yellow polygons in Fig. 3.7.

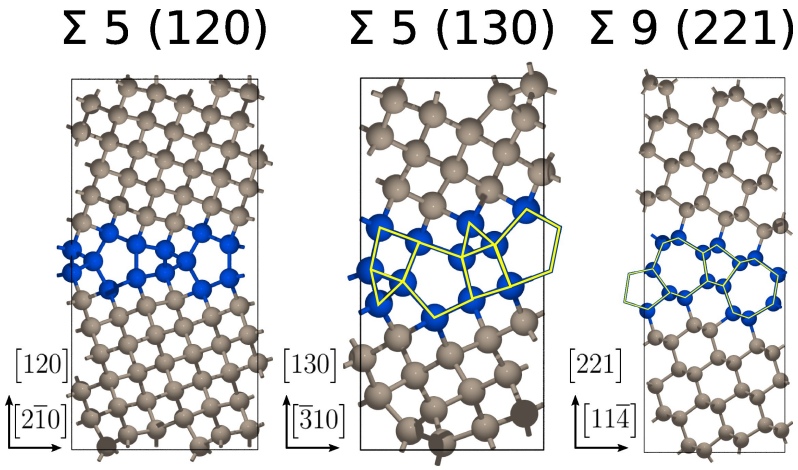

Figure 3.8: Supercell models of three symmetric tilt GBs: Σ 5 (120), Σ 5 (130) and Σ 9 (221).

Finally, Fig. 3.8 shows the supercell models of three GBs with higher Σ values: Σ 5 (120), Σ 5 (130) and Σ 9 (221). All Si atoms are 4-fold coordinated in these GB models. While the Σ 5 (120) and Σ 9 (221) GB interfaces are following a nonsymmetric pattern, the interface of the Σ 5 (130) GB is planar. While the interface structures of the Σ 5 GBs are build from 3-, 4- and 5-fold Si rings, the interface structure of the Σ 9 (221) consists only of 5- and 7-fold Si rings. The supercells contain 80, 40 and 136 Si atoms for the Σ 5 (120), Σ 5 (130) and Σ 9 (221) models, respectively. The structures of the chosen Σ 5 GBs have been reported in the literature to be low in energy [118–123]. To our knowledge, no theoretical first-principles study of the Σ 9 (221) GB has been reported so far, but our results for its interface structure is in agreement with experimental HRTEM observations [98].

Grain boundary	GB energy [J/m^2]	GB energy [meV/Å^2]
Σ 3 (111)	0.01	0.6
Σ 3 (112) sym.	0.67	41.8
Σ 3 (112) nonsym.	0.47	29.3
Σ 3 (110)	0.76	47.4
Σ 5 (120)	0.39	24.3
Σ 5 (130)	0.35	21.8
Σ 9 (221)	0.16	10.0

Table 3.1: Calculated GB energies.

3.2.2 Interface energies of grain boundaries
([2], Sec. IV. A)

Interface energies, γ_{GB}, for all GBs are defined as

$$\gamma_{\text{GB}} = \frac{E_{\text{GB}} - N_{\text{Si}} \cdot \mu_{\text{Si}}}{2A_{\text{GB}}}$$

where E_{GB} is the total energy of the GB supercell, N_{Si} is the number of Si atoms, μ_{Si} is the chemical potential of Si, i.e. the total energy of a Si atom in the equilibrium diamond structure and A_{GB} is the interface area of the GB. The factor of two in the denominator takes into account that there are always two grain boundaries in the supercells due to periodic boundary conditions.

The results for GB energies are listed in Table 3.1. As expected the Σ 3 (111) GB has a very low energy of 0.01 J/m^2. The results also indicate that the nonsymmetric reconstruction of the Σ 3 (112) GB leads to a reduction of the GB energy from 0.67 to 0.47 J/m^2.

Both Σ 5 GBs are similar in energy in spite of their clearly different geometric arrangements. The Σ 3 (110) GB has the highest energy of 0.76 J/m^2. The second lowest energy of all investigated structures, about 0.16 J/m^2, is found for the Σ 9 (221) GB.

3.2.3 Segregation of interstitial iron
([2], Sec. IV. B)

After optimization of the GB supercells for pure Si, a single Fe impurity has been inserted into various interstitial sites both in the vicinity of the GBs and in the bulk-like regions

of the models. Always one of the two Si GBs in the supercell was populated with Fe. In order to keep the number of calculations feasible we considered only charge-neutral $Fe^{(0)}$ interstitials. Segregation energies of the interstitial Fe atoms at GBs were calculated according to

$$E_{\mathrm{Fe}}^{\mathrm{seg}} = E^{\mathrm{tot}} - \gamma_{\mathrm{GB}} \cdot 2A_{\mathrm{GB}} - N_{\mathrm{Fe}}\mu_{\mathrm{Fe}_i} \tag{3.2.1}$$

where E^{tot} is the total energy of a Si GB supercell with an Fe impurity, N_{Fe} is the number of Fe atoms in the supercell, and μ_{Fe_i} is the chemical potential, which is set to the total energy of interstitial Fe in bulk Si, calculated with a cubic supercell containing 64 Si atoms and a single interstitial Fe atom. In addition, we validated that our results are well consistent by comparing the segregation energy of Fe in the bulk-like regions of the GB supercell models with that of Fe in the 64 atom bulk-Si supercell.

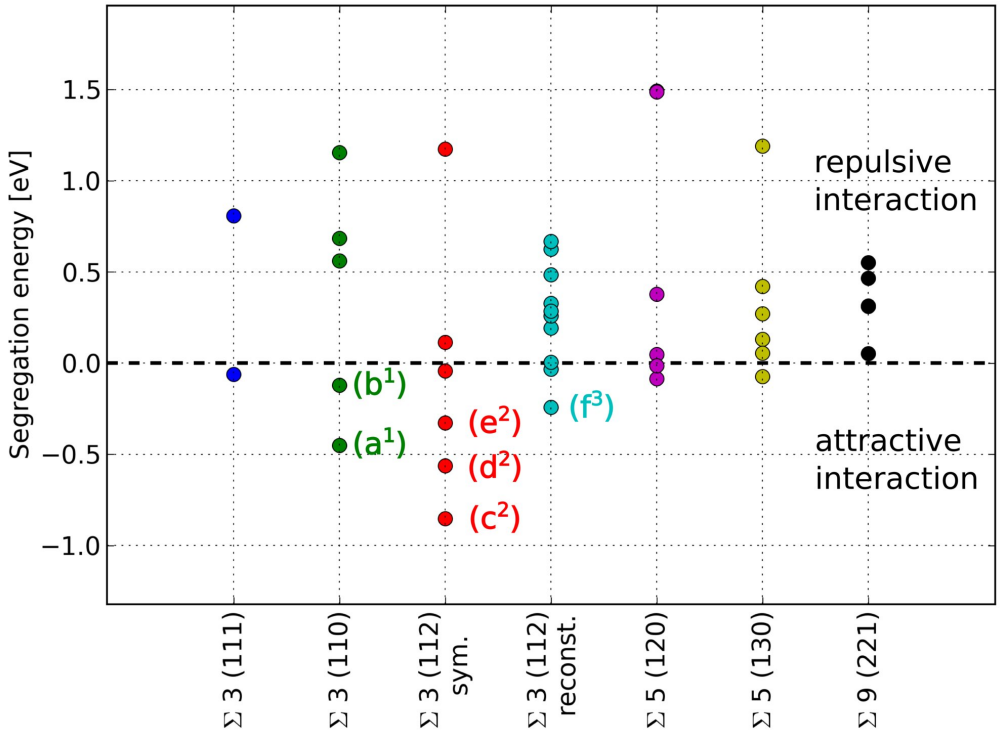

Figure 3.9: Segregation energies for various interstitial Fe within a 4-8 Å broad region around the GB. For the labeled structures more details are shown in Fig. 3.11.

We investigated more than 50 interstitial sites in the considered GBs. The segregation

energies of unique configurations are shown in Fig. 3.9. Negative segregation-energy values correspond to an attraction between the GB and Fe, positive values indicate that segregation is not favorable. Sites for which Fe segregation is favorable are labeled by (a^1) to (f^3) where the superscript marks the type of the GB: 1 for Σ 3 (110), 2 for mirror-symmetric Σ 3 (112) and 3 for nonsymmetric Σ 3 (112). These sites will be studied in detail in the following. All sites with segregation energies larger than -0.1 eV are not considered to attract Fe atoms significantly.

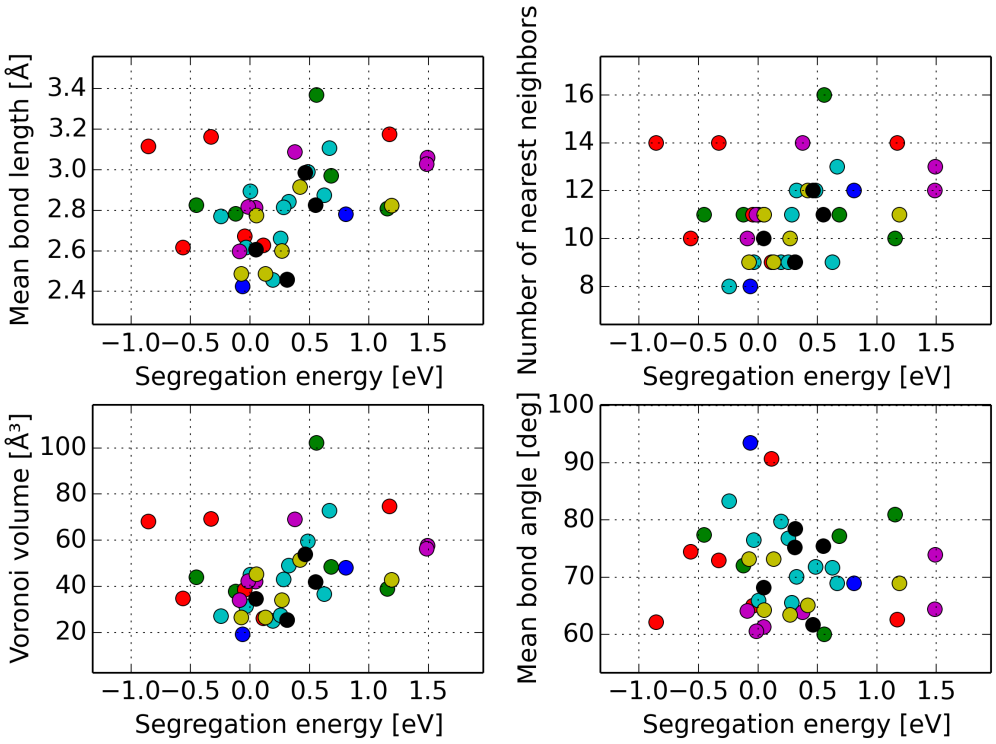

Figure 3.10: Geometric features of interstitial sites with respect to their segregation energy for all considered grain boundary sites. Nearest neighbors are neighboring atoms within a radius of 4 Å.

We attempted to correlate several geometric features of the segregation sites (e.g. coordination number, mean bond length, bond angle distribution and more) with the segregation energy. The results are shown in Fig. 3.10 which makes it clear that there is no simple correlation between the individual geometric features of the interstitial sites and the segregation energies of Fe to these sites.

From Fig. 3.9, it is evident that only three of the investigated GBs show a significant attractive behavior for interstitial Fe, namely the two Σ 3 (112) GBs and the Σ 3 (110) GB.

In Fig. 3.11, the local atomic arrangement of interstitial sites are displayed. The local structures of the (a^1) and (b^1) sites in the Σ 3 (110) GB are very similar. They differ only in two Si atoms which are nearby in (a^1) but are separated in (b^1). In the case of the symmetric model of the Σ 3 (112) GB the (c^2) and (e^2) sites differ only by their location in the reconstructed GB structure: while one site is located at the reconstructed Si-Si bond, the other site is in the more open environment. The site (d^2) resembles closely the tetrahedral position in bulk Si but with one additional Si neighbor giving it a 5-fold coordination. The site (f^3) of the reconstructed Σ 3 (112) GB is formed by a slightly disturbed 6-fold Si ring.

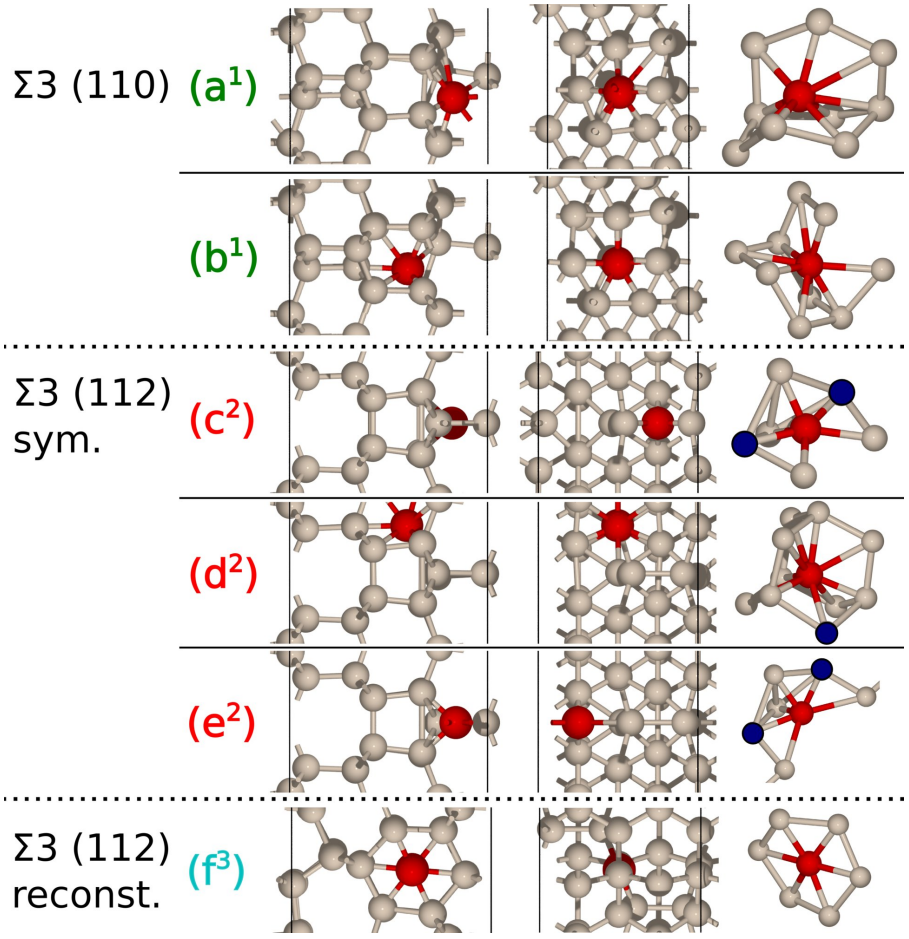

Figure 3.11: Low energy configurations of segregated Fe at GBs, cf. Fig. 3.9. The left column of pictures show the site along the $[1\bar{1}0]$ direction, while the pictures in 2nd column is along the $[111]$ direction. The left column shows the interstitial Fe with its surrounding only. Red spheres are Fe atoms and blue spheres indicate Si atoms with five Si neighbors.

Fig. 3.12 shows the site-projected densities of electronic states (PDOS) for all intersti-

tial configurations depicted in Fig. 3.11. The PDOS of interstitial Fe in bulk Si has been added as a reference. In bulk Si, interstitial Fe atoms occupy the tetrahedral sites formed by the nearest-neighbor shell of Si atoms. The second-nearest-neighbor shell of Si atoms provide an octahedral coordination. In this bulk interstitial configuration, the Fe-4s states are shifted to higher energies above the Fermi energy and, hence, the two 4s electrons are transferred into the lower lying Fe-3d states which are thus filled with eight instead of six 4d electrons, cf. uppermost left panel in Fig. 3.12. It turns out that the high-spin configuration is favored in bulk Si, i.e. the spin-up d states are completely filled by 5 electrons and the spin-down d states are occupied by 3 electrons. Due to the cubic crystal field symmetry, the 3d impurity level splits into t_{2g} and e_g levels. However, the crystal field contribution from the first nearest neighbors (tetrahedral coordination), which would result in more stable e_g bands, is apparently less effective than the crystal field contribution from the second nearest neighbors (octahedral coordination). In accordance with previous investigations, we find that the t_{2g} levels lie lower in energy than the e_g levels [84].

The spin-polarized state of the interstitial Fe in bulk Si remains stable for all GB structures shown in Fig. 3.9 except for (c^2) and (e^2). These two special cases will be analyzed further in the following.

At the GBs, the bulk-specific coordination pattern of nearest neighbor tetrahedral coordination and second nearest neighbor octahedral coordination is usually no longer present and, hence, the electronic structure of the Fe impurity and its environment changes. The investigated structures can be classified into two different groups.

The first group, (a^1), (b^1), (d^2) and (f^3), still favors the high-spin configuration like the interstitial Fe in bulk Si. However, the crystal-field-splitting of the d-levels is distorted: the d-levels split sometimes in more than two peaks and the peaks are no longer build up by either e_g or t_{2g} levels but by a mixture of the two. Interestingly, the resulting electronic structure of the d-levels (gray shaded area in Fig. 3.12) is still similar to that of the interstitial Fe at bulk.

The second group of structures, (d^2) and (f^3), favors the non-spin-polarized configuration. The peaks of the Fe d-levels overlap with peaks (turquoise) of a Si atom which is located in the nearest neighbor shell of Fe. This specific Si atom is coordinated by five Si atoms and marked by blue spheres in Fig. 3.11. The overlapping electronic states of neighboring atoms indicate the formation of a chemical bond. It is very likely that this effect causes the spin configuration of Fe to change.

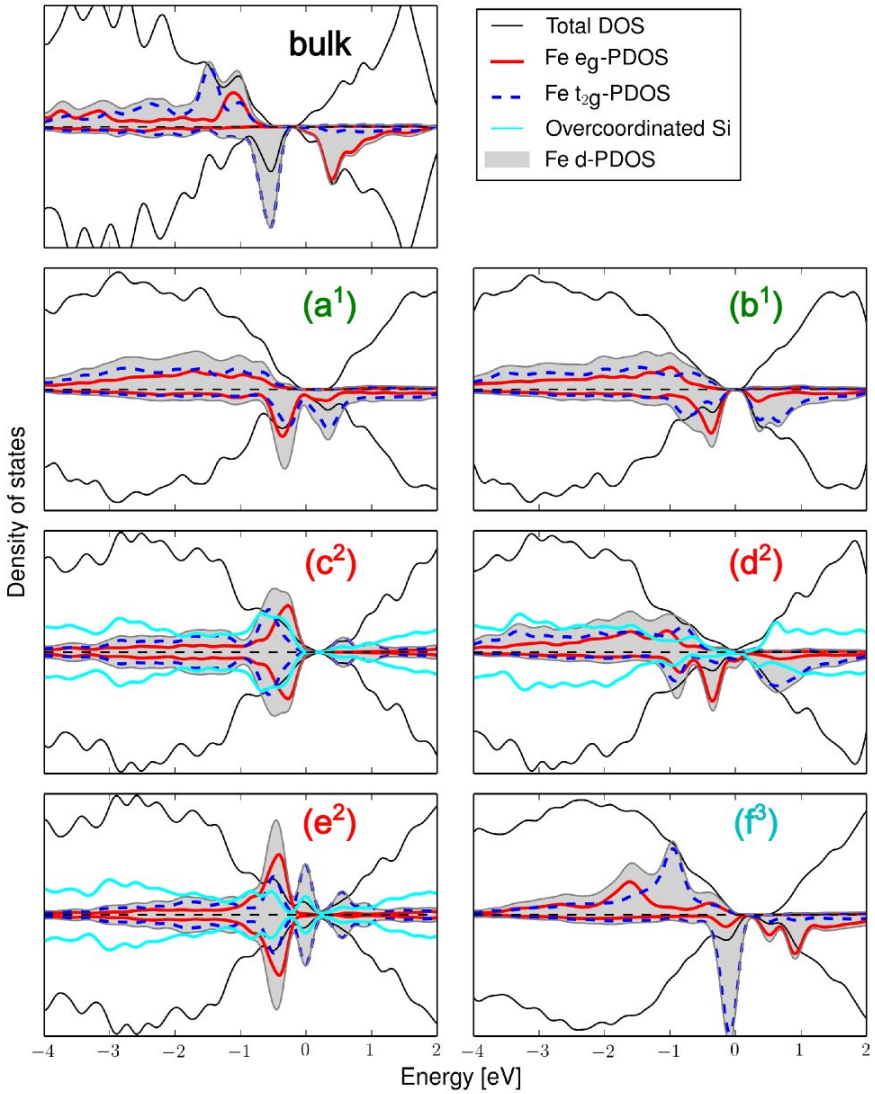

Figure 3.12: Total and local (site- and orbital-projected) densities of states for the various important segregation sites of interstitial Fe impurities at Si GBs depicted in Fig. 3.9 and 3.11. The energy is given with respect to the Fermi energy.

From the analysis above, we conclude that the change of the local electronic structure – in particular of the d-states – of interstitial Fe atoms at GBs in Si is mainly due to the different local environment. If only 4-fold coordinated Si atoms exist in this environment, the largest effect is due to the presence of the crystal field. 5-fold coordinated Si can perfectly lead to the formation of Fe-Si bonds that can alter the spin configuration of the interstitial Fe atoms.

3.2.4 Discussion
([2], Sec. V)

In order to study the behavior of Fe impurities in polycrystalline Si, atomistic models for seven symmetric GBs in Si were constructed and structurally relaxed, and their interface energies were calculated. The obtained structures for the two Σ 3 (112) GB models are in agreement with reported HRTEM observation by Watanabe *et al.* [99]. Experimentally, the mirror-symmetric arrangement of the GB was apparently found mainly in the vicinity of triple lines of GBs whereas the nonsymmetric arrangement was observed in GB segments which were free from any other structural distortion. Watanabe *et al.* also reported GB energies for the two Σ 3 (112) GB models from their first-principles calculations, namely 0.56 J/m^2 for the nonsymmetric and 0.75 J/m^2 for the mirror-symmetric model which are in good agreement to our values of about 0.47 J/m^2 and 0.67 J/m^2, respectively.

The results of recent first-principles studies for the Σ 5 (130) GB [120, 122] also agree well with our data. Our GB energy of 0.35 J/m^2 for the Σ 3 (112) GB is close to the values reported by Huang *et al.* (0.38 J/m^2) [120], Shi *et al.* (0.37 J/m^2) [119] and Lazebnykh and Mysovsky (0.29 J/m^2)[122]. We are not aware of any reports on atomistic studies for the Σ 5 (120) and Σ 3 (110) GBs. Our proposed models of the latter two GBs have similar GB energies as the other investigated GBs and hence we believe that such a GB configuration can exist in Si. We are confident that the chosen set of seven GB models is realistic, representative and useful to study the GB segregation of Fe impurities.

The Fe atoms were introduced at interstitial sites of the GBs. Among the seven GB models, for only three an attraction of Fe atoms is found, namely for both models of the Σ 3 (112) and the Σ 3 (110). This is in agreement with experimental SEM, HRTEM and EBIC observations. Chen *et al.* showed that in terms of Fe gettering the Σ 3 (111) GB behaves differently from the Σ 3 (112) and Σ 3 (110) GBs [36]. While latter two GBs strongly attract Fe, the Σ 3 (111) GB does not show Fe segregation at all. The different behaviors of a symmetric Σ 3 (111) and Σ 3 (110) GB was recently confirmed by Nacke *et al.* [44]. Chen *et al.* also reported that individual Fe atoms could be seen at the Σ 3 (112) GB in HRTEM [36]. This is also reflected by our results since only some but not all of the interstitial sites are apparently attractive. At variance to our present results, Chen *et al.* reported that the Σ 9 GBs also tend to attract Fe atoms. However, the interface plane orientation was not given for this Σ 9 GB. We therefore cannot be certain whether

the Σ 9 GBs which were investigated by Chen *et al.* have the (221) interface plane or a different one.

Two first-principles studies of Fe segregation at individual Si GBs have been reported in the literature: the Σ 3 (111) GB was studied by Suvitha *et al.* [124], and the Σ 5 (130) GB was investigated by Shi *et al.*[119]. The results of both studies for the segregation energies are in agreement within 0.1 eV with our results. Shi *et al.* also tried to correlate the local geometric arrangement of the Si atoms at the segregation sites with the segregation energy of Fe. Similarly to us, they concluded that it was not possible to identify any clear trend.

Our results indicate that in particular the symmetric Σ 3 (112) GB is a very favorable interface for Fe segregation. This may partially be attributed to an existence of 5-fold coordinated Si atoms at the GB. The segregated Fe atoms create a chemical bond with such Si atoms and thereby lower the energy. Such local bonding was indicated in the PDOS curves (cf. Fig. 3.12). Therefore, it is likely that intrinsic defects at GBs, such as Si atoms, that are not 4-fold coordinated, may trap Fe and even create chemical bonds between the Si and Fe atoms. It is known that Fe forms Fe silicide precipitates at GBs in Si and, hence, such an initial bond may act as a seed for precipitation of Fe-Si particles.

Another observation follows from the calculated DOS in Fig. 3.12: the electronic structure of interstitial Fe at GBs may differ significantly from that of interstitial Fe in bulk Si. For instance, the Fe atoms at the GB become non spin-polarized or the Fe d-states split into more than two levels. This is of particular relevance for experimental detection methods of interstitial Fe which rely on the energy position of the deep defect levels of Fe in the band gap, for instance μ-PL [97]. This position may vary for different GBs in Si and therefore segregated interstitial Fe may not be detected properly by such methods. In all cases a deep level from a Fe impurity remains in the band gap of Si and, hence, a previously inactive Fe-free GB in Si can become electrical active upon Fe segregation. If segregated Fe atoms accumulate and form Fe-Si precipitates at the GB, a band-like electronic state can develop instead of a single deep level. This is relevant for experimental methods such as deep level transient spectroscopy [52].

Our study was performed under the assumption that Fe atoms occupy interstitial positions at GBs. It cannot be excluded that Fe also substitute Si atoms at the GB. In bulk Si, interstitial Fe atoms occupy Si vacancies and become substitutional defects [125] but Si vacancies are very unlikely in bulk Si because they have large formation energies. However, this formation energy of Si vacancies is smaller at GBs, i.e. Si vacancies are

attracted by GBs [122, 126, 127]. The possibility for Fe to occupy Si vacancies at the GB sites may therefore be more likely than in bulk Si. GBs also attract other impurity elements[126, 128–131] that can modify the segregation behavior of Fe at the GB.

In addition to the considered low-Σ or large-angle GBs, there are random GBs and high-Σ or small-angle GBs as well, which all show a very strong attraction for the Fe atoms [95, 132]. The strong segregation can be explained by the interaction of Fe atoms with Si atoms which are not fourfold coordinated at the GBs, similarly as it was observed here for the symmetric Σ 3 (112) GB. The situation is different for small angle GBs. This type of GBs is composed of periodic interfacial Read-Shockley dislocation arrangements with not overlapping dislocation cores [133]. It is known that dislocations tend to reconstruct along their dislocation lines [108] and thereby avoid over- or undercoordinated Si sites. However, both bulk and GB dislocations have elastic strain fields surrounding them which may affect the segregation behavior of Fe atoms [44, 45, 95]. An elastic strain field is also observed around GBs which contain Fe precipitates [36, 44, 95]. However, in this case it is not evident whether the strain field is induced by the growth of the precipitate at the GB or it is present beforehand. The question how strain fields affect Fe impurities in bulk Si crystals is subject of the next section.

3.3 Diffusion of iron impurities in strained silicon crystals

In the previous section, we have studied the segregation of interstitial Fe impurities at a set of symmetrical tilt or twist GBs in Si. We were able to show that the segregation energies of Fe atoms at Si GBs are determined by rather subtle features of the local coordination and bonding. In addition to GBs, there also exist other extended defects such as dislocations. Dislocations are one-dimensional defects which consist of a dislocation core and long-ranged elastic stress and strain fields. But in a polycrystalline material, elastic strain can also originate from other sources such as precipitates, triple junctions of GBs, etc. Strain may influence the energy of interstitial Fe impurities and thus change their distribution in the polycrystalline material. Moreover, the diffusion properties of interstitial Fe may be affected due to a change of their migration barriers. To investigate these possibilities we study the influence of different states of elastic strain on interstitial Fe impurities in the following section.

The modeling of strain is achieved by the geometric deformation of the super cell. Various modes of strain have been applied such as shear or uniaxial strain. In order to describe the diffusion of Fe impurities, jump rates of Fe atoms are calculated from energy barriers along the minimum energy paths (MEPs), and from frequency factors that are obtained from phonon spectra. The jump rates are then transferred into a kinetic Monte Carlo simulation from which diffusion coefficients are extracted. In addition, also the temperature dependence of the formation energies for the different configurations are obtained by considering the vibrational entropy. The content of this section has been published in [1] (Ziebarth et al., Phys. Rev. B **92**, 115309).

3.3.1 Structural models

([1], Sec. II. B)

In all DFT calculations, a cubic diamond supercell with 64 Si atoms was used. Validation calculations for several structures with a larger supercell containing 96 Si atoms yielded identical results. The calculated equilibrium value of the cubic lattice constant is 5.467 Å which is in agreement with experimental (5.431 Å [134]) and other calculated data (5.469 Å [135]). Calculated values of the cubic elastic constants also agree reasonably well with experimental data (cf. Tab. 3.2; the deviations are typical for DFT results within the generalized gradient approximation).

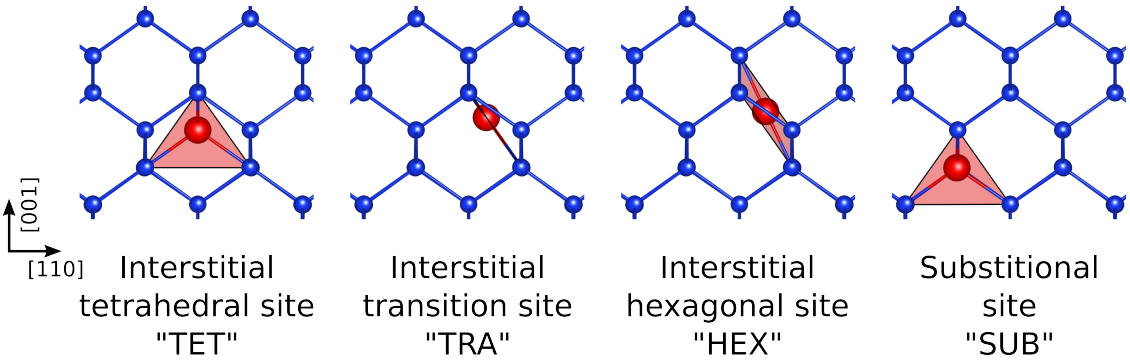

Figure 3.13: Four different configurations of Fe impurities (red spheres) in the diamond structure of Si (blue spheres) are shown. The local coordination shell is depicted as a red polyhedron. The pictures show a projection along the [110] direction.

3.3.2 Temperature dependence of defect formation energies for iron impurities

([1], Sec. III. A)

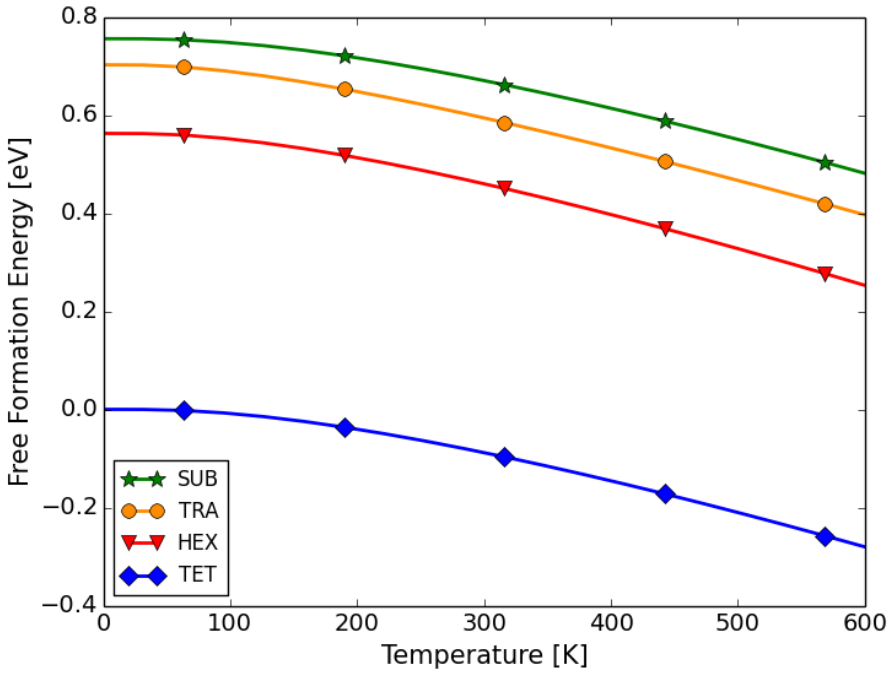

Figure 3.14: Temperature dependencies of the free energies of defect formation for the four different Fe defect configurations.

Previous studies [21, 83, 125] have shown that Fe impurities in bulk Si can be located in three different configurations. The Fe atom can occupy either interstitial sites with tetrahedral T_d or trigonal D_{3d} symmetries [137] (the trigonal site is commonly called 'hexagonal' due to its six Si neighbors) or Fe can substitute Si on regular sites. These three configurations are displayed in Fig. 3.13 together with a configuration of the transition state (marked as TRA in the following) between the tetrahedral and hexagonal sites

[GPa]	Calc.	Exp.[136]
C_{11}	149	165.6
C_{12}	59	63.9
C_{44}	99	79.5
B	89	97.8

Table 3.2: Cubic elastic constants and bulk modulus of bulk Si (in GPa).

(see discussion bellow).

In a perfect Si single crystal, the tetrahedral (TET) site is known to be energetically more favorable for the interstitial Fe than the hexagonal (HEX) site [83]. Our calculated energy difference between the TET and HEX configurations of 0.60 eV agrees well with the value of 0.57 eV obtained in previous DFT calculations [83]. It has also been reported that interstitial Fe atoms will preferentially occupy Si vacancies (forming substitutional (SUB) Fe defects) rather than forming a defect complex with the Si vacancy [125].

The formation energy E_{f} of a defect configuration can be calculated as

$$E_{\mathrm{f}} = E^{\mathrm{total}} - N_{\mathrm{Si}}\mu_{\mathrm{Si}} - N_{\mathrm{Fe}}\mu_{\mathrm{Fe}} \quad , \tag{3.3.1}$$

where E^{total} is the total (internal) energy of the supercell with the Fe impurity, N_{Si} and N_{Fe} are the numbers of Si and Fe atoms in the supercell, and μ_{Si} and μ_{Fe} are the chemical potentials for Si and Fe, respectively. In our calculations, μ_{Si} has been chosen to be equal to the chemical potential of Si in the crystalline equilibrium diamond structure, and μ_{Fe} such that the formation energy of an interstitial Fe atom at a tetrahedral site in a Si single crystal is zero. This corresponds to the Si-rich limit of the binary Si-Fe system. In unstrained Si, we obtained formation energies of 0.0, 0.70, 0.56, and 0.76 eV for all the TET, TRA, HEX, and SUB defects, respectively. The calculated values for excess volumes for these defects turned out to be negligibly small. The formation energy of a SUB defect includes the formation energy of the Si vacancy.

In order to take into account finite temperature effects, we also investigated the phonon contributions to the defect formation energies[138]. The phonon densities of states for the different defect configurations and for the perfect Si crystal were calculated, using the Phonopy software package [139], from the dynamical matrix obtained from finite atomic displacements in the harmonic approximation[138, 140]. Atomic displacements from equilibrium positions were set to 0.05Å. From the phonon density of states, it is straightforward to calculate the free energy of defect formation for a given temperature [141]. The calculated temperature dependencies of the free energies for the four defect configurations are shown in Fig. 3.14. Since all four curves look very similarly, the relative energy differences between the defect configurations are almost independent of temperature. Hence, it is reasonable to assume that temperature does not affect significantly the hierarchy of defect formation energies for Fe impurities in bulk Si, and therefore the temperature dependence is not further taken into account.

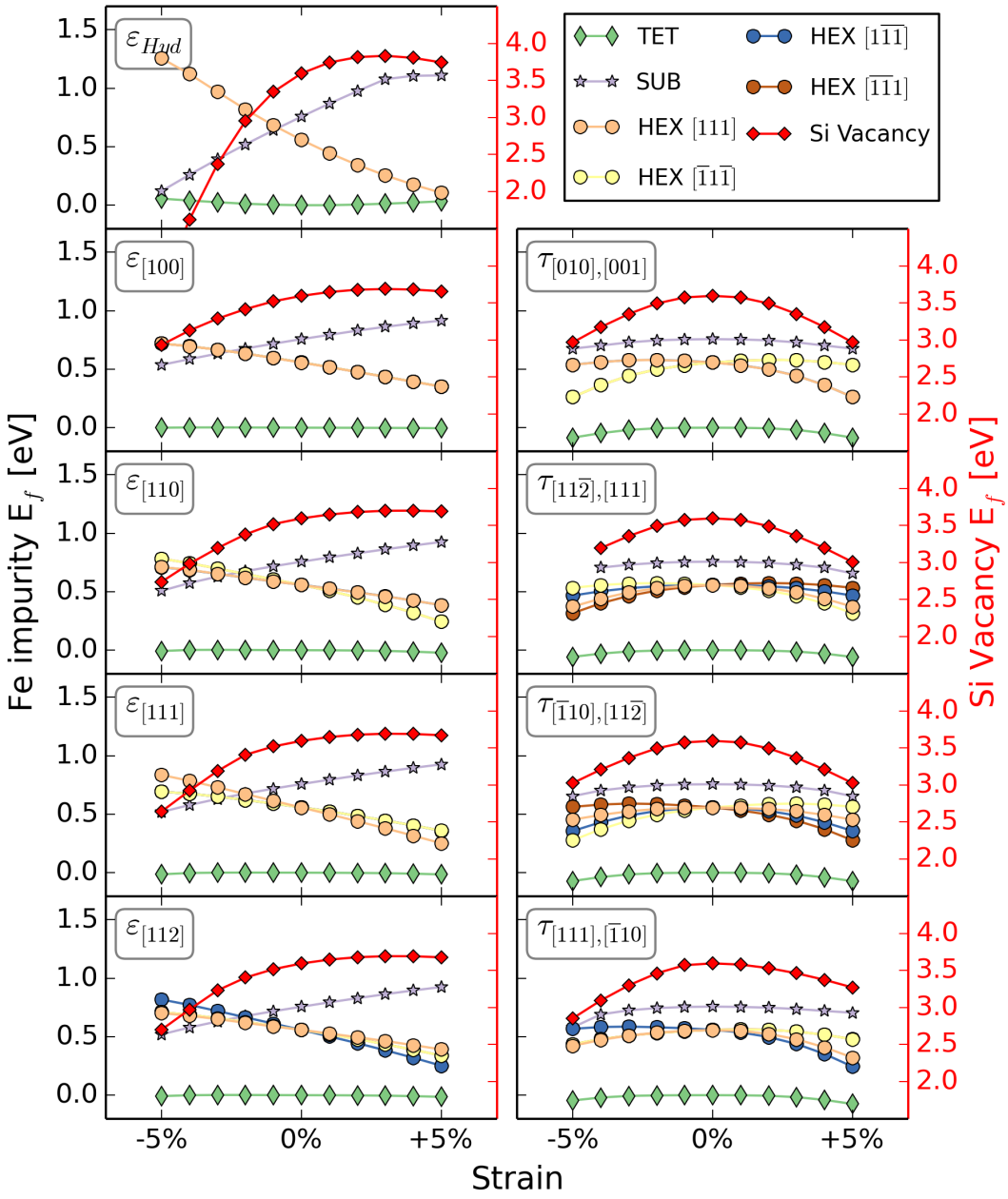

Figure 3.15: Formation energies of the different Fe defects and the Si vacancy in Si for different strain states. The energy scale for the Fe impurities is on the left side and the energy scale for the Si vacancy is on the right side. Negative strain corresponds to compression and positive strain corresponds to expansion.

3.3.3 The effect of strain on the defect-formation energy of iron impurities

([1], Sec. III. B)

In order to investigate the effect of elastic strain ε on the defect formation energies, different uniform strain states with strain magnitudes ranging between -5% and $+5\%$ were applied. The considered strain modes were: hydrostatic strain $\varepsilon_{\mathrm{Hyd}}$, uniaxial strains $\varepsilon_{[100]}$, $\varepsilon_{[110]}$, $\varepsilon_{[111]}$, $\varepsilon_{[112]}$, and shear strains $\tau_{[010],[001]}$, $\tau_{[11\bar{2}],[111]}$, $\tau_{[\bar{1}10],[11\bar{2}]}$, $\tau_{[111],[\bar{1}10]}$. Strain is applied by the deformation of the conventional cubic fcc unit cell with a lattice constant of a_0 and cell vectors [142]

$$\mathbf{a} = \begin{pmatrix} \mathbf{a_1} \\ \mathbf{a_2} \\ \mathbf{a_3} \end{pmatrix} = \begin{pmatrix} a_0 & 0 & 0 \\ 0 & a_0 & 0 \\ 0 & 0 & a_0 \end{pmatrix} \tag{3.3.2}$$

by applying a deformation matrix $\mathbf{D}$ such that new cell vectors $\mathbf{a}'$ are

$$\mathbf{a}' = (\mathbf{I} + \mathbf{D}) \cdot \mathbf{a} \qquad , \tag{3.3.3}$$

where $\mathbf{I}$ is the identity matrix. The deformation matrices are given in the Appendix. In addition to the formation energies of interstitial Fe defects, the formation energies of substitutional Fe defects and Si vacancies were also calculated. As mentioned above, the Si-vacancy + Fe-interstitial complex is not as stable as a Fe-substitutional unstrained Si, but this relative stability may be altered by applied strains. For the calculations of the formation energies under external strain, we always set the chemical potential of Si (μ_{Si} in Eq. 3.3.1) at the same strain state as for the perfect Si crystal containing the Fe

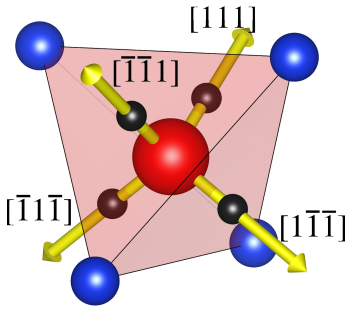

Figure 3.16: The interstitial tetrahedral site (red sphere) in Si is connected via hexagonal sites (small black spheres) in $\langle 111 \rangle$ directions with four neighboring tetrahedral sites.

impurity. The defect formation energies for all applied strain modes are displayed in Fig. 3.15. Note that the energy scales for the Fe impurities are different from that for the Si vacancy.

Due to the lattice symmetry, the tetrahedral interstitial sites in bulk Si remain equivalent for arbitrary homogeneous strain. In contrast, the hexagonal interstitial sites become nonequivalent depending on the strain state of the system. The four differently oriented hexagonal sites in the rectangular supercell system differ by the orientation of their large facet, which is orthogonal to one of the following four directions: [111], [$\bar{1}$11], [1$\bar{1}$1] and [11$\bar{1}$] (see Fig. 3.16). These four hexagonal sites are therefore labeled in the following by their directions from the tetrahedral site.

As displayed in Fig. 3.15, the formation energy for the TET configurations remains almost constant for all investigated strain states. The strain dependencies for the HEX configurations follow linear relations in the cases of hydrostatic and uniaxial strains. The largest change in the interstitial formation energies is for the hydrostatic strain, for Fe at the HEX site it changes by almost 1.2 eV over the range of $\pm 5\%$ strain. In the case of uniaxial strains, the changes are only by about 0.5 eV for the same strain range. For shear strains, the HEX formation energies depend non-linearly on the strain with maximum variations reaching also about 0.5 eV (e.g., for the $\tau_{[010],[001]}$). In all cases, there is at least one hexagonal site which shows a reduction in the formation energy during shear.

The formation energies for the Fe substitutional and the Si vacancy follow similar parabolic trends, but the variations are more pronounced for the latter. In all investigated cases, the transformation of a Fe-substitutional into an Si-vacancy + Fe-interstitial defect complex is unlikely because the formation energy for substitutional (SUB) Fe remains smaller than the sum of the formation energies of the interstitial TET Fe and the Si vacancy.

The formation energies for charged Fe^+ defects in Si have not been calculated because Fe^+ is mainly present in p-doped Si and forms defect clusters with shallow acceptors such as boron [21, 83]. In order to accurately describe the energetics and kinetics of charged Fe^+, it would therefore be necessary to consider such defect clusters of Fe with B. This is not in the scope of the present work.

3.3.4 Diffusion of iron in strained silicon
([1], Sec. IV. B)

To analyze the migration of Fe impurities in Si, we first determined the frequency factors for the TET $\rightarrow$ HEX and HEX $\rightarrow$ TET jumps from phonons according to Eq. 2.2.3 and Eq. 2.2.4. For the unstrained Si crystal, we obtained frequency factors of $\nu_{\text{TET}\rightarrow\text{HEX}} = 30$ THz and $\nu_{\text{HEX}\rightarrow\text{TET}} = 18$ THz. For simplicity, the frequency factors for Fe are taken to be the same as well for the strained cases in the following.

The MEPs and associated migration barriers for Fe jumps between the interstitial TET and HEX sites were calculated using the CI-NEB method for all investigated strain states but only for the three strain magnitudes of -5%, 0 and $+5\%$. For illustration, the MEPs for different uniaxial $[100]$ strains are shown in Fig. 3.18. The migration barrier decreases for tension and increases for compression. The HEX site corresponds to a local energy minimum and its relative stability with respect to the TET site depends strongly on the applied strain.

All computed energy barriers are compiled in Fig. 3.17. The reference energy barrier for Fe diffusion from a TET to a HEX site in unstrained bulk Si amounts to 0.74 eV while the barrier height for the reverse jump (HEX to TET) is only 0.19 eV. The largest changes in the energy barriers are observed for the hydrostatic strain. The energy barrier between the TET and HEX sites decreases to about 0.3 eV for $+5\%$ strain while the energy barrier for the reverse direction increases to about 0.25 eV. For negative strain of -5%, the energy barrier between the TET and HEX sites increases to about 1.20 eV, for the reverse direction the energy barrier almost vanishes. A similar but less pronounced change is found for uniaxial strain. Some of the deformations, e.g. uniaxial strain along the [111] direction, do not conserve the equivalence of the hexagonal sites, and thus, different energy barriers for different directions are obtained. For all shear strains, the migration barriers are reduced for both directions. Again, the magnitude of the reduction depends specifically on both the elastic shear direction and the geometric jump direction. This is of particular interest because it is not reflected in the formation energies shown in Fig. 3.15, i.e., the formation energy for the HEX site increases with strain whereas the energy barrier decreases for both jump directions.

To investigate the influence of the migration barrier changes on the diffusion of Fe, lattice-based numerical kMC simulations were employed. A rate table for the different migration directions was set up using Eq. 2.2.2 with the calculated energy barriers

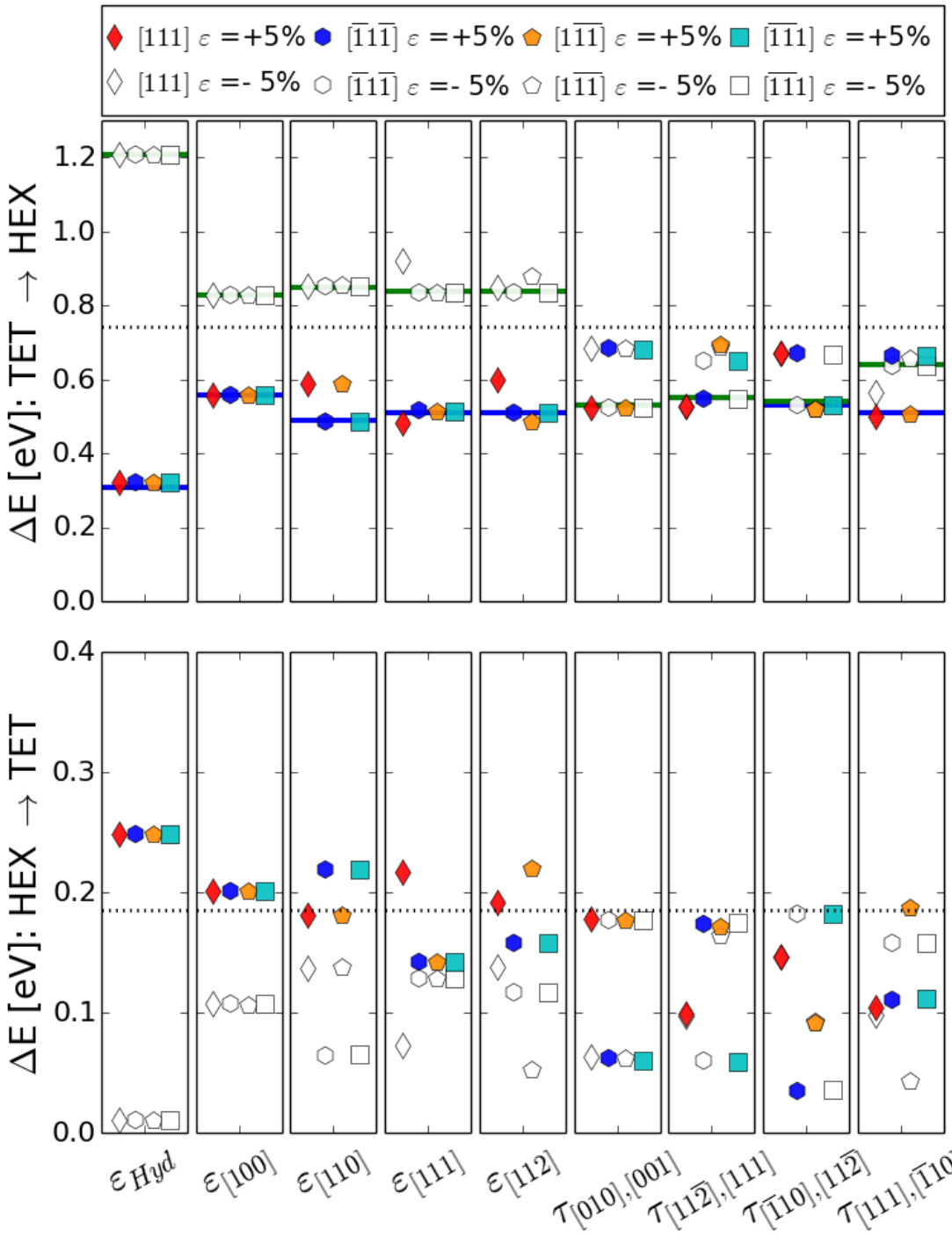

Figure 3.17: Energy barriers for forward and backward jumps between the TET and HEX sites obtained using CI-NEB calculations. The dashed line corresponds to the energy barrier for migration of Fe interstitials in unstrained bulk Si. The solid blue and green lines indicate to the effective energy barriers obtained from the kMC simulations.

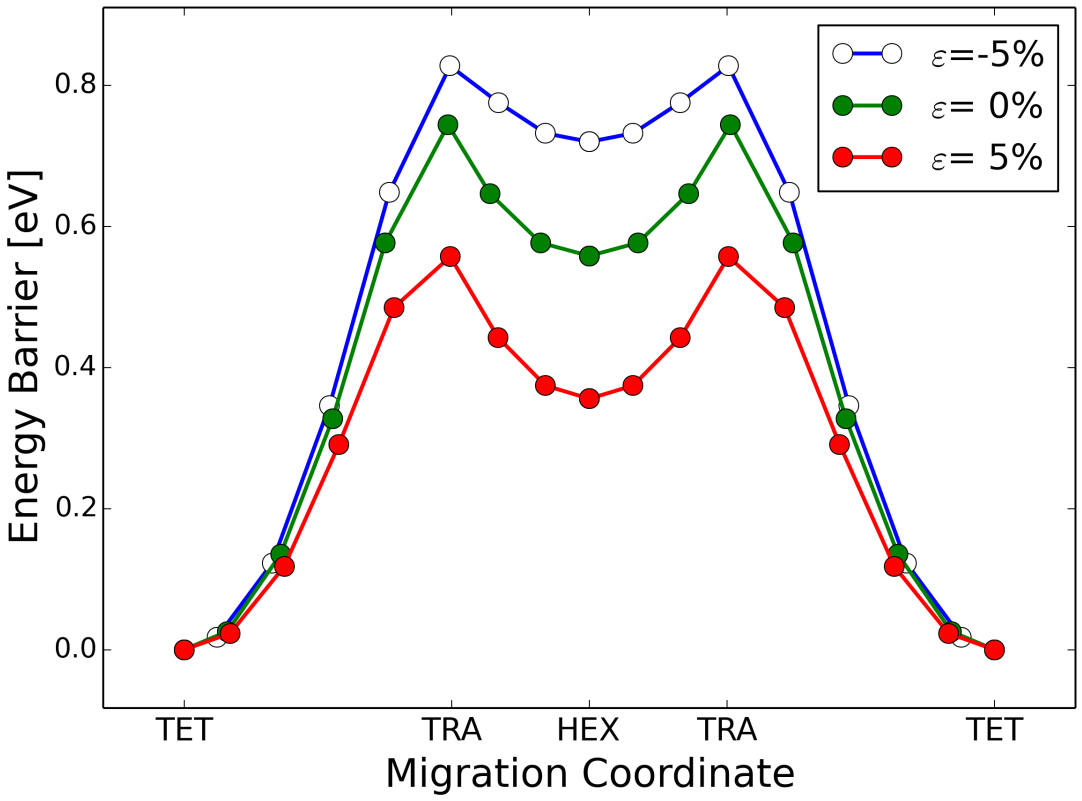

Figure 3.18: Minimum energy paths for interstitial Fe migration between two tetrahedral sites for different uniaxial [100] strains.

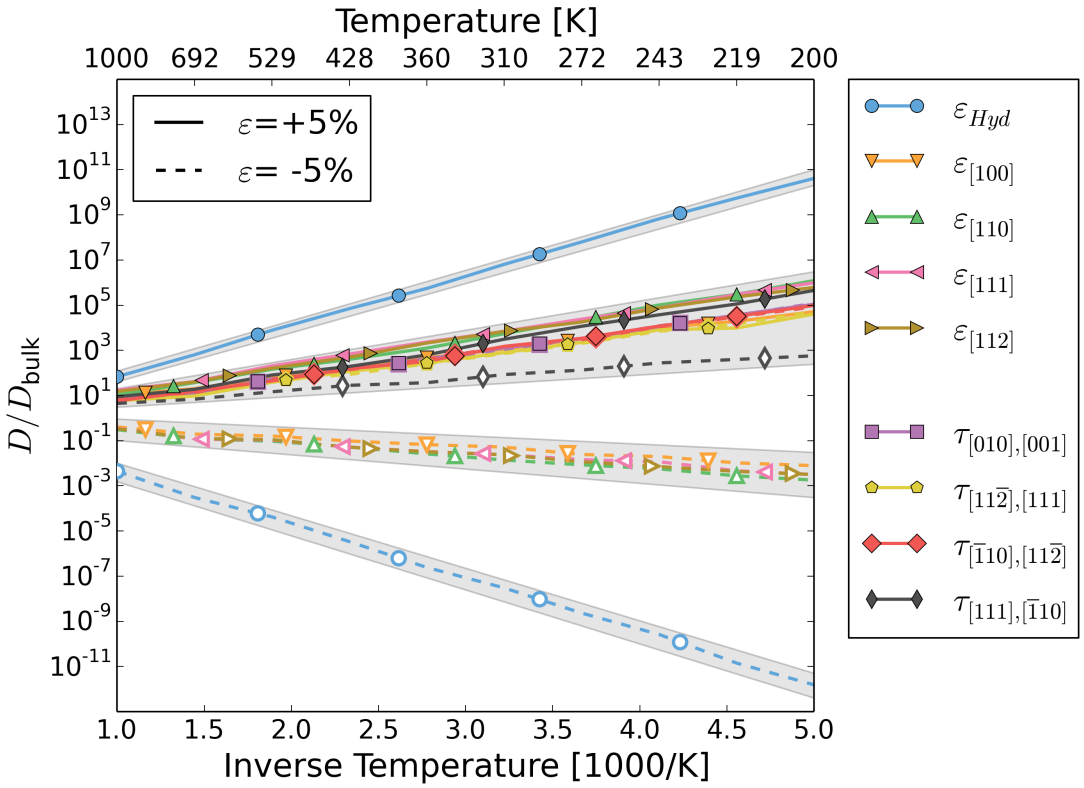

Figure 3.19: Temperature dependencies of relative diffusion coefficients (w.r.t. Fe diffusion in unstrained bulk Si) for all investigated strain states obtained from kMC simulations. The shaded areas emphasize data with quantitatively similar behaviors.

from Fig. 3.17 and the frequency factors given above for the unstrained supercell. The diffusion constants (with a standard deviation lower than 1%) for different strain states were obtained by averaging one hundred kMC runs (each having one million kMC steps) according to Eqs. 2.2.5-2.2.7.

Fig. 3.19 displays the temperature dependencies of the diffusion coefficient (with respect to the diffusion coefficients of interstitial Fe in unstrained bulk Si) for all investigated strain types. Despite the consideration of different migration directions and the strain-induced change of the crystal structure (symmetry), the Fe diffusion always follows an Arrhenius behavior. The effective energy barriers are included in Fig. 3.17 as green and blue solid lines. They only deviate slightly from the lowest energy barriers found for the TET→HEX migration. The reverse migration direction has no significant influence on the effective energy barriers. Beware that due to our simplification of setting the

frequency factors to those of the unstrained crystal, the intercepts may be inaccurate and, hence, they are not considered here. The results for D/D_{bulk} can be sorted into four quantitatively similar groups. The two extreme cases, i.e., strongly reduced and strongly enhanced diffusion, occur for $+5\%$ and -5% hydrostatic strain, respectively. The third group, consisting of compressive uniaxial strains, leads to a slightly lower diffusivity. The majority of the strain states, including all types of shear strain, form a fourth group that causes a moderately higher diffusivity.

3.3.5 Discussion
([1], Sec. VI)

The results of our DFT calculations show that the behavior of Fe atoms in a bulk Si crystal is not significantly affected by temperature. The temperature neither changes the stability hierarchy of the Fe defect configurations nor does it influence the predominant migration mechanism, i.e., the MEP and its energy barrier for migration of a Fe interstitial between the neighboring tetrahedral sites. This finding is consistent with experimental observations of only one operating mechanism for diffusion of Fe in Si over a wide range of temperatures [143].

It is still a matter of debate why Fe impurities are attracted by regions of large elastic strains [41–43, 45]. The stability of the most favorable configuration for Fe atoms occupying the interstitial tetrahedral sites in Si remains almost unaltered in the presence of realistic strain fields ranging within $\pm 5\%$ (cf. Fig. 3.15). Therefore, there is no thermodynamic driving force for the accumulation of Fe impurities in regions of large strain associated with high concentrations of dislocations or other extended crystal defects. This result is consistent with the experimental observation of Lu *et al.* that the gettering of interstitial Fe by the strain field of dislocations is very inefficient [55].

Nonetheless, the formation energies of other interstitial and substitutional Fe defects are affected by strain. Even though these configurations are not thermodynamically stable, they play a role in the diffusion of Fe impurities. We carried out extensive MEP calculations to study the effect of various homogeneous strains on the migration of Fe atoms in Si. The results for the energy barriers were then used for the parametrization of a mesoscopic kMC simulation model to obtain effective diffusion coefficients under various strain states and temperatures. The effects of different strain states could be classified into four groups (cf. Fig. 3.19). For all considered cases, the diffusion of Fe follows

an Arrhenius behavior with effective energy barriers close to that of the lowest energy barrier for the TET→HEX migration direction. Hydrostatic strains lead to the largest changes of Fe diffusion. For 5% hydrostatic expansion of the lattice the diffusion at room temperature becomes seven orders of magnitude faster than the diffusion in unstrained Si. An analogous reduction of the Fe diffusivity by eight orders of magnitude occurs for hydrostatic compression of the same magnitude (cf. Fig. 3.19). Similarly, all the uniaxial compressive and tensile strains also lead to a decrease and an increase of the Fe diffusion, respectively, albeit not to such dramatic ones. Rather surprising is our finding that a shearing of the crystal structure results always in an enhancement of the Fe diffusion, which is similar to that found for uniaxial tension. In summary, we observe an increase of Fe diffusion for all types of strain except for compressive strain.

The diffusion of Fe in n-doped Si under external uniaxial stress along [110] has been studied by Suzuki *et al.* [45, 46] using Mössbauer spectroscopy. The activation energy barrier for interstitial Fe diffusion was found to decrease from 0.68 eV to 0.33 eV for a stress of about 19 MPa at room temperature. Since the lattice strain corresponding to this stress is much lower than 1%, the expected change for the migration barrier is very small. According to our calculations, the reduction of the migration barrier to 0.35 eV requires an application of external hydrostatic stress of about 4.4 GPa (cf. Tab. 3.2), which is much higher that the reported stress value. A possible explanation of the experimental observations of Suzuki *et al.* may be related to large local stress associated with dislocation entanglements and their changes under external loading; unfortunately, no information about the dislocation distribution and arrangement was given.

3.4 Iron impurities in strain fields and at cores of dislocations in silicon

In the previous section, we have studied the influence of elastic strain on interstitial Fe impurities. Surprisingly, elastic strain only affects their diffusion but does not lead to their segregation. In the following section, we want to study the influence of dislocations on interstitial Fe atoms. Dislocations are line defects and consist of a long-ranged strain field and a short-ranged core region.

The long-range behavior of a dislocation can be described by an elastic strain field which decays with the distance from the core of the dislocation. In the previous section, the influence of strain on the migration of interstitial Fe was already thoroughly investigated. These results are now used to parameterize the strain-dependence of the migration barrier of an interstitial Fe atom. This parameterization is then used to examine the migration of Fe interstitials in the strain field caused by a dislocation which is obtained from the theory of linear elasticity.

The study of the core region of a dislocation, at which the atomic structure is heavily distorted from that of the perfect crystal, requires atomistic models. The core of the dislocation is a one dimensional defect and Si atoms rearrange and reconstruct as well at dislocation cores like they do at GB interfaces. For some types of dislocations, there are several reconstruction patterns which may be formed. Indications exist that a perfectly reconstructed dislocation, i.e. all Si atoms are four-fold coordinated at the dislocation core, is electrically inactive [52] and, hence, does not affect the efficiency of the solar cell. But dislocations can be decorated by metallic impurities and such a decoration makes the dislocation electrically active [34, 52]. This is of course important for the production of solar cells because electrically active defects reduce the efficiency of solar cells but dislocations also exist in other semiconducting devices which are made from monocrystalline Si. Electrically active defects may lead to complete malfunction of such devices.

The modeling of dislocations is even more difficult than the modeling of highly symmetric grain boundaries due to the long-ranged elastic stress and strain fields inherent

to dislocations. The elastic field of an individual dislocation cannot be represented realistically using supercells of treatable sizes with periodic boundary conditions. In our study, we adopted an arrangement of a dislocation quadrupole which cancels most of the elastic field at the boundaries of the supercell so that periodic boundary conditions can be applied. But we still have to use rather large supercells with more than 500 atoms. The large size of the supercell limits us to study only the few most stable configurations of interstitial Fe at the dislocation core.

In the following section, we report our results on the segregation of interstitial Fe and its local electronic structure at cores of dislocations. The first part of this section, in which the influence of the strain field of dislocations on Fe interstitials is investigated, has been published in [1] (Ziebarth et al., Phys. Rev. B **92**, 115309). The second part about the segregation of interstitial Fe impurities at cores of dislocations is in preparation for publication.

3.4.1 Dislocations in silicon

Dislocations are line defects accompanied by long-ranged stress and strain fields which, according to the continuum theory of linear elasticity, diverge at the dislocation centers [105]. In the region around the dislocation center, usually referred to as the dislocation core, linear elasticity ceases to be valid and non-linear elasticity [144] or the discrete atomic structure needs to be taken into account.

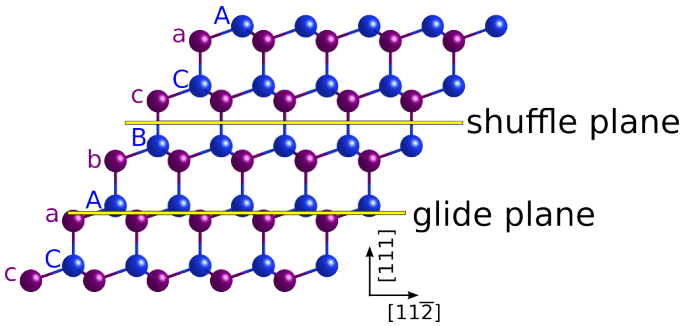

Figure 3.20: Stacking of the atomic {111} layers in the diamond structure of Si. Blue and purple spheres mark the Si atoms of the two fcc sublattices.

In the diamond structure of Si, perfect dislocations have Burgers vectors, $\mathbf{b}$, equal to $a/2\langle 110\rangle$, where $a = 5.47\,\text{Å}$ is the cubic lattice constant of Si. Experimental observations have revealed that there are only two types of perfect dislocations in Si – a pure

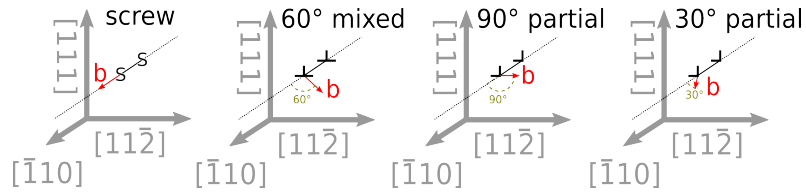

Figure 3.21: Orientation for the screw and 60° mixed dislocations and the 90° and 30° partial dislocations. The stacking fault associated with the partial dislocation is not shown here.

screw dislocation and a 60° mixed dislocation [108]. Both dislocations glide on the close-packed $\{111\}$ planes. Since the diamond structure is build from two face-centered cubic (fcc) sublattices, there is an alternating stacking ...AaBbCcAaBbCc... of the $\{111\}$ planes, where the layers labeled by uppercase letters belong to one sublattice and the lowercase letters denote layers of the other sublattice (see Fig. 3.20). These two sets of $\{111\}$ planes have also two distinct interplanar spacings. The narrowly spaced planes (aA, bB, cC) are called *glide* planes while the widely spaced planes (Ab, Bc, Ca) are called *shuffle* planes. The dislocation core can be, in principle, located between either of the planes [105, 145]. If the core is centered between the glide set of planes, it can dissociate into partial dislocations with Burgers vectors $a/6\,\langle 211\rangle$ according to [105, 108]

$$\frac{a}{2}[1\bar{1}0] \rightarrow \frac{a}{6}[2\bar{1}\bar{1}] + \frac{a}{6}[1\bar{2}1], \tag{3.4.1}$$

where the dissociated partial dislocations are connected by an intrinsic stacking fault of very low energy. The perfect screw dislocation dissociates into two 30° partial dislocations, while the 60° dislocation dissociates into one 30° and one 90° partial dislocation [108]. The dissociated dislocations are energetically favorable and have been confirmed by high-resolution transmission electron microscopy [108, 146]. These two partial dislocation cores (30° and 90°) were therefore chosen for our study of the interaction with the Fe impurities.

In the first part of this section, we focus on the interactions between the interstitial Fe impurities and the long-ranged strain fields of dislocations in Si. Core effects of partial dislocations are investigated in the second part of this section.

3.4.2 Iron in strain fields of perfect and partial dislocations ([1], Sec. V)

In this subsection, the interaction between the strain fields of dislocations and interstitial Fe impurities are studied. For simplicity, we treat the partial dislocations as individual objects since the strain field of the stacking fault is negligibly small relative to the strain fields of the cores. The crystallographic orientations for the dislocations are sketched in Fig. 3.21. The strain field of the screw dislocation has an axial symmetry and can be decomposed into shear strains τ_{xz} τ_{yz} along the dislocation line only [105]. The strain fields of the 60° mixed and the 30° partial dislocations have more complex symmetries as they consist of strain components with both screw and edge characters. The latter includes dilatational strains ε_x and ε_y and shear strain τ_{xy} perpendicular to the dislocation line [105]. The 90° partial dislocation is a pure edge dislocation with a corresponding strain field. Note that decompositions of dislocation strain fields into individual strain components are not unique but depend on the choice of the geometrical reference frame (for the orientations used here see Fig. 3.21).

In order to analyze the diffusion of Fe in the strain fields of the four dislocations, we first parametrized the changes of the migration barriers as functions of the relevant strain components. This was done by interpolating the barrier changes calculated for strains ranging between -5% and $+5\%$ (cf. Fig. 3.17) with a polynomial function. Results of these interpolations, showing the barrier change $e_s(\varepsilon) = \Delta E(\varepsilon)/\Delta E_{\text{bulk}}$ for the two dilatational and four shear strains needed for the dislocation strain fields, are presented in Fig. 3.22. The different colors in each graph correspond to migration pathways in the different $\langle 111 \rangle$ directions.

In linear elasticity, the total strain field at an arbitrary location in the field of the dislocation (outside of the dislocation core) is given by superposition of all strain components. The corresponding migration barrier at this location can be then written as

$$\Delta E(\varepsilon) = \Delta E_{\text{bulk}} \cdot \prod_{i=1}^{N_{\text{strain}}} e(\varepsilon_i) \qquad , \tag{3.4.2}$$

where N_{strain} is the number of strain components.

Fig. 3.23 shows the variations of migration barriers for Fe jumps along different $\langle 111 \rangle$ directions in the strain fields of all four considered dislocations. As expected, the most pronounced barrier changes are close to the dislocation cores, where the amplitude of

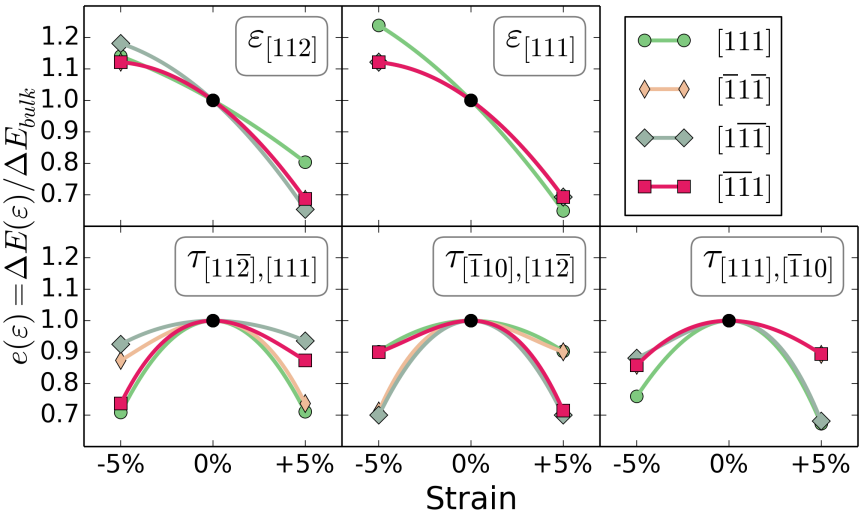

Figure 3.22: Parameterizations of the change of the migration barrier $e_s(\varepsilon)$ for strain component s and strain value ϵ by a polynomial function. Only strain components necessary for the dislocation strain fields are shown. The different colors represent the different $\langle 111 \rangle$ migration directions (of Fig. 3.21).

the strain field is largest. In case of the screw dislocation, the influence of the elastic field is rather short-ranged and the migration barrier differs less than 0.01 eV from the bulk value at a distance of 40 Å away from the dislocation core. For the 60° mixed dislocation, the influence of the strain field on the migration barrier is much more pronounced and its difference from the bulk value falls below 0.01 eV at a distance of about 150 Å away from the dislocation core (not shown here). The shear strain field of the screw dislocation leads only to a decrease of the migration barrier, whereas for the 60° mixed dislocation the migration barrier is increased in the compressive region (positive y-values) and decreased in the tensile region (negative y-values). The strain fields of both partial dislocations influence the migration barrier similarly as that of the 60° mixed dislocation, predominantly due to the edge components of their strain fields. The influence is more pronounced for the 90° partial dislocation than for the 30° partial dislocation due to the larger edge character.

For all dislocations, the migration barrier depends also on the migration direction which leads to direction-dependent shapes of the contour plots. Cross sections along the green dashed lines are shown in the right-most panels. For the 60° mixed dislocation and the two partial dislocations, different $\langle 111 \rangle$ migration directions have almost the same migration barriers in the tensile region, while in the compressive region the [111] migration

direction has a slightly larger migration barrier then the other three directions. However, in both cases the deviations between the different directions are hardly significant.

In order to estimate the influence of the strain field on the diffusion of interstitial Fe, we compare the ratio λ between the migration rate $\Gamma_{\text{local,direction}}(\mathbf{r})$, in different migration directions at a position $\mathbf{r}$ and the migration rate in bulk Γ_{bulk}. This ratio is given by

$$\lambda(\mathbf{r}) = \frac{1}{4} \sum_{\text{direction}} \frac{\Gamma_{\text{local,direction}}(\mathbf{r})}{\Gamma_{\text{bulk}}} = \frac{1}{4} \sum_{\text{direction}} \frac{\mathrm{e}^{-\Delta E_{\text{local,direction}}(\mathbf{r})/k_B T}}{\mathrm{e}^{-\Delta E_{\text{bulk}}/k_B T}} \quad , \tag{3.4.3}$$

where $\lambda = 1$ corresponds to a bulk-like migration while Fe migration is enhanced or decreased for $\lambda > 1$ or $\lambda < 1$, respectively. From λ angle-averaged rates are calculated. Since for all cases but the screw dislocation the migration behaviors are different in the two halfspaces above (a) and below (b) the glide plane of the dislocation (i.e. a: $y > 0$ and b: $y < 0$ in Fig. 3.23), separate $\overline{\lambda_{\text{a}}}(r)$ and $\overline{\lambda_{\text{b}}}(r)$ are calculated for these two regions. The angle-averaged $\overline{\lambda_{\text{a}}}(r)$ and $\overline{\lambda_{\text{b}}}(r)$ around the dislocation center are calculated from the ratio $\lambda(\mathbf{r})$ in Eq. 3.4.3 according to:

$$\overline{\lambda_{\text{a}}}(r) = \int_0^{\pi} \lambda(r,\theta)\mathrm{d}\theta \tag{3.4.4}$$

and

$$\overline{\lambda_{\text{b}}}(r) = \int_{-\pi}^{0} \lambda(r,\theta)\mathrm{d}\theta \tag{3.4.5}$$

where r and θ are the polar coordinates of $\mathbf{r}$ in a plane perpendicular to the dislocation line, and the half spaces above and below the glide plane are denoted by the subscripts a and b.

In Fig. 3.24, we show the results of $\overline{\lambda_{\text{a}}}(r)$ and $\overline{\lambda_{\text{b}}}(r)$ for the different dislocations at $T = 100$ and 300 K. In the lower half space (left panels) the migration of Fe is enhanced in all cases. The 60° dislocation has the largest influence on the migration. In the upper half space (right panels) only the screw dislocation leads to an increase of the diffusion which is the same for the upper halfspace. The compressive strain fields of the other tree dislocations lead to a decrease of the diffusion.

The influence of the screw dislocation has the shortest range. This is reflected in the

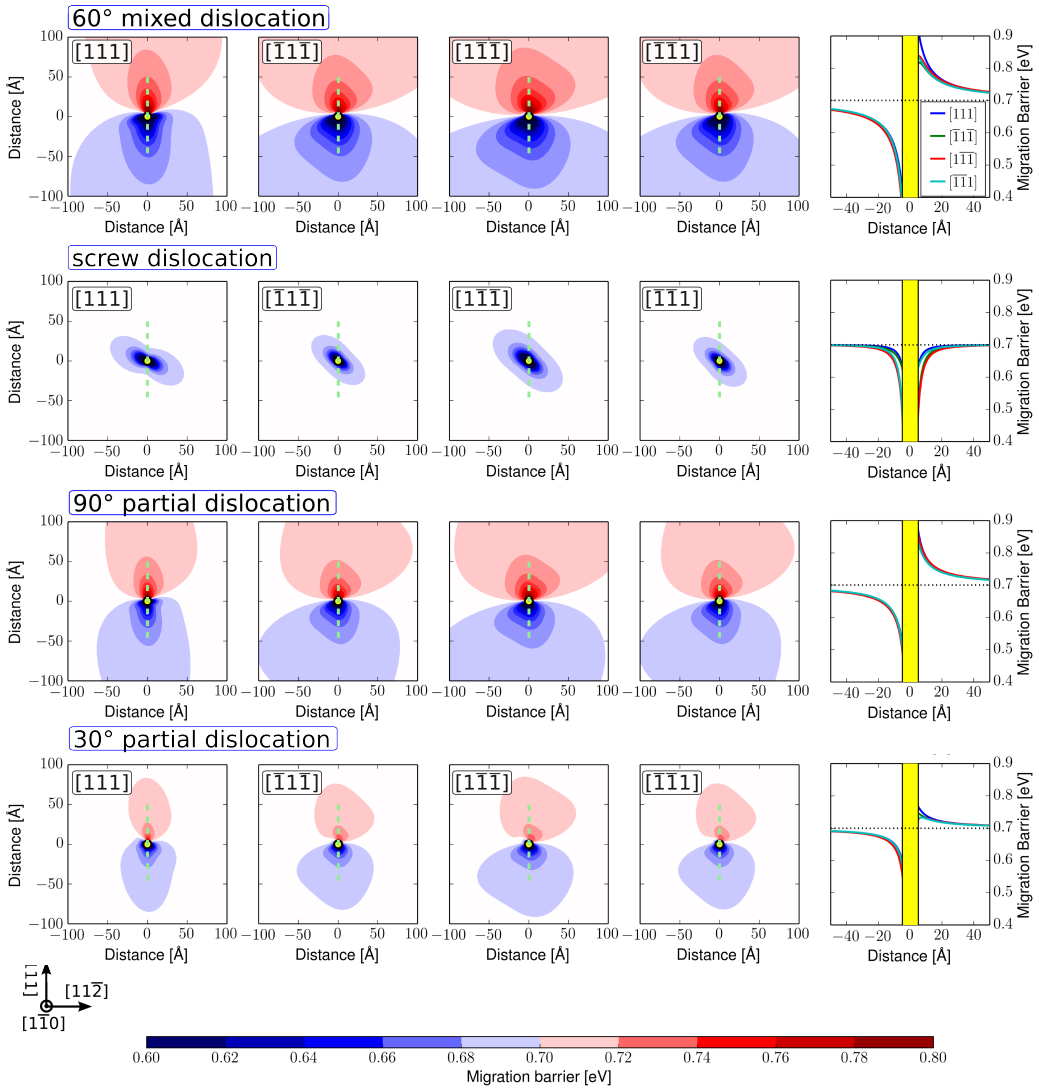

Figure 3.23: Migration barrier for interstitial Fe impurities in the strain field of a 60° mixed dislocation, screw dislocation, 90° partial dislocation, and 30° partial dislocation for different migration directions. The yellow circles indicate the core region of the dislocation (radius chosen to be 5 Å) where our model is not applicable due to core effects. The panels on the right show cross sections along the dashed green lines marked in the contour plots. The dotted horizontal black line indicate the migration barrier for Fe in bulk Si.

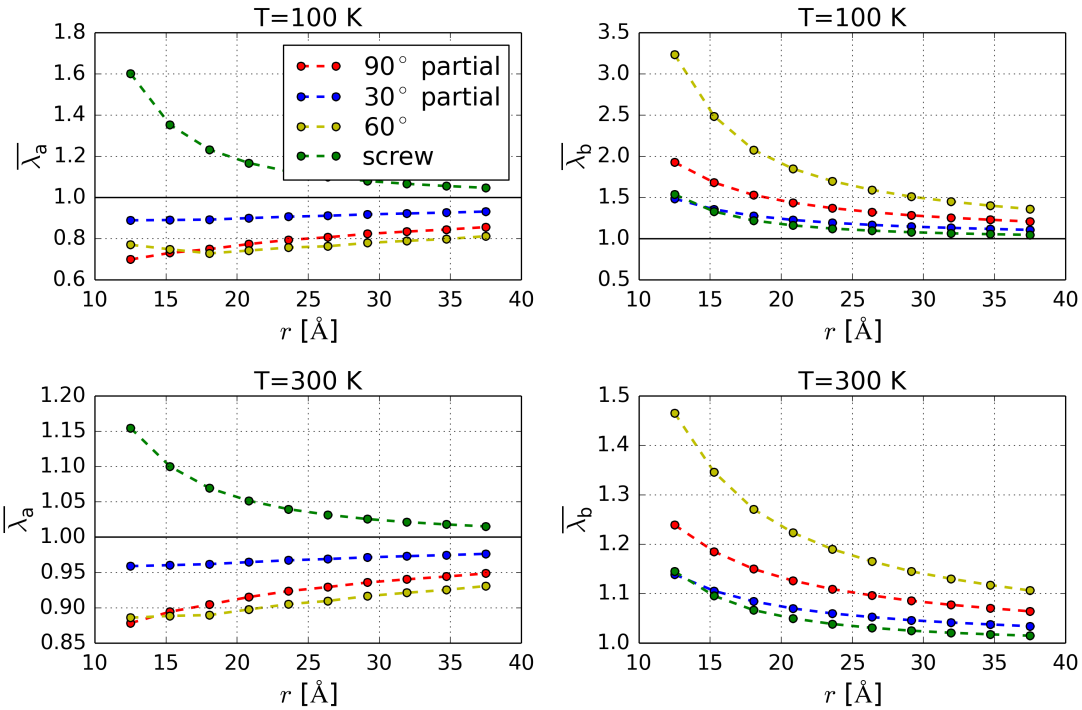

Figure 3.24: Angle-averaged distance-dependent ratios between migration rates of interstitial Fe around dislocations and in the perfect crystal of Si in the two halfspace above (a) and below (b) the glide plane of the dislocation for the two temperatures $T = 100\,\mathrm{K}$ and $T = 300\,\mathrm{K}$.

decay of $\overline{\lambda_a}(r)$ and $\overline{\lambda_b}(r)$ as a function of r. For the screw dislocation it approaches the bulk value faster than for the 90° and 30° dislocation. The influence of the 60° dislocation has the longest range.

With increasing temperature, the influence of the strain field on the diffusion is less pronounced. While $\overline{\lambda_a}$ is about 2.5 at a radius $r = 15\,\text{Å}$ for the 60° dislocation at $T = 100\,\mathrm{K}$, it is only 1.35 for $T = 300\,\mathrm{K}$.

3.4.3 Atomistic models of dislocations

To study the interaction of interstitial Fe impurities with the cores of dislocations, atomistic models have to be constructed which are small enough so that they can be treated within the DFT approach. Since dislocations require supercells with a large number of atoms, we limit ourselves to the most important types of dislocations, namely the partial 30° and the partial 90° dislocation, because most perfect dislocations are dissociated.

The long-range elastic stress and strain fields of dislocations make it challenging to simulate dislocations using small periodic supercells, which are treatable by electronic structure calculations. In our previous study [1], we investigated the interaction of Fe impurities with the long-range elastic fields of dislocations using a combined atomistic/kinetic Monte Carlo approach. In the present work we can focus on the core region and study the segregation of Fe only close to the dislocation cores. We therefore employ a common supercell geometry with a quadrupole arrangement of dislocations (see Fig. 3.25). In this periodic arrangement of dislocations, most of the long-range stress and strain fields of the individual partial dislocations are cancelled in the region between the dislocation cores [147–151]. A nonrectangular supercell with two dislocations of opposite Burgers vectors is a suitable atomic representation for such a dislocation arrangement. We used supercells containing 512 Si atoms, which were found to be sufficiently large to obtain correct core configurations without any spurious interactions. The thickness of the supercell along the dislocation line amounted to $4a[1\bar{1}0]$ to enable the investigation of different Fe concentrations (see below).

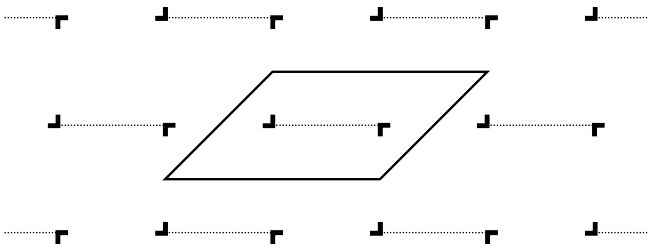

Figure 3.25: Schematic view of the periodic arrangement of dislocations. The supercell contains a dislocation dipole of partial dislocations which forms a lattice of dislocation quadrupoles when the supercell is periodically repeated. The dashed lines correspond to the stacking faults connecting the partial dislocations.

It is known that both cores can undergo reconstructions along the dislocation line [108]. The unreconstructed and reconstructed configurations of the 30° partial core are shown in Fig. 3.26). The unreconstructed core of the 30° partial dislocation is not stable and reconstucts spontaneously during relaxation of the supercell [152]. For the partial 90° dislocation, there exist at least two different core configurations, termed as the single period (SP) and the double period (DP) reconstruction, shown in Fig. 3.27 [111, 153]. Both the SP and DP reconstructed cores of the 90° partial dislocation are metastable. We found the SP core to be about 0.08 eV/Å more stable than the DP core, in agreement with other DFT studies of Benneto et al. (0.10 eV/Å) [153] and Valladares et al. (0.04 eV/Å)

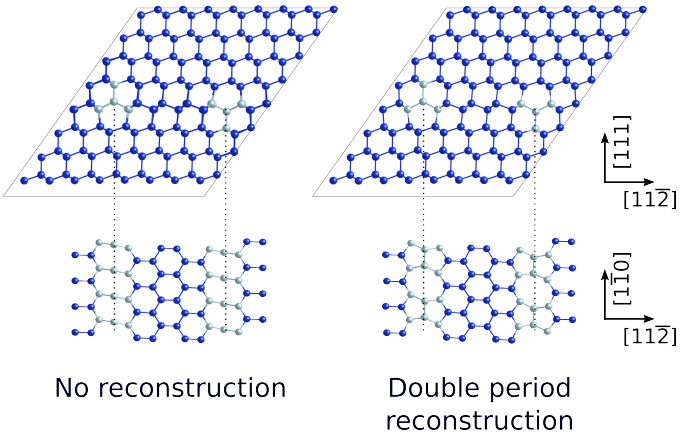

Figure 3.26: Supercell models of the 30° partial dislocations with different core structures. The upper panels show the dislocations oriented along the dislocation line, the bottom panels show the reconstruction patterns of the dislocations. Blue spheres indicate Si atoms; light blue spheres indicate Si atoms which form the core of the dislocation. The dashed lines are guides to the eyes.

[111].

3.4.4 Segregation of iron impurities at dislocation cores

Atomic structure and energetics

In the following, we focus on the interaction between the interstitial Fe impurities and the two partial dislocation cores. As mentioned in Sec. 3.4.3, we employed a large supercell with a period of $4a[1\bar{1}0] = 4\boldsymbol{\xi}$ along the direction of the dislocation line, $\hat{\boldsymbol{\xi}} = \boldsymbol{\xi}/\xi$, in order to be able to examine to which extent the segregation as well as the core structure are influenced by Fe concentration. Our setup allows to vary the Fe concentration from 1 to 4 Fe atoms per core in the supercell. The investigated impurity concentrations then correspond to 0.25, 0.5 and 1.0 Fe atom$/\xi$.

To investigate the energy landscape of Fe inside the dislocation core, we first inserted a single Fe atom at different positions along the dislocation line. Initially, only the position of the Fe atom was relaxed while the positions of the Si atoms were kept fixed. Then the low-energy configurations were selected and full structure optimizations were carried out using the BFGS algorithm [154]. The relaxed Fe positions were then used for the construction of initial supercells containing 2 or 4 Fe atoms in the core. These

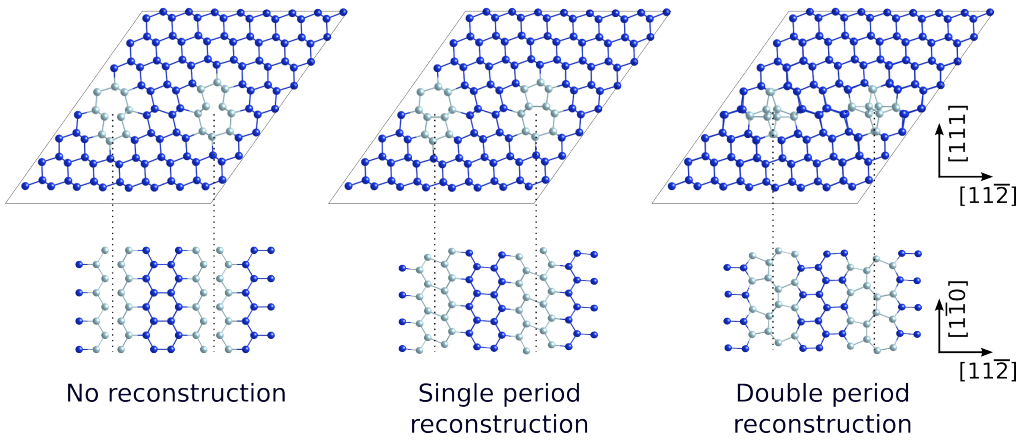

Figure 3.27: Supercell models of the 90° partial dislocations with different core structures, displayed in the same way as in Fig. 3.26.

supercells were then also fully relaxed. The most stable configurations of Fe impurities at all investigated dislocation cores are shown in Fig. 3.28.

For all configurations, segregation energies were obtained according to

$$E_{\mathrm{Fe}}^{\mathrm{seg}} = \frac{E^{\text{with Fe}} - E^{\text{without Fe}} - N_{\mathrm{Fe}}\mu_{\mathrm{Fe}}}{N_{\mathrm{Fe}}} \tag{3.4.6}$$

where $E^{\text{with Fe}}/E^{\text{without Fe}}$ is the total energy of the Si dislocation supercell with/without an Fe atom, N_{Fe} is the number of Fe atoms in the supercell, and μ_{Fe} is the chemical potential, which is set to the total energy of an interstitial Fe atom in a perfect bulk Si crystal. Note that within this definition a negative segregation-energy value favors segregation while no segregation is expected for a positive value.

The absolute value of the segregation energy (cf. Fig. 3.28) is largest for the SP and DP reconstructions of the 90° partials and smallest for the reconstructed 30° partial. For all dislocation cores, the segregation energies for impurity concentrations of 0.25 and 0.5 Fe atom/ξ are very similar. This indicates that the interaction energy between the Fe atoms is negligible for these concentrations. In contrast, for the largest concentration of 1 Fe atom/ξ, we observe that the segregation energies decrease significantly, i.e., the segregation becomes more favorable for the weakly attractive DP reconstruction and the 30° partial.

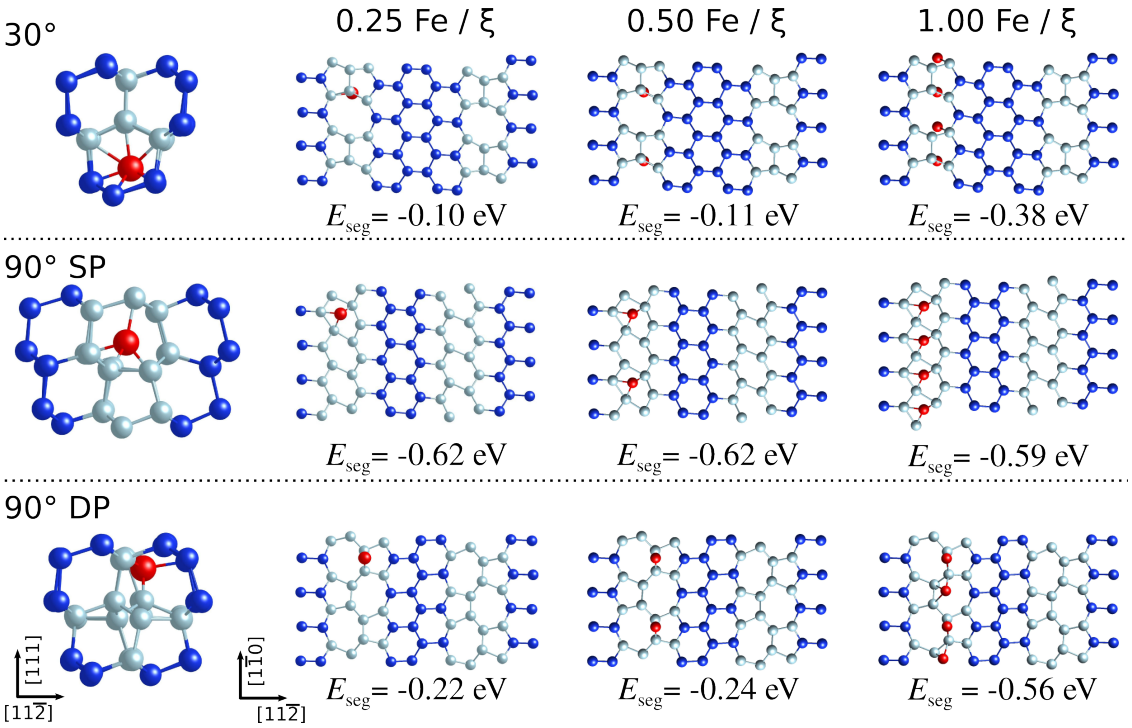

Figure 3.28: Atomic structures of the most stable configurations of segregated Fe impurities (red spheres) at investigated cores. The left column shows the location of the Fe atom viewed along the dislocation line for a concentration of 0.25 Fe atom$/\xi$. The other columns show the location of the Fe atoms from a top view for increasing Fe concentrations. Blue spheres indicate Si atoms, light blue atoms indicate Si atoms that correspond to the dislocation cores.

Electronic structure analysis

The electronic densities of states (DOS) of the three considered dislocation cores (cf. Fig 3.28) without and with segregated Fe atoms are displayed in Fig. 3.29. For comparison, also the DOS for the perfect Si crystal without and with interstitial Fe at a tetrahedral interstitial position is shown. For the d-states of Fe, projected DOS have been calculated. In Fig. 3.29, they are displayed as gray-shaded areas. A decomposition of the d-states into cubic t_{2g} and e_g contributions is included (red and blue lines, respectively) in Fig. 3.29. For the interstitial sites at the dislocation cores this decomposition is only approximate since the Si atoms surrounding the Fe interstitial do not have a perfect cubic (octahedral or tetrahedral) symmetry. The orbital directions for the projection were chosen to be same as those for the perfect Si crystal.

In agreement with previous studies [2, 21, 83], our calculations yield for interstitial Fe

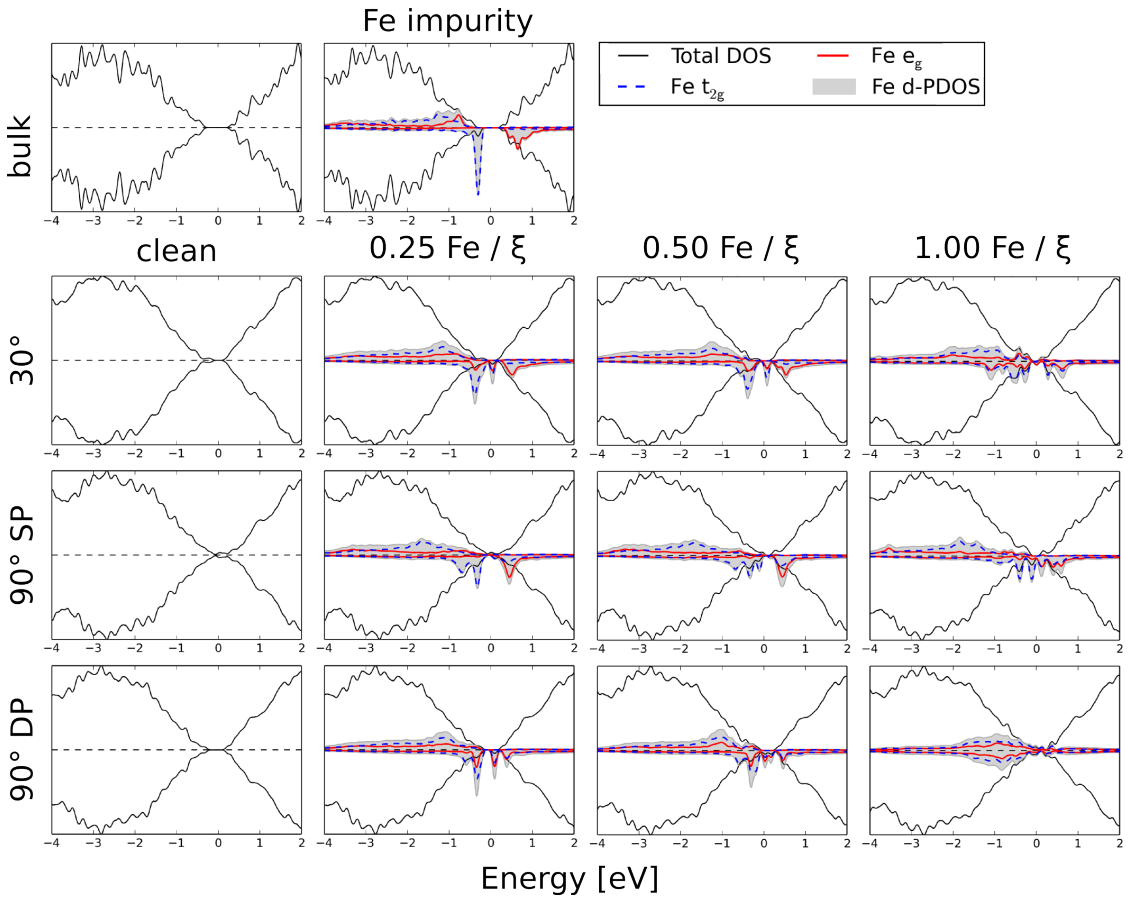

Figure 3.29: Total and projected electronic densities of states for the bulk crystal and the 30° DP, 90° SP, and 90° DP dislocation cores without and with segregated interstitial Fe for different impurity concentrations. For clarity, the projected densities of states of the states of Fe are scaled.

in bulk Si that two electrons are transferred from 4s to 3d states. This leads to a filling of the d-states of Fe by eight instead of six electrons per Fe atom. Moreover, the high-spin configuration for the Fe atom is favored such that the spin-up d-states are completely filled and the spin-down d-states are partially filled by three electrons. The tetrahedral crystal field of the surrounding Si atoms splits the spin-down states into t_{2g} and e_g states. The t_{2g} states are located above the edge of the valence band and correspond to the deep defect states known from several studies [2, 21, 83]. The e_g states are shifted to the conduction band and remain unoccupied.

In the case of a clean 30° partial dislocation, the band gap is narrowed but still open. For Fe concentrations of 0.25 and 0.5 Fe atom/ξ, the segregated Fe creates several gap states that cannot be clearly discriminated as t_{2g} and e_g states. While the first peak is still at the

same position as the t_{2g} states of Fe in bulk Si, an additional peak appears in the band gap about 0.4 eV higher in energy.

For the clean 90° partial dislocation with SP core, the band gap is closed while with DP core it remains almost the same as in bulk Si. This feature of chemical bonding is likely reflected by the higher energy of the SP core compared to the DP core. The partial d-DOS of segregated Fe for the SP core at the two lower concentrations are similar to that of interstitial Fe in bulk Si, but one of the t_{2g} states is shifted to a lower energy. The local electronic structure of the DP core is similar to that of the 30° partial.

For all three dislocation cores, the highest concentration of 1 Fe atom/ξ induces much more significant changes in the electronic structure as the atom-like d-states start to broaden to a crystal-like d-band. For the case of the DP core of the 90° dislocation, the system even becomes spin-unpolarized and thus qualitatively very different from those with the lower impurity concentrations.

3.4.5 Discussion

([1], Sec. VI)

The obtained dependencies for the migration barriers on the applied strain were utilized to analyze the diffusional behavior of Fe interstitial in the strain fields of the perfect screw and 60° mixed dislocations as well as of the partial 90° and 30° dislocations in Si. Due to the shear character of its strain field, the perfect screw dislocation always enhances the Fe diffusion in its vicinity. However, the effect is rather short-ranged, within a radius of less than 4 nm. In contrast, the perfect 60° mixed dislocation enhances Fe diffusion on one side and impedes it on the other side, since the migration barriers are increased in the compressive and reduced in the tensile regions of the dislocation (cf. Fig. 3.23). The barriers are systematically influenced by strain even beyond 15 nm from the dislocation center, i.e., within a significantly larger region than around the screw dislocation.

Both partial dislocations behave qualitatively similarly as the 60° mixed dislocation although the barriers are affected within a smaller range (smaller for the 30° than for the 90° partial dislocation). A superposition of the effects of the two partials can be used to determine whether dissociated dislocations alter the migration barrier differently than the perfect dislocations. Since the dissociated 60° mixed dislocation is composed of the 30° and the 90° partials separated by less than 5 nm, its overall effect on the migration

barrier is qualitatively same as that of the perfect dislocation. In contrast, the dissociated screw dislocation will influence the migration barrier of Fe markedly differently than the perfect dislocation, since two 30° partials have both screw and edge characters. The dissociation in this case therefore gives rise to regions of inhibited and enhanced Fe diffusivity around the screw dislocation. For all dislocations the most pronounced changes of the migration barriers occur close to the dislocation cores where the stresses and strains are largest.

We investigated the segregation of interstitial Fe atoms at three most relevant core structures of partial dislocations in Si. In all considered configurations, the Fe interstitials are attracted to the dislocation cores. The segregation energies do not depend on the impurity concentration if it remains lower than 0.5 Fe atom$/\xi$, i.e. the Fe atoms are separated by at least $2\boldsymbol{\xi}$ and are uniformly distributed along the dislocation line. For these concentrations, the system can be considered to be in the dilute limit. This is supported by the calculations of the electronic densities of states which look almost identical for the impurity concentration of 0.25 and 0.5 atom$/\xi$ (cf. Fig. 3.29). In the dilute limit a rather small segregation energy of about -0.10 eV is found for the 30° partial dislocation. For the 90° partial dislocation, a much lower (higher in the absolute value) segregation energy is found for the SP core (-0.62 eV) than for the DP core (-0.22 eV). For higher concentrations of 1 Fe atom$/\xi$, one can see that the segregation energy is significantly different for the 30° and 90° DP cores. For the SP core of the 90° dislocation, the segregation energy almost does not change.

In order to analyze how the thermodynamic stability of dislocation is affected by the segregation of impurity atoms, we computed the relative line energies for both clean and Fe-containing dislocations. For the clean dislocations, the relative line energy η_0 is calculated as

$$2\eta_0 = \frac{E^{\text{without Fe}} - E^{\text{ref}}}{4\xi} \tag{3.4.7}$$

where the factor 2 accounts for the presence of two dislocations in our supercells. E^{ref} is an arbitrarily chosen reference energy. For the 30° dislocation, the natural reference is the energy of the clean dislocation so that $\eta_0 = 0$. For the 90° dislocations we chose the SP core energy as the reference so that the line energy of the more stable LP core is lower and negative. We can then determine the relative line energies of the Fe-decorated

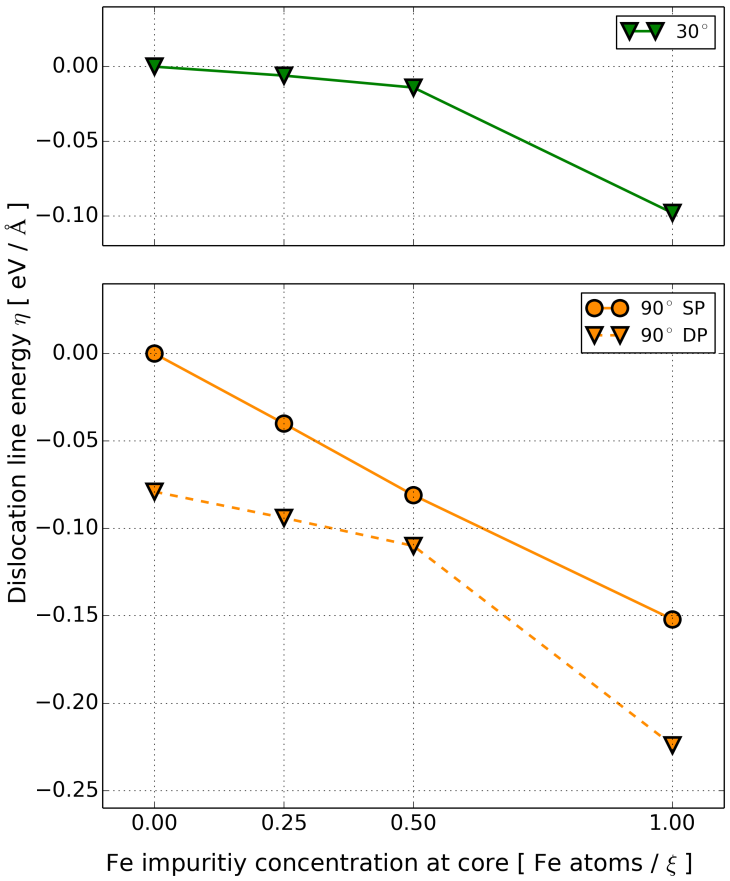

Figure 3.30: Relative dislocation line energy as a function of Fe impurity concentrations along the dislocation line.

dislocation cores as:

$$\eta = \frac{E^{\text{with Fe}} - N_{\text{Fe}}\mu_{\text{Fe}} - E^{\text{ref}}}{4\xi} - \eta_0 \tag{3.4.8}$$

This formula corrects for a double-counting contribution since in our supercells only one of the two dislocations is decorated with Fe atoms.

The results are summarized in Fig. 3.30 for both cores types. For the 30° core, the relative dislocation line energy is only weakly dependent on the concentration, with a marginal decrease at high concentration. For the 90° dislocations the concentration dependence is much more pronounced. It is close to linear in both cases and the relative line energies of both cores decrease significantly with increasing Fe concentration. Nevertheless, the relative thermodynamic stability of the reconstructed SP and DP cores remains unaltered, with the DP core being more stable at all Fe concentrations.

The electronic densities of states for an impurity concentration of 1 Fe atom/ξ reveal a formation of broader d-bands that indicate chemical interaction between the Fe impurities. For the DP core of the 90° dislocation, the system becomes non-spin-polarized. This behavior has already been observed in previous studies of segregated Fe impurities at large-angle grain boundaries, and it may indicate an initial stage of formation of iron silicide [2]. Our results show that large concentrations of Fe impurities at the dislocations are favored which implies that local clustering of Fe impurities at the dislocation line is possible even at low total Fe concentrations. Such clustering would again favor an iron-silicide nucleation.

Our findings for the Fe segregation at dislocation cores in Si are in accordance with experimental reports [54, 55]. However, the segregation mechanism at the atomic scale is different than that expected by some of the experimental studies. For instance, Lauer *et al.* [54] assumed that the Fe interstitial binds to a dangling bond present in the core of a 60° dislocation, but this core structure is not energetically favorable [108]. Moreover, it is likely that dislocations in Si dissociate under normal conditions as it was observed using HRTEM by Reiche *et al.* [146]. Our results clearly show that Fe segregation at the dissociated dislocations is not only possible but also energetically favorable.

The electronic structure of Fe atoms segregated at dislocation cores is different from that of interstitial Fe impurities in bulk Si. For an individual Fe impurity at each of the considered dislocation cores, we can identify a Fe-related deep electronic defect level at about $E_\mathrm{V} + 0.40\,\mathrm{eV}$ (E_V stands for the highest energy of the valence band). This peak is located in the same energy range as the deep level for interstitial Fe in bulk Si [83, 155–158]). Moreover, a second peak appears for all stable cores (90° DP and 30° dislocation core) which originates from the Fe d-states and is located 0.42 eV higher in energy , i.e. at $E_\mathrm{V} + 0.82\,\mathrm{eV}$. This peak may explain the metal-related deep level observed by deep-level transient spectroscopy (DLTS) at $E_\mathrm{V} + (0.77 \pm 0.03)\,\mathrm{eV}$ [52, 159, 160]. However, in these studies, the first deep level at $E_\mathrm{V} + 0.40\,\mathrm{eV}$ does not appear in the measured DLTS data. Another DLTS study by Lu *et al.* reported a deep level only at $E_\mathrm{V} + 0.42\,\mathrm{eV}$ but the deep level at $E_\mathrm{V} + (0.77 \pm 0.03)\,\mathrm{eV}$ was not observed [55]. Our calculations suggest that indeed both deep levels should be present. However, the electronic structure of Fe impurities at dislocation cores may be influenced by other conditions such as additional impurity elements, intrinsic defects at the dislocation line, etc.

Hence, a possible extension of this study is to consider also the interaction of interstitial Fe impurities with other point defects at the dislocation cores. For instance, Matsubara *et*

al. showed that the local concentration of H at dislocations can be significantly increased and thus the formation of FeH pairs in the dislocations may become possible [114] and can affect the local electronic structure of the decorated dislocation.

Our findings show that diffusion around dislocations is enhanced. Therefore, Fe atoms can be transported easily to regions of higher dislocation densities. However, the preferential segregation of Fe has to occur within the core region. The segregation of interstitial Fe impurities is possible at all the considered cores of partial dislocations in Si, but the segregation energy of Fe depends strongly on the type of dislocation. The segregation energies for Fe atoms are largest for the SP core of the 90° dislocation, but the 90° dislocation still favors the DP reconstructed core even with segregated Fe. In all stable cases, an additional peak of Fe d-states is observed in the density of states.

For completing the study of Fe atoms at cores of dislocations it will be necessary to take the kinetics of Fe atoms at the dislocation cores into account. However, this will require calculations of MEPs in the dislocation-core region using the atomistic models which were addressed in this section. But the computational resources necessary for this would have been too extensive for this work. In the future such a computation may become doable and its results may be useful to extend our kMC simulation to obtain the Fe distribution around the whole dislocation including its core. Moreover, these calculations will also help clarifying whether if the dislocation core acts as a pipe-diffusion channel along the dislocation line for Fe in Si, as observed for instance for Si in Al [161].

4 Potential-induced degradation in solar cells

4.1 Sodium in stacking faults of silicon

In this section, sodium decorated stacking faults (SFs) are investigated. These were recently identified as the primary cause of potential-induced degradation in Si solar cells due to local electrical short-circuiting of the p-n junctions. In this section, we investigate these defects by first-principles calculations based on density functional theory in order to elucidate their structural, thermodynamic, and electronic properties. The content of this chapter has been published in [3] (Ziebarth *et al.*, J. Appl. Phys. **116**, 093510 (2014)).

4.1.1 Introduction

([3], Sec. I)

In recent years, silicon-based photovoltaic devices have become exceedingly important as an alternative way of generating electricity without using fossil fuels, and a lot of effort has been spent to improve the efficiency of the Si-based solar cells. For instance, techniques have evolved in order to lower the concentrations of impurities (e.g. iron impurities, cf. last chapter) that reduce the lifetime of photo-induced charge carriers. But efficiency is not the only quantity which is required for the successful application of photovoltaic devices as large-scale power generators. A long lifetime and high reliability of photovoltaic power plants is at least as important as the efficiency of the solar cells. To ensure this, it is particularly important to understand in detail possible failure mechanisms occurring during device operation.

One class of failure mechanisms is the so-called potential-induced degradation (PID) [28–30], which leads to a significant efficiency loss of Si-wafer-based photovoltaic cells at high operating voltages. An important sub-class of PID is associated with the formation of so-called shunts [57, 162] that reduce the parallel resistance R_p [29]. The shunts occur in both polycrystalline Si and single-crystalline Si modules composed of soda lime glass, ethylene vinyl acetate and an anti-reflective coating (SiN_x) [29, 163]. Recent experiments using time-of-flight secondary-ion-mass spectroscopy and scanning electron microscopy [164, 165] revealed that the shunted areas are associated with stacking faults (SF) inside Si and sodium precipitates at the $SiN_x/SiO_x/Si$ interface. Very recently, Na decorated stacking faults terminating at Si surfaces have been observed by high-resolution transmission electron microscopy (HRTEM), cf. Fig 4.1 [56]. The amount of Na in the stacking fault was estimated to be about one monolayer, decorating completely the SF plane. Since the formation energy of the (111) stacking fault in Si is very low, these defects can extend throughout the p-n junction of a solar cell. However, it is unclear how Na affects the SF properties. In the light of the experimental evidence, it is speculated that Na-decorated SFs may become electrically conductive and thus present the key agents of PID via short-circuiting of the Si p-n junction [56].

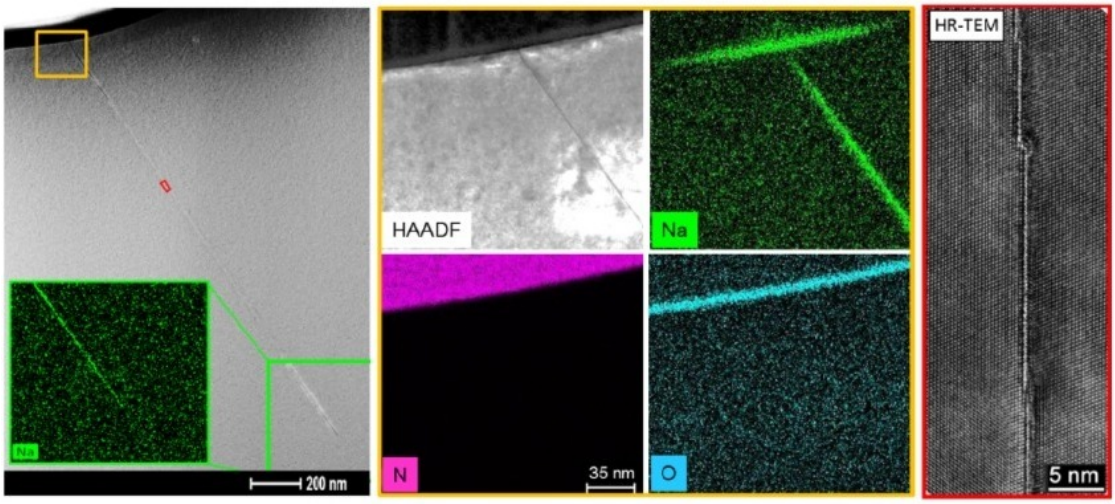

Figure 4.1: Transmission electron microscopy and energy-dispersive X-ray spectroscopy observation of a Na-decorated SF in Si. Picture taken from [56].

In the present study, we investigate the structure and energetics of Na-decorated stacking faults in Si by calculations based on density functional theory (DFT) [62, 63]. We address the questions of how Na diffuses into the SF of Si and what is the mechanism responsible for the short-circuiting of the p-n junction.

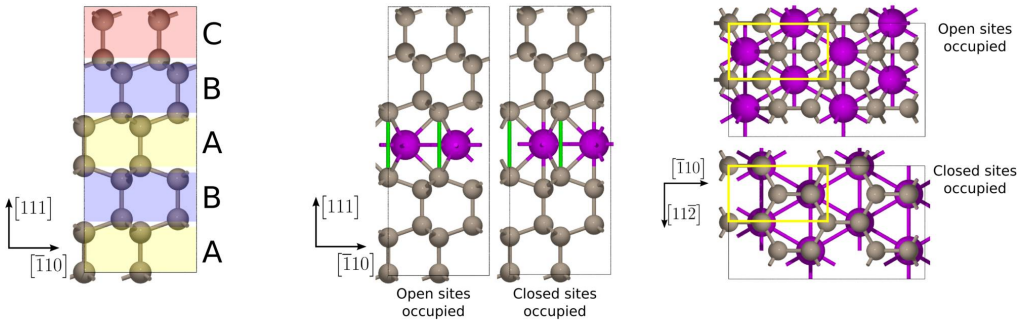

(a) intrinsic stacking fault (b) Na decorated stacking fault (c) topviews of (b)

Figure 4.2: Atomic structure of the intrinsic stacking fault in Si (a); the normal ordering ABCABC is disrupted due to a missing C plane into ABABC. Relaxed atomic structure of the Na-decorated SF projected along the [11$\bar{2}$] direction (b) and along the [111] direction (c). The extended Si-Si bonds (length of about 1.96 Å) across the SF are marked by green lines in panel (b). The yellow box in panel (c) indicates the supercell used in the calculations.

4.1.2 Atomistic models of sodium-decorated stacking faults

([3], Sec. II. B)

In order to obtain reference configurations, we first computed properties of ideal (111) SF in Si with and without Na, using bulk supercell models with periodic boundary conditions applied in all directions (see Figs. 1 and 2). Based on the experimental evidence, the amount of Na atoms in the SF was set to one monolayer.

For calculations of Na diffusion into the SF, additional supercell models containing a single (111) SF terminating at free (100) surfaces were created. The surfaces were separated by at least 14 Å of a vacuum region in order to avoid spurious interactions between the surfaces. To simplify the calculations, SiO_x or SiN_x reaction phases at the Si surfaces were not taken into account. Instead, all bare Si surface atoms were passivated with hydrogen atoms in order to saturate the Si dangling bonds, or one of the surfaces was fully covered by a thick layer of Na (cf. Fig. 4.8).

Sodium at the stacking fault

([3], Sec. III. A)

Structure and energetics A model of an intrinsic (111) stacking fault in Si is obtained simply by removing a pair of adjacent atomic (111) planes. The supercell used

in our calculations is shown in Fig. 4.2. It contains 20 Si atoms and was tested to be sufficiently large for a reliable description of SF properties. We found the length of the Si-Si bond across the SF to be only 0.02 Å larger than that of the equilibrium Si-Si bond (2.37 Å). The computed SF energy of 3 meV / Å^2 (discussed later in this section) agrees well with other theoretical calculations and experimental measurements [166–168].

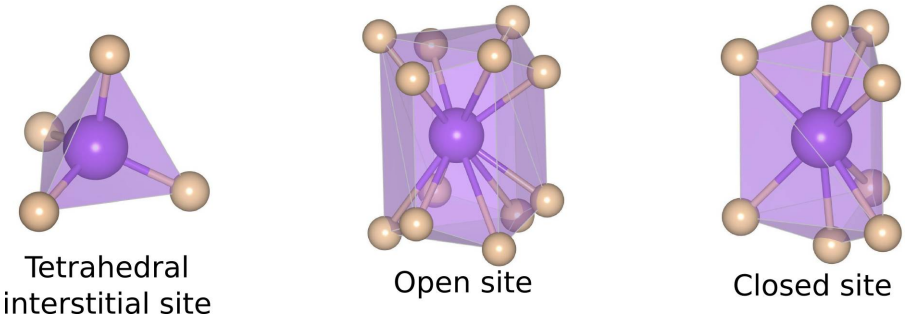

Figure 4.3: Three possible interstitial sites for Na in Si bulk and SF. The tetrahedral interstitial position is the most stable configuration in bulk Si. The open and closed structures with 16 and 12 surrounding Si atoms, respectively, exist at SF and the $\Sigma 3$ (111) GB.

In order to investigate the energetics of Na-decorated SFs, interstitial Na atoms were subsequently added to the SF. Fig. 4.3 shows three types of interstitial sites that exist in bulk Si and in the intrinsic SF. The 12-fold and 8-fold coordinated interstitial sites at the SF, termed as "open" and "closed", differ clearly from the tetrahedral site in bulk Si.

For our choice of the supercell dimensions, it was possible to study two configurations: (i) with one Na atom per SF area, which corresponds to a half-filled SF, and (ii) with two Na atoms per SF area, which completely fill all available sites in the SF (cf. Fig. 4.2). For both configurations the atomic positions as well as the cell dimensions were relaxed. We also tested different initial positions of interstitial Na atoms, but the final configuration was found to be always the same, namely, with Na atoms occupying the open sites at the SF. In contrast, the atomic structure of the SF depends sensitively on the Na concentration. In the case of the half-filled SF, the presence of Na atoms leads to only a very small extension (0.08 Å) of the Si-Si bonds across the SF. The situation is markedly different for the fully-filled SF where the bond length across the SF (cf. green bonds in Fig. 4.2 (b)) is extended by 1.96 Å with respect to the bulk bond length. This expansion of the Si lattice is confined to the Si-Si bonds across the SF while the length of the more remote Si-Si bonds in the supercell remains almost unaltered.

In addition to the SF, we also investigated Na segregation at the $\Sigma 3(111)$ symmetric tilt

grain boundary (GB) in Si, which is closely related to the SF, and at the (111) plane in bulk Si with the same Na concentration as in the fully-filled SF. In both cases, the presence of Na causes similar local stretching (1.9 Å) of the Si-Si bonds as for the SF.

In order to compare the energetics of the investigated planar defects, we computed the interface energies as

$$E_{\text{interface}} = \frac{E^{\text{tot}}_{\text{defect}} - N_{\text{Si}}\,\mu_{\text{Si}}}{A}, \tag{4.1.1}$$

where $E^{\text{tot}}_{\text{defect}}$ is the total energy of the supercell containing the defect, N_{Si} is the number of Si atoms in the system, μ_{Si} is the chemical potential of Si in its most stable crystal structure (diamond structure), and A is the area of the planar defect.

The obtained interface energies of 3 and 2 meV/Å^2 for the SF and the $\Sigma 3$ grain boundary, respectively, are similar and very small, as already reported in literature [166, 167]. Such small values can be explained by negligible changes in the bond lengths and bond angles in both defects compared to the perfect crystal structure.

The normalized formation energies of interstitial Na atoms were calculated as

$$E_{\text{form}} = \frac{E^{\text{tot}}_{\text{with Na}} - E^{\text{tot}}_{\text{without Na}} - N_{\text{Na}}\,\mu_{\text{Na}}}{N_{\text{Na}}}, \tag{4.1.2}$$

where N_{Na} is the number of Na atoms in the system, μ_{Na} is the chemical potential of Na, and $E^{\text{tot}}_{\text{with Na}}$ and $E^{\text{tot}}_{\text{without Na}}$ are the calculated total energies for the systems with and without Na, respectively.

Fig. 4.4 shows the calculated formation energies of Na in Si bulk and SFs as a function of Na chemical potential. The chemical potentials of Na in different systems relevant to the present study are marked by arrows, cf. Fig. 4.5. All values were calculated using DFT with the reference zero value corresponding to Na in its equilibrium body-centered cubic (bcc) structure. As the surfaces of the Si wafers are usually parallel to the (100) planes, one of the configurations is a single Na atom on a free (100) 1x1 surface of Si. The chemical potential of this system is almost 1 eV lower than that of bulk bcc Na. Since the Na atoms arrange as a layer at the Si surfaces, we also consider a free monolayer of Na atoms arranged in a triangular and square lattices. The chemical potential of both these lattices is almost the same and not very different from that of the reference state. In reality, the Si surfaces of the solar cells are oxidized and hence covered by a thin amorphous layer of silicon oxide. Since first-principles calculations of

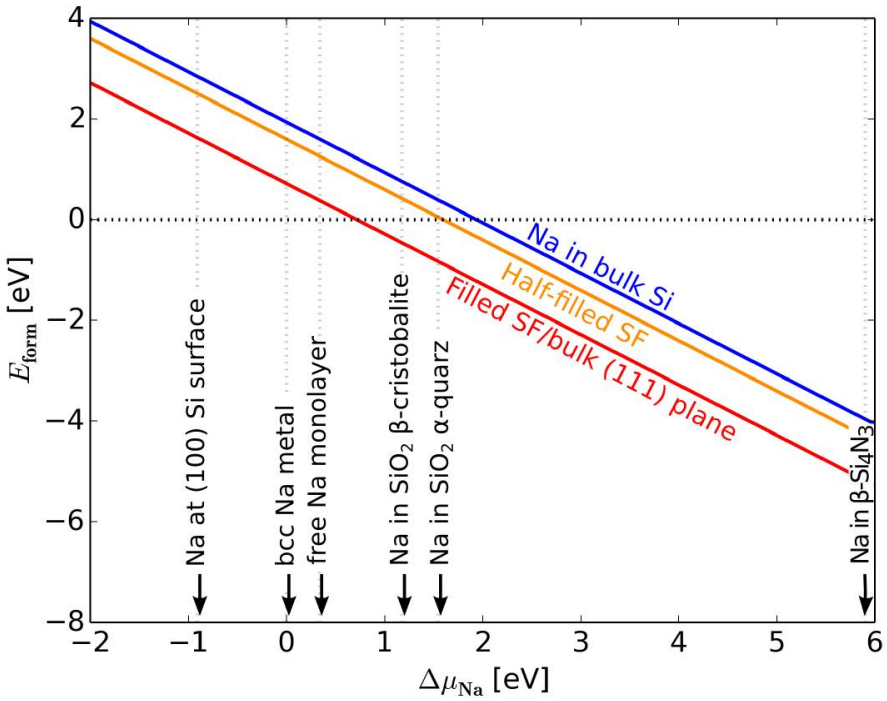

Figure 4.4: Na formation energy as a function of the chemical potential of Na. The Na chemical potentials for relevant configurations are marked by arrows.

amorphous structures are computationally too demanding, the energy of interstitial Na in two different crystalline silicon oxide structures (α-quarz and β-cristobalite) has been calculated instead. Finally, the solar cells also contain an anti-reflection coating made of amorphous silicon nitride. Again, as amorphous silicon nitride is out of the scope of this study, we used crystalline β-silicon nitride as a representative phase for determination of the Na chemical potential in this layer. The calculated Na chemical potentials in both oxide phases and especially in the nitride phase exceed significantly that of the bulk Na.

The results in Fig. 4.4 clearly show that it is thermodynamically more favorable for Na to segregate at a SF than to remain in bulk Si. The energy needed for a Na atom to segregate into a half-filled SF is about 0.34 eV lower than that in bulk Si. The formation energy then further decreases by about 0.88 eV when Na fills completely the SF or the (111) plane. Based on these thermodynamical arguments, it can be expected that Na will prefer to form a continuous atomic layer rather than a dispersed distribution of independent atoms. We observed that there is no significant difference between Na at the SF, $\Sigma 3$ (111) GB, and the bulk (111) plane. However, as will be discussed below, the Na diffusion behavior

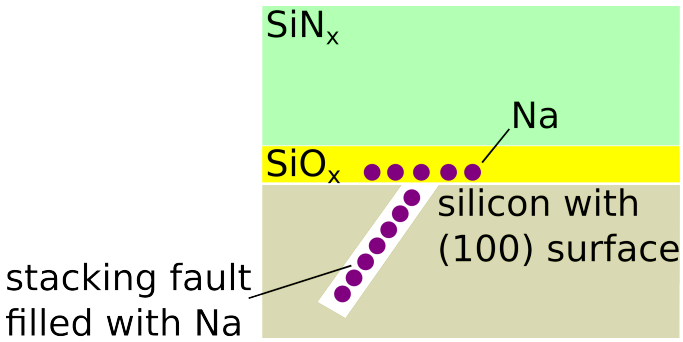

Figure 4.5: Relevant environments for Na in the context of PID as obtained from Fig. 4.1 .

at these defects is different.

Electronic properties Fig. 4.6 shows the electronic total density of states (DOS) and atomic site-projected density of states (PDOS) for the SF fully occupied with Na. We also calculated the DOS of an empty SF (not shown), but it does not significantly differ from that of the perfect Si crystal. Once the Na monolayer is embedded into the shuffle plane of the stacking fault, two peaks appear in the DOS. One peak (marked as Peak I in Fig. 4.6) is located about 1 eV below the Fermi level, while the other peak (marked as Peak II in Fig. 4.6) coincides exactly with the Fermi energy.

The origin of these two peaks can be analyzed using the PDOS curves (a)-(c) in Fig. 4.6. The PDOS of the Si atom located far away from the stacking fault (green line corresponding to atom (c) in the inset) has an almost bulk-like DOS with some finite density left at the Fermi energy. The PDOS of the Si atom located at the stacking fault (orange line corresponding to atom (a) in the inset) contains two peaks that coincide exactly with the new peaks in the total DOS. These peaks are also discernible in the PDOS of the second Si layer below the SF (red line corresponding to atom (b) in the inset), but are less pronounced. Additional DOS calculations carried out for a larger supercell with Si atoms separated by at least 8 Si-layers from the SF showed a perfect agreement with the DOS of c-Si.

A local charge analysis around the Na atoms within their ionic radius of 0.99 Å [169] revealed that no significant remaining charge is present at the Na atoms. Hence, the 3s valence electrons of the Na atoms are completely delocallized and transferred to the Si environment.

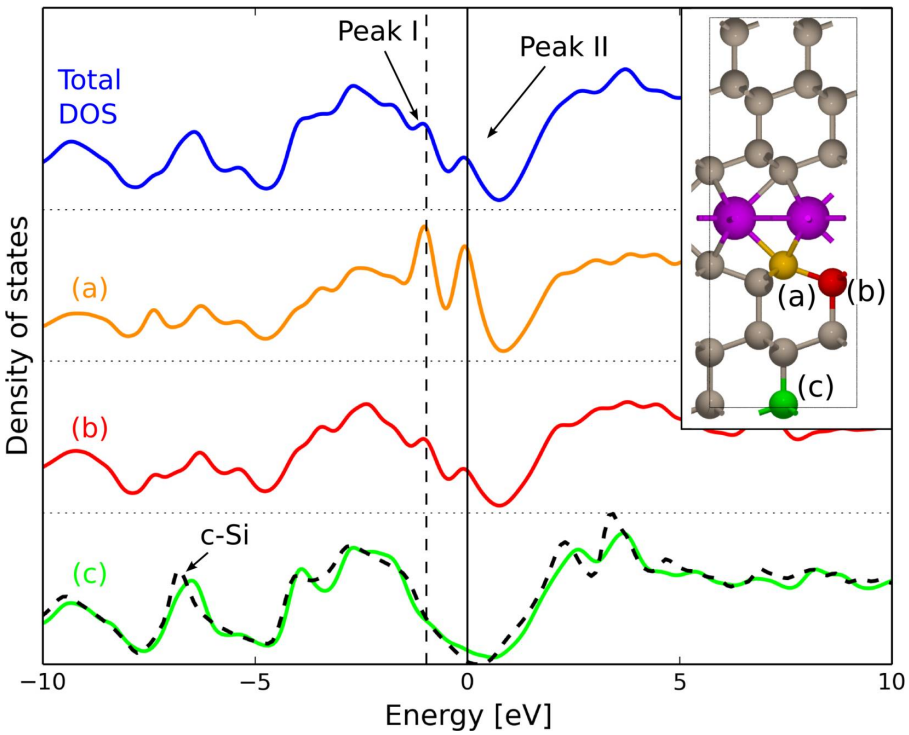

Figure 4.6: Total DOS (top panel) and PDOS (panels (a)-(c)) of the SF filled with Na. The PDOS are scaled by a factor of 3 in order to make their features better discernible. The PDOS are colored and labeled in the same way as the associated atoms in the inset. The total DOS of the perfect Si crystal (c-Si) is shown for comparison (dashed black line in bottom panel). The Fermi energy coincides with the solid vertical line at $E = 0$ eV.

Diffusion of Sodium
([3], Sec. III. B)

Perfect stacking fault As a first step for understanding Na diffusion, we computed the mobility of Na inside the fully-filled, half-filled, and empty SF using NEB calculations. In order to remove spurious finite size effects, an extended supercell consisting of eighty atoms was used in these calculations. For the fully-filled SF, it was necessary to remove one Na atom from the supercell in order to create a vacant interstitial site into which the neighboring Na atom can jump. In the half-filled SF, this step was not necessary as the neighboring interstitial sites are already unoccupied. In the empty SF, a single Na atom was added into the open interstitial site within the SF. The atomic positions in both the initial and final NEB configurations were relaxed while the supercell dimensions were kept fixed. As a reference, we performed also an NEB calculation for the Na diffusion between two neighboring tetrahedral interstitial sites in bulk Si using a

cubic supercell containing 64 Si atoms.

The results of the NEB calculations are displayed in Fig. 4.7. All Na diffusion pathways within the SFs are equivalent (see the top panels in Fig. 4.7). The distance between the open interstitial sites in the SFs is double of that between two neighboring tetrahedral interstitial sites in bulk Si (therefore two jumps are plotted in Fig. 4.7). We found that the energy barriers for Na diffusion are 2.0, 2.3, and 0.3 eV in the empty, half-filled, and fully-filled SF, respectively, and about 1.3 eV in bulk Si. The large energy barriers for the empty and half-filled SF can be attributed to the very unfavorable closed interstitial configuration, which the diffusing Na has to pass through. This configuration is slightly metastable for the empty SF, most likely due to missing Na-Na interactions. The transition state in bulk Si corresponds to the hexagonal interstitial site with a significantly lower energy than that of the closed configuration. The migration barrier is therefore correspondingly smaller. By far the smallest migration barrier is observed for the filled SF, in which the Si-Si bonds across the SF are markedly elongated as discussed above. It is this expansion of the SF which contributes mostly to the lowering of the diffusion barrier. It should be noted that for the half-filled SF, the initial and final configurations are not equivalent. Since the final configuration is composed of Na clusters, it is by about 0.1 eV more stable than the initial one (composed of Na rows). The formation of Na clusters leads also to a local elongation of the Si-Si bonds, but this elongation is only about 0.3 Å (compared to 1.96 Å in the fully-filled SF), which is probably not sufficient to influence the diffusion barrier.

Surface model with hydrogen passivation Based on the experimental evidence [30], it is assumed that Na first accumulates in the interface region between Si covered by a thin layer of SiO_x and the SiN_x anti-reflection coating before diffusing into the SFs intersecting the Si surface. We considered first a simplified computational setup using a thin Si slab terminated with two (100) surfaces that contains a (111) stacking fault penetrating the whole slab thickness (see Fig. 4.8). The dangling bonds at the Si surfaces were saturated by hydrogen in order to obtain a stable configuration without any structural and/or electronic artifacts. The atomic positions as well as the dimensions of the supercell perpendicular to the stacking fault were relaxed. Subsequently, the SF was gradually filled with Na atoms and relaxed after each addition. For our supercell model, it was possible to place four Na atoms into the SF so that the final, fully-filled configuration consisted of 40 Si, 17 H and 4 Na atoms.

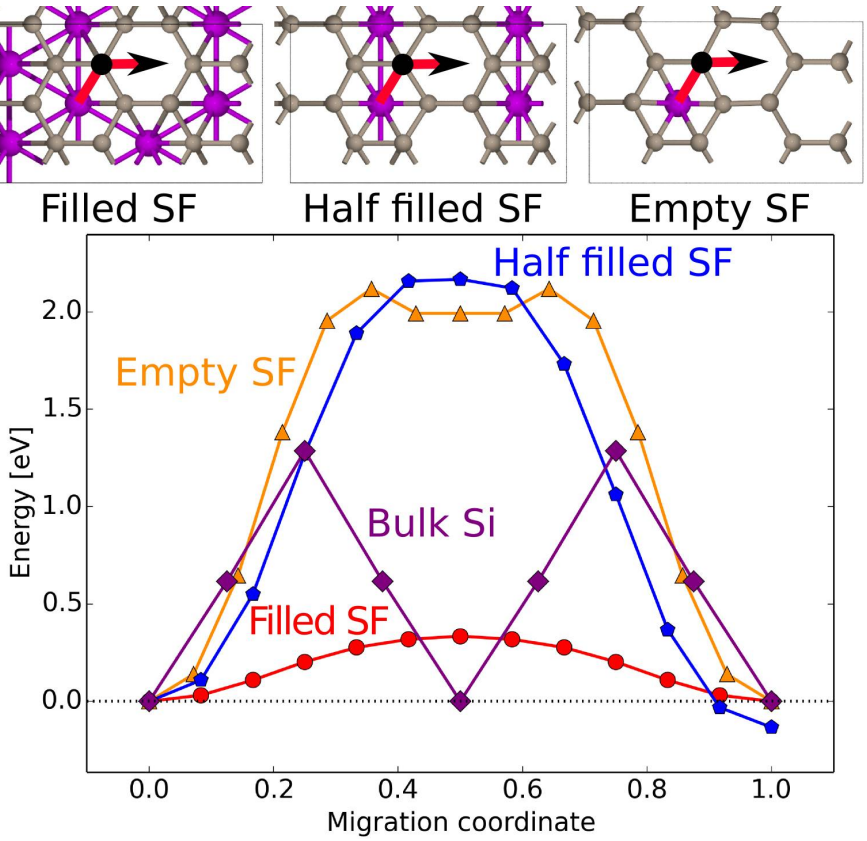

Figure 4.7: Minimum energy paths for Na diffusion along a fully-filled, half-filled, and empty SF as well as for Na diffusion between tetrahedral sites in bulk Si. The diffusion pathways in the crystal are shown schematically in the top panels (the projection is along the [111] direction).

For all four configurations, relative energies were calculated as

$$E(N_{\mathrm{Na}}) = E^{\mathrm{tot}} - N_{\mathrm{Na}}\, \mu_{\mathrm{Na}_{\mathrm{cristobalite}}},$$

where N_{Na} is the number of Na atoms in the system, E^{tot} is the total energy of the supercell, and $\mu_{\mathrm{Na}_{\mathrm{cristobalite}}}$ is the chemical potential of Na in the β-cristobalite. The β-cristobalite was chosen as the representative silicon oxide phase for the oxidized Si surface. We included in the Fig. 4.9 also results from the half-filled and filled SF calculations from the bulk supercells determined as

$$E(N_{\mathrm{Na}}) = N_{\mathrm{Na}} \cdot E_{\mathrm{seg}}$$

with the formation energies corresponding to the chemical potential of the β-cristobalite

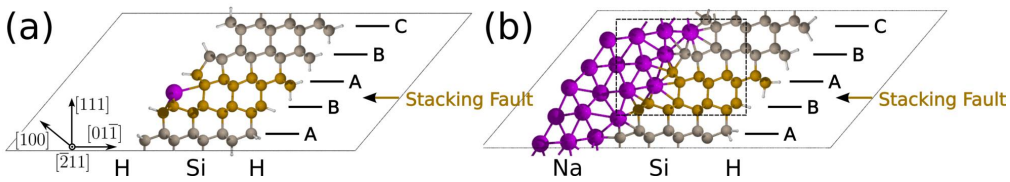

Figure 4.8: Supercells containing a Si slab terminated by (100) surfaces. In model (a), both Si surfaces are passivated by hydrogen (white) atoms. In model (b), the left surface is covered by a thin Na layer (purple atoms). The SF penetrating the slab is marked by orange atoms. The dashed frame shows the segment displayed in Fig. 4.11.

(cf. Eq. 4.1.2 and Fig. 4.4).

Fig. 4.9 shows the relative energy for the four slab configurations (marked as a-d) as a function of Na filling. The energy decreases with increasing number of Na atoms at the SF in a similar way as for the fully-filled SF from the periodic supercell calculation. The small difference between the slab and bulk supercell calculations is likely caused by finite size effects and should become negligible for a thicker slab (the results for the two systems converge as the Na concentration increases). For the choice of the chemical potential, the energy of the half-filled SF increases as it is filled with Na. In addition, we investigated also a configuration where two Na atoms are not immediately neighboring each other but are placed at a larger distance from each other to minimize their mutual interaction. This configuration, marked as (b') in Fig. 4.9, has about 0.74 eV higher energy than the equivalent configuration with neighboring Na atoms, marked as (b). The energy of the (b') configuration nearly agrees with that of the half-filled SF. This result again indicates that the energetics of Na atoms in the SF depends sensitively on the continuity of the Na monolayer.

Apart from the energy analysis, we also investigated the change of the Si-Si bond lengths across the SF upon filling the SF with Na (see Fig. 4.10). For the slab configurations with a continuous Na layer, i.e. (a), (b), (c), and (d), the extension of the bonds at the SF is fully consistent with the gradual Na filling. The Na layer causes the SF to open up and the Si-Si bonds across the SF stretch by 1.7 Å to 2.2 Å. These values are very close to the expansion of 1.96 Å obtained for the fully-filled bulk SF configuration (cf. Sec. 4.1.2). Interestingly, the (b') configuration containing independent Na atoms shows no expansion of the SF, similarly as in the half-filled SF.

The results obtained for the slab model are therefore fully consistent with those obtained

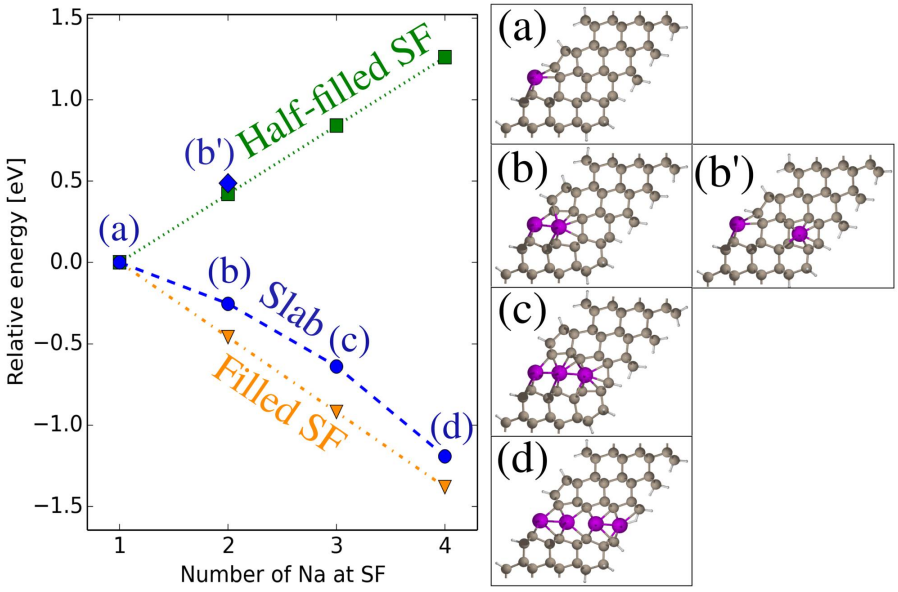

Figure 4.9: The relative energy of Na-decorated SFs as a function of Na concetration for different configurations. The investigated slab configurations are shown on the smaller panels (cf. Fig. 4.8(a)).

for the bulk SF models and the calculated differences due to finite size effects are apparently very small.

Model of Si surface covered with Na In order to mimic the presence of Na on the Si surface, we used the same slab model as described in the previous section, but removed the hydrogen atoms on one side of the slab and covered this surface with 18 randomly placed Na atoms as shown in Fig. 4.8 (b). Upon relaxation (the supercell dimensions were kept fixed), this Na surface layer spontaneously transforms into the equilibrium bcc structure with a (110) plane oriented parallel to the (100) Si surface. Due to a lattice mismatch between the two crystal structures, the Na surface contains a small step at the stacking fault.

To model the process of Na decorating the SF, a series of NEB calculations was carried out as shown in Fig. 4.11. The intermediate NEB configurations were prepared in the following way. First, the Na atom lying closest to the SF (red) was pulled into the stacking fault, thereby creating an empty Na site at the interface. During subsequent structural relaxation, a next Na atom (yellow) from the Na layer filled this space and created a vacancy in the metal. The calculated energy barrier for this process is 1.25 eV, while for the reverse direction only 0.27 eV is needed. In the second step, the red Na

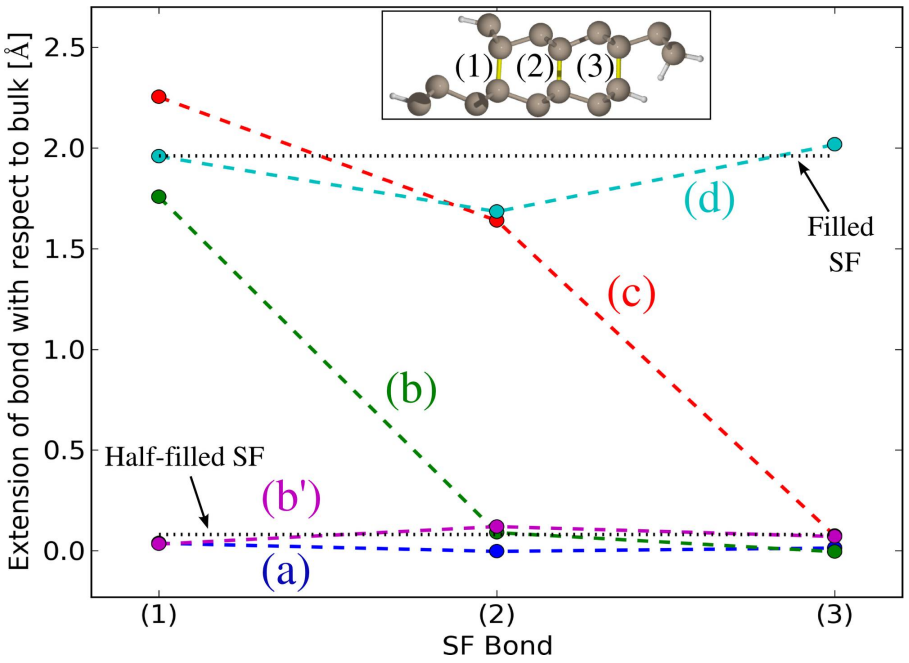

Figure 4.10: Extensions of the Si-Si bond lengths across the SF for different Na-decorated SF configurations. The markings correspond to structures shown in Fig. 4.9.

atom was pulled further into the SF. During relaxation of this configuration no changes of the Na surface layer took place. The corresponding energy barrier amounts to about 1.9 eV. In the third step, the yellow Na atom from the interface layer was pulled into the SF. This jump is again accompanied by a movement of another Na atom (blue) into the emptied site. The energetics for this process is comparable to the first step.

The calculated energy profile in Fig. 4.11 shows that the energy of the subsequent configurations increases, and the process of Na diffusion into the SF is therefore energetically unfavorable. However, it has to be kept in mind that because of the complexity of the NEB calculations, the volume of the system was not allowed to change so that only minimal expansion of the lattice perpendicular to the SF was possible. The presented results therefore effectively correspond to a rather artificial situation of Na diffusion under high compressive stresses.

In order to approach more realistic conditions, we relaxed the intermediate configurations with additional expansion of 1.9 Å perpendicular to the SF, which is the extension observed for the equilibrium SF configuration fully-filled with Na. The energies of these configurations are marked by orange diamonds in Fig. 4.11. The energy of the first configuration increases since there is no Na inside the SF and the whole supercell is under

elastic tension. The energy of the second configuration becomes now almost the same as that of the first configuration since it is favorable for Na to occupy the expanded SF. The third configuration has again a significantly larger energy. The reason for this large increase in energy can be traced back to the situation presented in Fig. 4.9: the energy of an independent Na atom inside the SF is significantly larger than that of a continuous Na layer. Finally, for the fourth configuration containing connected Na atoms the energy again decreases and is comparable to the first two configurations. These results support further our previous analysis that the segregation process will rather involve a continuous Na monolayer than independently diffusing atoms.

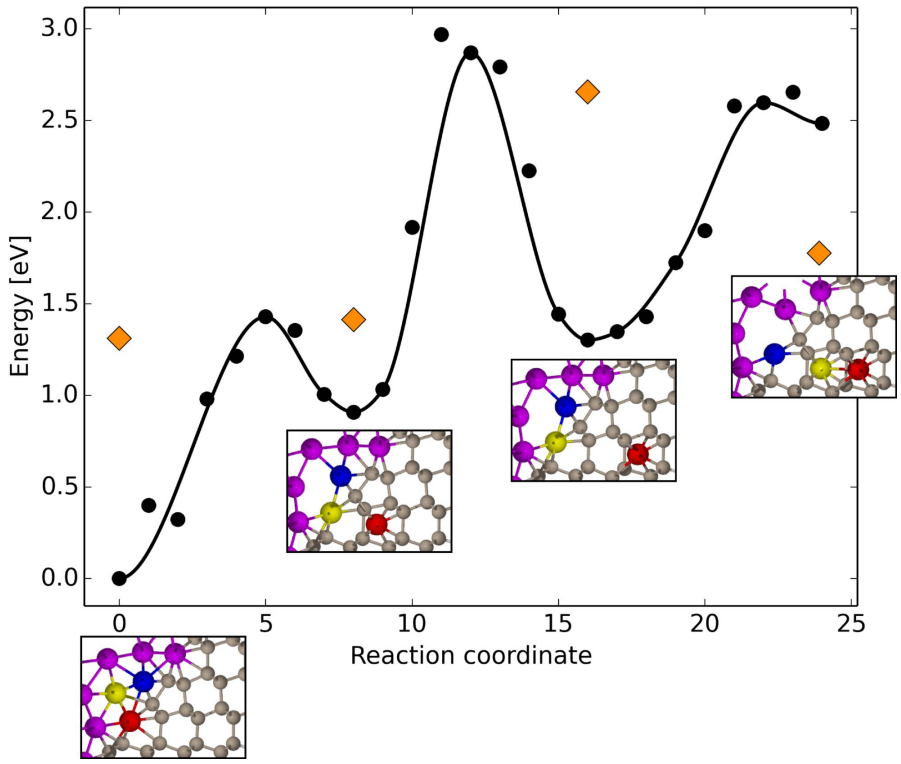

Figure 4.11: The energy profile associated with a three-step process of Na entering the SF computed using the NEB method (black circles and the interpolation curve). The orange squares are obtained by relaxing the intermediate minimum energy configurations using a supercell which is stretched by 2 Å along the [111] direction.

Apart from placing Na atoms in the SF, we also investigated the migration of surface Na atoms into the tetrahedral interstitial site in bulk Si. This configuration turned out to be unstable with the displaced Na atom always moving back to its initial position in the Na layer during relaxation.

4.1.3 Discussion

([3], Sec. IV)

Based on the results of our calculations, we can analyze the behavior of Na atoms in Si stacking faults and provide some explanations of existing experimental observations.

Our computational results confirm the experimental findings that it is energetically favorable for Na to segregate at SFs in Si. The formation energy as well as the local structure of the Na-decorated SF depend sensitively on the amount of segregated Na atoms. The most favorable configuration is a SF fully-filled with Na atoms which form a continuous two-dimensional metallic layer. In order to accommodate such high Na concentration, the interatomic Si-Si bonds across the SF have to extend by about 2 Å compared to their equilibrium distance. This theoretical prediction agrees well with the HRTEM measurements of Naumann *et al.* [30] who observed a widening of the Na-decorated SF by about 2.6 Å.

The large local dilation of the SF is associated with an appearance of two distinct peaks in the density of states that can be attributed to the Si atoms at the SF. The two peaks correspond to localized bonding and anti-bonding states originating predominantly from the stretching of the Si-Si bond across the SF. According to our analysis, the 3s electron of the Na is completely transferred into the Si-Si anti-bonding state at the SF. Since exactly one electron is transferred per anti-bonding state, this state remains half-filled. In addition both, the anti-bonding and bonding states are shifted down in energy by an electrostatic interaction due to the Na ion. Since the half-filled anti-bonding state can contribute to the electronic conduction along the SF, this offers an explanation for the short-circuiting of the p-n junction in the solar cell due to PID.

In order to understand the diffusion of Na atom into and along the Si SFs, we performed extensive NEB calculations. The results in Fig. 4.7 indicate that the Na diffusion barriers in the half-filled and empty SFs (2.3 eV and 2.0 eV, respectively) are significantly higher than the barrier for Na diffusion in bulk Si (1.3 eV), despite a lower Na formation energy in the SF. However, when the SF is fully filled with Na, the diffusion barrier decreases to only 0.3 eV. This large reduction of the barrier height is primarily caused by expansion of the Si-Si bonds across the SF. Further NEB calculations with the slab geometry fully confirm these results.

Additional NEB calculations were carried out to mimic the presence of Na layer on the Si substrate. These simulations are however biased in two aspects. Firstly, the calculations

were done with fixed supercell dimensions so that the system is in equilibrium in the initial configuration but large compressive stresses build up as the Na atoms are placed inside the SF. The potential energy landscape shown in Fig. 4.11 is therefore tilted due to increasing elastic energy in the system, and the energy barriers for filling the SF with Na are overestimated. Secondly, the chemical potential of bcc Na is lower than that of a Na inside the SF making the Na segregation into the SF energetically unfavorable. In order to overcome this limitation, it would be necessary to simulate a more realistic configuration of Si substrate covered by amorphous SiN_x and SiO_x layers. Unfortunately, such configurations are too complex to calculate using DFT.

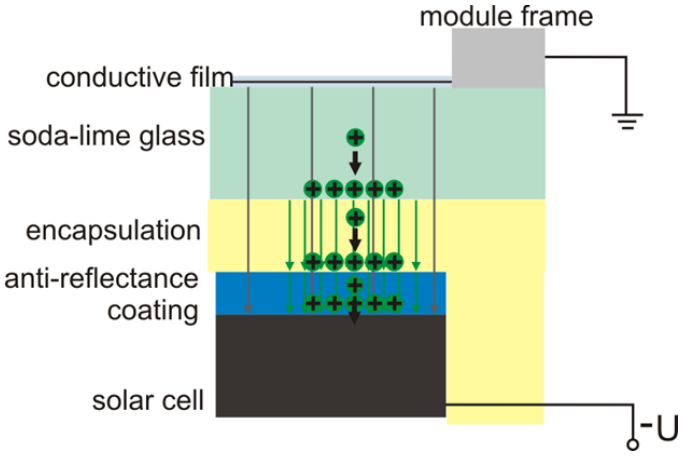

Figure 4.12: Mobile ions including Na diffuse from the glass towards the surface of the silicon solar cell due to a large electric field between the surface of the solar cell and the grounded module frame. Picture taken from [170].

It has been shown that the use of soda-lime glass enhances PID [171]. It is still debated whether the soda-lime glass is the actual source of Na or whether it only enhances the electrical field in the SiN_x anti-reflection coating, which already contains abundant Na impurities [172]. In any case, the mobile Na cations from the overlayers diffuse towards Si due to the external electrical field in the module as shown in Fig. 4.12, and accumulate at the $SiN_x/SiO_x/Si$ interface [30]. The calculated chemical potentials of Na in crystalline SiN_x and SiO_x indicate that Na will tend to leave these phases and most likely also their amorphous variants. As shown in Fig. 4.9, for Na chemical potential corresponding to the β-cristobalite the SF fully filled with Na is the thermodynamically stable configuration while the formation of a half-filled is not favored. Whether this range of chemical potentials exists in real conditions still needs to be determined.

Since our diffusion study is based on the experimental observation that the SFs are filled

from a reservoir of Na atoms segregated at the $SiN_x/SiO_x/Si$ interface, only diffusion of neutral Na atoms was considered in our calculations. It is also posible that Na^+ impurities in bulk Si [173] can diffuse into the SF. However, we believe that this mechanism is of secondary importance since the diffusion barrier for Na in bulk Si is rather large (cf. Fig. 4.7), and no zones of Na depletion around the SFs were observed [56]. In addition, the segregation of Na cations into the SF would be hindered by large repulsive Coulombic interactions which would destabilize any coalescence of charged species.

Finally, a question arises why Na has been found only at SFs but not at the closely related $\Sigma 3$ (111) twin GBs. From the energy arguments there is no reason why this should be the case. It is possible that Na is indeed decorating twin boundaries but they have not been observed yet. Another reason might be crystallographic, since the intrinsic SFs can terminate at flat (100) surfaces of Si (cf. Fig. 4.8) while this is not possible for the $\Sigma 3$ (111) GB. (For a flat surface only one of the bicrystals can have te (100) orientation.) Na segregation at other GBs terminating at (100) Si surfaces has also not been observed which may be related to less favorable diffusion mechanisms than those operating at the SFs.

In conclusion, our results suggest that a large electrical potential is required to transport Na atoms from the Na source (either the soda-lime glass or the SiN_x anti-reflection coating) into the $SiN_x/SiO_x/Si$ interface. Providing Na atoms accumulate at the interface, they would then spontaneously diffuse into the SF, and create an electrically conductive 2D layer. The electrical active SFs cause the short-circuiting of the pn-junction in the solar cell and contribute to the potential induced degradation.

5 Summary

In this thesis, metallic impurities in polycrystalline silicon were studied because they play a major role in the performance of solar cells [21–25, 28–30]. In order to reduce their negative effects, one needs to understand their behavior in the microstructure of silicon polycrystals. Here, we have focused on two important metallic impurities which act very differently, namely iron and sodium. Iron is known to cause the recombination of electrons and holes generated by photons and thus to reduce the efficiency of the solar cell [21–25]. Sodium has been identified recently to be involved in the potential-induced degradation of solar cells [28–30]. For both cases, various atomistic model systems have been studied by first-principles calculations based on density functional theory.

In **Chapter 3**, we have investigated three different aspects of the interaction of interstitial Fe impurities with extended defects and distortions in the microstructure of polycrystalline silicon. In the following, we summarize our main results for the three different scenarios.

Grain boundaries are two-dimensional extended planar defects in polycrystalline silicon. In **Section 3.2**, various atomistic models of high-angle grain boundaries have been constructed and the segregation of Fe atoms at their grain boundary plane has been studied. For the most stable configurations, the electronic structure has been calculated and analyzed. We found that the segregation of interstitial iron depends strongly on the orientation of the grain boundary plane rather than only on the Σ-value characterizing the misorientation of the grains. For example, segregation of interstitial Fe is observed at the Σ 3 (112) and Σ 3 (110) grain boundaries but not at Σ 3 (111) grain boundaries. Our results emphasize the necessity to describe the segregation behavior of Fe to a specific grain boundary not only by its Σ-value value but also by the inclination of the grain boundary plane [36, 39, 94, 96].

Mechanical strain fields can be caused by various extended defects such as triple junctions of grain boundaries, dislocations, or precipitates, and they may influence the

formation energy of Fe impurities. This can result in the agglomeration of Fe impurities in spatial regions of sufficiently large strain [41, 43, 44, 52]. To see how interstitial Fe is affected by mechanical strain, we have applied various modes of mechanical strain to a supercell of the bulk Si crystal containing an Fe impurity in **Section 3.3**. Three different defect configurations under the influence of strain have been considered. While the interstitial Fe at hexagonal sites and substitutional Fe are affected by hydrostatic, uniaxial and shear strain, the most stable configuration, an Fe interstitial at a tetrahedral site, is not affected by strain. This implies that there is no thermodynamic driving force for Fe impurities to segregate in regions of high strain. Nevertheless, mechanical strain influences the diffusion of Fe impurities. The diffusivity of interstitial Fe which has been obtained from kinetic Monte Carlo simulations is strongly lowered by compressive strain while dilative stain increases the diffusivity.

Dislocations are one-dimensionally extended linear defects which consist of a short-ranged atomistic core region surrounded by a long-ranged elastic strain field [105]. In **Section 3.4**, the two different regions have been both studied.

In a first step, the results of **Section 3.3** for strained bulk crystals were extrapolated to describe the influence of the dislocation far away from the core region on the migration of an Fe atom by considering only its elastic strain field. The two types of perfect dislocations in silicon, namely the screw and 60° mixed dislocation, behave quite differently. While the screw dislocation always enhances the diffusion of Fe impurities in its vicinity, the 60° mixed dislocation can both enhance and impede the Fe diffusion in the tensile region and the compressive region around the dislocation core, respectively. Under normal conditions, these two types of perfect dislocations are split into partial dislocations. For a 60° mixed dislocation split into a 90° and a 30° partial dislocation we found no qualitatively different behavior. However, when a perfect screw dislocation is split into two 30° partial dislocations, its behavior changes because the influence of the 30° partial dislocation on the iron migration is more like that of the perfect 60° mixed dislocation, it is just weaker.

In a second step, atomistic core models of partial 30° and 90° dislocations have been constructed and the segregation of interstitial Fe to those has been studied. For all considered atomistic core models, segregation of interstitial Fe is favored. In the electronic structure of the dislocation the segregated Fe induces an additional

gap state from the Fe d-states. This additional gap state may explain observations from deep level transient spectroscopy measurements on dislocations which were decorated by metallic impurities [52, 83, 157, 159, 160].

The combined results of the two different regimes indicate how segregation of interstitial Fe at dislocation cores happens: the tensile region of the long-ranged elastic strain field enhances the diffusion around dislocations by which Fe atoms can be transported preferably to regions of higher dislocation densities where they finally segregate at cores of the partial 30° and 90° dislocation. Once interstitial Fe is segregated, the dislocation becomes electrically active and thus alters the performance of the device.

In **Chapter 4**, we have investigated one aspect of sodium in silicon in the context of potential-induced degradation. In the following, we summarize our main results on the sodium-decorated stacking faults in crystalline bulk silicon.

Sodium-decorated stacking faults have been recently identified as the key reason for potential-induced degradation, but until now only speculations on the physical mechanism exist [28–30, 56]. In literature it is proposed that sodium drifts from the protection glass of the solar module to the silicon surface of the solar cell because of an electric potential difference that is build up between the grounded frame of the solar module and the surface silicon of the chip. The sodium which is enriched at the silicon surface diffuses into stacking faults reaching to the surface and covers these completely. In this chapter the structural, thermodynamic and electronic properties of these planar defects have been investigated. Our results reveal that the presence of sodium atoms leads to a substantial elongation of the silicon-silicon bonds across the stacking fault. This elongation gives rise to partially occupied defect levels within the silicon band gap that lead to electrical conduction along the stacking fault. Our thermodynamic analysis of the sodium-decorated stacking faults takes all relevant chemical environments of the system into account, namely the anti-reflection coating (SiN_x), the silicon surface, the native oxide film (SiO_x) which forms at the silicon surface during the production of the solar cell, and stacking faults which form during the growth of the silicon wafer. The analysis of the formation energy of the sodium-decorated stacking fault reveals that sodium prefers to stay in the silica at the silicon surface and enters the silicon only if a stacking fault is present. This interpretation is in agreement with experimental observations. Furthermore, the degree of planar coverage of the

stacking fault and continuously connectivity of the sodium layer strongly affects the diffusion behavior of sodium within the stacking fault such that configurations are favored in which the sodium monolayer is not disconnected.

6 Outlook

The work on the behavior of iron impurities in the microstructure of polycrystalline Si in Chapter 3 can be extended in several ways. In the following we discuss some suggestions of how this study can be continued to answer questions which require large system sizes, or questions that concerns defect complexes of iron, charge states of iron, and other elements.

Larger systems: So far only rather symmetric high-angle grain boundaries with low Σ-value and short planar periodicity have been studied since such grain boundary segments are most abundant in silicon. However, also other classes of grain boundaries in particular more asymmetric and small-angle grain boundaries are important for photovoltaic applications [95]. Unfortunately, these kind of grain boundaries usually require large supercells of several hundreds to thousands of atoms.

In order to describe dislocations by first-principles calculations, these were always represented as a perfect one-dimensional line defect. In reality kinks, jogs and other intrinsic structural defects occur along dislocation lines [105]. Again, such kinds of defects cannot be studied with first-principles calculations due to the required too large sizes of the supercells.

These two example indicate the size limitation of first-principles calculations and the need for simplified atomic interaction models for the binary Si-Fe system which can treat problems such as interstitial iron atoms at small-angle grain boundaries or at intrinsic imperfections of dislocation cores. Such simplified models for the Si-Fe system still do not exit but one promising way of development for such a model may be a tight-binding total-energy model in which the quantum-mechanical description of the chemical bonds is still included but the Hamiltonian of the system is systematically simplified [174]. Within such an approach several thousand atoms can be described which will allow to study the thermodynamics

and kinetics of Fe impurities at small-angle grain boundaries, and non-straight dislocations.

Defect complexes: Another important aspect of interstitial iron in silicon is its property to interact with shallow dopants and hydrogen impurities that are present in the silicon matrix [21, 83]. This interaction leads to the formation of defect complexes such as FeB or FeH pairs in silicon. For simplification these interactions were not taken into account throughout this thesis. But they have to be considered for a more realistic description. While it is known that the bulk electronic structure of these defect complexes is different, it is still unclear if the segregation behavior of iron at extended planar or linear defects is also affected by the formation of such complexes. In the case of dislocations, it was already shown that hydrogen segregates at the dislocation cores [114, 115]. Since in this thesis the same was shown for interstitial iron, it will be very likely that iron and hydrogen do interact at the cores of dislocations. Further studies will be necessary to investigate this interaction not only at the dislocation cores but also at the grain boundaries.

Charge states of iron: Throughout this thesis only neutral interstitial iron in silicon was considered. In p-type silicon, also positively charged Fe^{+} is observed [21, 83]. The investigation of Fe^{+} requires calculations for charged supercells. Since first-principles calculations of solids are usually carried out using periodic boundary conditions, for calculations of charged defects it is necessary to introduce a compensating homogenous background charge density to ensure that that the total energy remains finite. Moreover, the charged defect in a supercell interacts electrostatically with its mirror images and thus one has to correct for this long-range interaction by either increasing the size of the supercell drastically or by applying more sophisticated correction schemata [175]. Thus, the extension of the current work to charged iron defects in silicon will require a careful electrostatic treatment of each supercell but will lead to more insight into the behavior of iron impurities in silicon materials.

Other impurity elements: The first part of our study has been focused on interstitial iron only. Other transition metals are important as well for the performance of solar cells. In particular, interstitial chromium has been identified as a very important metallic impurity for solar cells with n-based emitters [176]. To carry out a corresponding study for interstitial chromium is a straightforward extension of this work since the same atomistic simulation models and analysis procedures can be

employed.

In the **Chapter 2.** of this work, sodium-decorated stacking faults and their role in the potential-induced degradation have been studied and can be extended in several ways:

Stacking faults decorated by other elements: So far only sodium-decorated stacking faults have been investigated because the study was motivated by their direct experimental observation by high resolution transmission electron microscopy [56]. However, also other alkali metals such as potassium or even alkaline earth metals such as magnesium may decorate stacking faults in silicon if the elements enter the SF from appropriate reservoirs. The study of these elements at stacking faults can be carried out by adopting the same steps as for the sodium-decorated stacking faults. Moreover, thermodynamic calculations of formation energies may guide experimentalists in avoiding (or enhancing) stacking faults by other malign (or benign) elements.

The process of decoration: Also the dynamics of the decoration process of the stacking fault is not yet completely clarified. While our work provides first insight on how this process takes place, more investigations are needed. For instance, so far no electric field along the stacking fault has been considered. It may be that such an electric field is required to drive the kinetics of the decoration process. The incorporation of an electric field into a first-principles calculation is possible at least for atomic slab models [177].

Sodium as a cause for stacking faults in silicon: Another open question is whether the stacking faults exist before the sodium decorates these or they can also be created or further extended by the sodium. It may be that the sodium reservoir which forms at the silicon surface leads to large mechanical stresses which are released by the formation of stacking faults that are then decorated by sodium, or that the decoration process leads to the extension of the stacking fault by further propagating the partial dislocation that terminates the stacking fault, from the surface into the interior of the crystal. Such a process cannot be studied using first-principles simulations. Simpler models such as tight-binding total-energy models which can handle much larger systems are needed as already discussed for the case of the Fe-Si system.

Appendix

Computational setup

In Chapter 3, all the reported DFT calculations have been carried out by means of the Quantum Espresso PWscf code [178] which uses a plane-wave basis to represent the wavefunctions of the valence electrons. Interactions of ionic cores and valence electrons are described by ultrasoft pseudopotentials. The PBE generalized gradient approximation was used for exchange-correlation [65, 179]. For all calculations in which Fe was involved spin-polarization was taken into account. Energy cutoffs of $48\,\mathrm{eV}$ and $480\,\mathrm{eV}$ for the plane-wave basis and the Fourier representation of the electron density, respectively, were found to yield sufficiently converged results. The Brillouin-zone integrals were sampled by Monkhorst-Pack k-point grids [76]. The specific grids differ for the various supercells but the results were checked for equally good convergence in all cases. Positions of the atoms were relaxed until the residual forces acting on the atoms were less than 10^{-4} eV/Å. The volume was relaxed for each GB supercell of Si without Fe and then kept fixed when Fe was inserted at interstitial sites.

The minimum energy paths (MEPs) for jumps of Fe atoms between neighboring sites were calculated using the nudged elastic band (NEB) method [74]. In addition, the climbing image NEB (CI-NEB) method was applied to ensure accurate locations of activation barriers [74]. The threshold for the total forces, which are acting on the NEB images of an interpolated reaction path, was set to 0.05 eV/Å.

In Chapter 4, all DFT calculations have been performed using the Siesta [180], which uses a local orbital basis to expand the wave-functions of the valence electrons. In order to obtain converged results, polarized double-zeta basis sets of numerical orbitals were employed for all elements [180]. Interactions between ionic

cores and valence electrons were described using norm-conserving pseudopotentials in Troullier-Martins form [181]. For exchange-correlation the PBE generalized gradient approximation was used [65]. The charge density was projected on a real-space grid; an equivalent plane-wave-energy cutoff of 270 eV for the fast Fourier transformation has been found to yield well converged total energies. For Brillioun-zone integration, grids of $8 \times 4 \times 8$ k-points were used for the SF-model and $1 \times 2 \times 12$ k-points were used for the surface-slab model. Geometry optimization was carried out using the BFGS algorithm [154] until forces acting on the ions were less than 0.01 eV/ Å. Energy barriers associated with atomic migration process were calculated using the nudged elastic band method (NEB) [74, 75]. The force convergence criterion in the NEB calculations was set to be less than 0.05 eV/Å.

Management of calculations Throughout the thesis, DFT calculations have been set up, analyzed and managed with the help of the atomic simulation environment [182].

Deformation matrices for the calculation of formation energy under strain

In the following, we list the deformation matrices D which are used according to Eq. 3.3.2 to apply an elastic strain to the cubic 64 atom supercell of the diamond structure of Si. For hydrostatic strain $\varepsilon_{Hyd}(\varepsilon)$, the deformation matrix is

$$\begin{pmatrix} \varepsilon & 0 & 0 \\ 0 & \varepsilon & 0 \\ 0 & 0 & \varepsilon \end{pmatrix}. \tag{6.0.1}$$

For uniaxial strains $\varepsilon_{[100]}$, $\varepsilon_{[110]}$, $\varepsilon_{[111]}$, $\varepsilon_{[112]}$, the deformation matrices are

$$\begin{pmatrix} \varepsilon & 0 & 0 \\ 0 & 0 & 0 \\ 0 & 0 & 0 \end{pmatrix}, \begin{pmatrix} \frac{\varepsilon}{2} & -\frac{\varepsilon}{2} & 0 \\ -\frac{\varepsilon}{2} & \frac{\varepsilon}{2} & 0 \\ 0 & 0 & 0 \end{pmatrix},$$

$$\begin{pmatrix} \frac{\varepsilon}{3} & \frac{\varepsilon}{3} & \frac{\varepsilon}{3} \\ \frac{\varepsilon}{3} & \frac{\varepsilon}{3} & \frac{\varepsilon}{3} \\ \frac{\varepsilon}{3} & \frac{\varepsilon}{3} & \frac{\varepsilon}{3} \end{pmatrix}, \begin{pmatrix} \frac{\varepsilon}{6} & \frac{\varepsilon}{6} & -\frac{\varepsilon}{3} \\ \frac{\varepsilon}{6} & \frac{\varepsilon}{6} & -\frac{\varepsilon}{3} \\ -\frac{\varepsilon}{3} & -\frac{\varepsilon}{3} & \frac{\varepsilon}{6} \end{pmatrix},$$

respectively. For the shear strains, $\tau_{[010],[001]}$, $\tau_{[11\bar{2}],[111]}$, $\tau_{[\bar{1}10],[11\bar{2}]}$, $\tau_{[111],[\bar{1}10]}$, the deformation matrices are

$$\begin{pmatrix} 0 & \varepsilon & 0 \\ \varepsilon & 0 & 0 \\ 0 & 0 & 0 \end{pmatrix}, \begin{pmatrix} \sqrt{2}\frac{\varepsilon}{3} & \sqrt{2}\frac{\varepsilon}{3} & -\sqrt{2}\frac{\varepsilon}{6} \\ \sqrt{2}\frac{\varepsilon}{3} & \sqrt{2}\frac{\varepsilon}{3} & -\sqrt{2}\frac{\varepsilon}{6} \\ -\sqrt{2}\frac{\varepsilon}{6} & -\sqrt{2}\frac{\varepsilon}{6} & -2\sqrt{2}\frac{\varepsilon}{3} \end{pmatrix}$$

$$\begin{pmatrix} -\sqrt{3}\frac{\varepsilon}{3} & 0 & \sqrt{3}\frac{\varepsilon}{3} \\ 0 & \sqrt{3}\frac{\varepsilon}{3} & -\sqrt{3}\frac{\varepsilon}{3} \\ \sqrt{3}\frac{\varepsilon}{3} & -\sqrt{3}\frac{\varepsilon}{3} & 0 \end{pmatrix}, \begin{pmatrix} -\sqrt{6}\frac{\varepsilon}{3} & 0 & -\sqrt{6}\frac{\varepsilon}{6} \\ 0 & \sqrt{6}\frac{\varepsilon}{3} & \sqrt{6}\frac{\varepsilon}{6} \\ -\sqrt{6}\frac{\varepsilon}{6} & \sqrt{6}\frac{\varepsilon}{6} & 0 \end{pmatrix},$$

respectively.

Description of the kMC simulation code

In Chapter 3.3 diffusion constants of interstitial Fe impurities in strained Si crystals have been calculated using a lattice kMC approach. As a part of the thesis work, a code was written to carry out these kMC calculations. In the following the structure of this code is described.

The general algorithm was already discussed in Sec. 2.2.2. The usage of large simulation boxes such as the one used in Sec. 3.3 requires a software code which is feasible to run such simulations in a reasonable amount of time. In order to achieve an easy handling of the code by other users and a good readability of the source code, the program was written using the scripting language Python (see, e.g. Ref. [183]). Time critical parts of the code were translated into Cython (see, e.g. Ref. [184]).

The main structure of the code can be divided in three different classes: the *kMC* class, the *atomlist* class and the *lattice* class as depicted in Fig. 6.1.

The *lattice* class stores all information of the lattice such as positions of the sites, occupation of the sites and connections between sites. A lattice can be defined in two or three

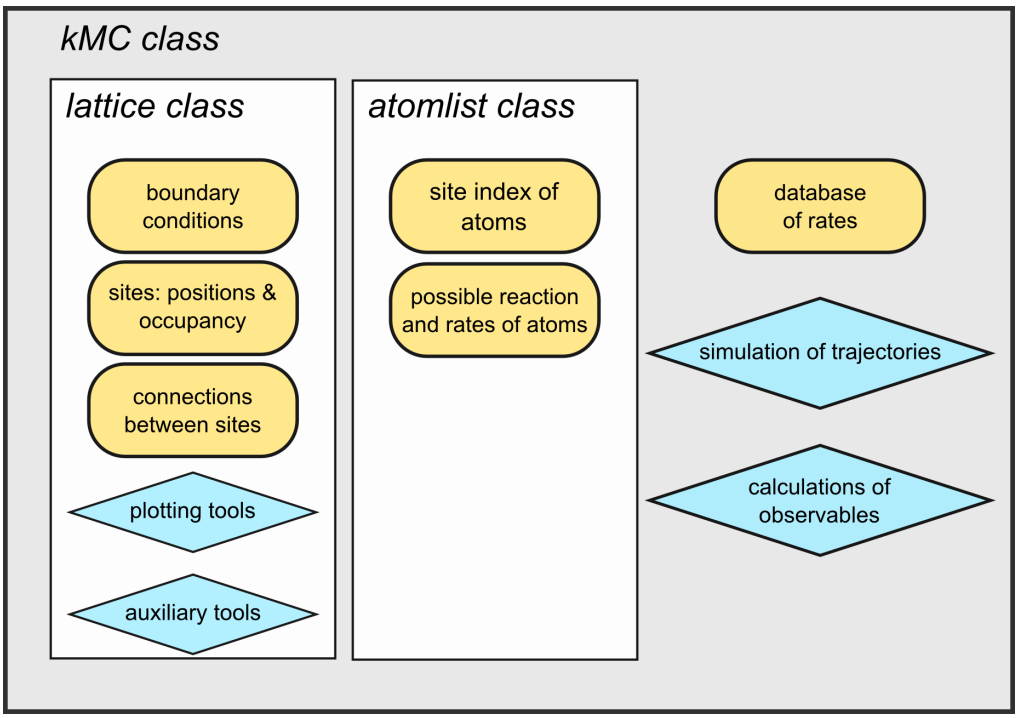

Figure 6.1: Structure of the kMC simulation code.

dimensions with open or periodic boundary conditions. In addition, helper functions are included to plot the lattice, to build up connections between sites by a nearest-neighbor analysis, and more.

The *atomlist* class tracks all information of the particles which migrate/diffuse through a lattice. It contains all data which define the current configuration of the system. Optionally, the atomlist also saves the current positions of the particles on a given *lattice* object. Moreover, possible reaction events and the corresponding reaction rates are stored in this object.

The *kMC* class carries out the actual simulation. It requires an *atomlist* and a *lattice* object. The *kMC* class incorporates all methods for the actual kMC simulation, i.e. carrying out a single kMC step, calculating kMC trajectories and obtaining observables such as diffusion constants. It also saves the information of the rates for possible reactions. There are two different ways how to set up the reaction rates for the simulations: the first way is the definition of a function called *ratefunction* which describes the rates as a function of the current position of the diffusing particle and the direction of the jump process. Since its definition can be sometimes rather tedious, the second possibility is to label each site of a lattice and define a table of rates for the diffusion between different types of sites,

i.e. the diffusion from a site of type X to a site of type Y, $X \to Y$, requires the input of the rate $\Gamma_{X \to Y}$.

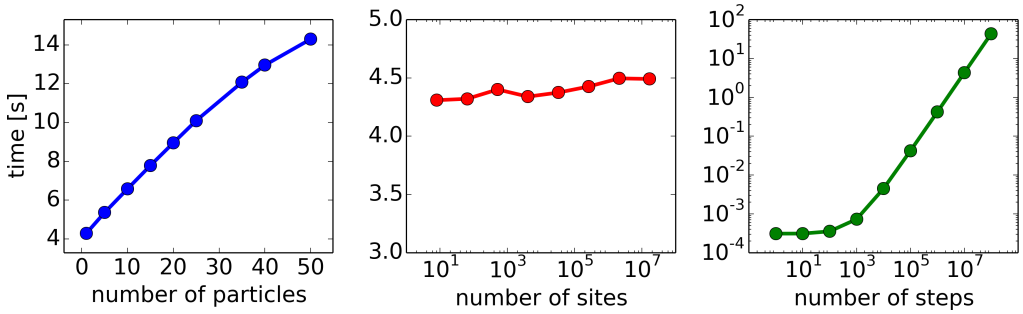

Figure 6.2: Benchmark of the kMC simulation. The computational time is shown for different number of particles, different number of lattice sites and different number of kMC steps.

The calculation of observables in a kMC simulation requires a large amount of long kMC trajectories and hence an efficient performance of a kMC step is crucial. Fig. 6.2 shows a benchmark of a diffusion through a crystal with the diamond structure. Each value is obtained from an average of ten independent calculations.

The graph on the left in Fig. 6.2 shows the computation times which are required to perform 10 million kMC steps for different numbers of particles. The graph shows an almost linear behavior. It turns out that the time limiting step is the calculation of the cumulative sum which increases linearly with the number of possible events, i.e. the number of rates of possible reactions in the kMC simulation. The number of events is proportional to the number of diffusing particles in the dilute limit because every particle has the same number of possible events in our test case. For large particle numbers, some of the particles block each others and less reactions are possible. This leads to the slight bending of the blue curve in Fig. 6.2.

The middle graph in Fig. 6.2 shows the computation times for different numbers of lattice sites. Apparently the computational time for 10 million kMC steps does not depend on the number of lattice sites in the system.

The graph on the right Fig. 6.2 reveals that after about 100 kMC steps the computation time grows linearly with the number of steps . For fewer steps, the required time is mostly influenced by the overhead of function calls and allocation of memory which lead to an almost constant time value.

The present code can be easily adapted for the use in other problems of materials science. In particular, the high performance efficiency of the code allows to treat large system sizes. This benchmark shows that the code performance is independent from the number of lattices sites even up to 10^7 and its linear scaling with the number of particles is nearly perfect. The kinetic Monte-Carlo approach is one of the most promising ways to carry atomistic insight over to macroscopic behavior of materials. In the future, this code can be used for instance to study the precipitation of second phases, to obtain effective diffusion constant for grain boundaries and dislocations, and much more.

Bibliography

[1] B. Ziebarth, M. Mrovec, C. Elsässer, and P. Gumbsch. *Influence of dislocation strain fields on the diffusion of interstitial iron impurities in silicon*. Phys. Rev. B **92** (11), 2015, 115309.

[2] B. Ziebarth, M. Mrovec, C. Elsässer, and P. Gumbsch. *Interstitial iron impurities at grain boundaries in silicon: A first-principles study*. Phys. Rev. B **91** (3), 2015, 35309.

[3] B. Ziebarth, M. Mrovec, C. Elsässer, and P. Gumbsch. *Potential-induced degradation in solar cells: Electronic structure and diffusion mechanism of sodium in stacking faults of silicon*. J. Appl. Phys. **116** (9), 093510, 2014.

[4] B. Lang, B. Ziebarth, and C. Elsässer. *Lithium Ion Conduction in $LiTi_2(PO_4)_3$ and Related Compounds Based on the NASICON Structure: A First-Principles Study*. Chem. Mater. **27** (14), 2015, 5040–5048.

[5] B. Ziebarth, M. Klinsmann, T. Eckl, and C. Elsässer. *Lithium diffusion in the spinel phase $Li_4Ti_5O_12$ and in the rocksalt phase $Li_7Ti_5O_12$ of lithium titanate from first principles*. Phys. Rev. B **89**, 17 2014, 174301.

[6] J. N. Mayer, D. S. Philipps, N. S. Hussein, D. T. Schlegl, and C. Senkpiel. *Current and Future Cost of Photovoltaics - Long-term scenarios for Market Development, System Prices and LCOE of Utility-Scale PV Systems*. 2015.

[7] R. M. Swanson. *A vision for crystalline silicon photovoltaics*. Prog. Photovoltaics Res. Appl. **14** (5), 2006, 443–453.

[8] G. F. Nemet and D. Husmann. *PV learning curves and cost dynamics*. Advances in Photovoltaics Part I: Basics **1**, 2012, 85.

[9] A. Sharma. *Top Solar Power Industry Trends for 2015*. 2015.

[10] JA Solar Holdings Co., Ltd. *JA Solar and Essel Infraprojects Limited Sign MOU on 500MW PV Joint Venture*. URL: `http://www.prnewswire.com/news-releases/ja-solar-and-essel-infraprojects-limited-sign-mou-on-500mw-pv-joint-venture-300088239.html` (visited on 08/11/2015).

[11] H. Wirth and K. Schneider. *Aktuelle Fakten zur Photovoltaik in Deutschland*. 2012.

[12] D. Wöhrle and D. Meissner. *Organic solar cells*. Adv. Mater. **3** (3), 1991, 129–138.

[13] F. C. Krebs. *Fabrication and processing of polymer solar cells: a review of printing and coating techniques*. Sol. Energy Mater. Sol. Cells **93** (4), 2009, 394–412.

[14] S. Günes, H. Neugebauer, and N. S. Sariciftci. *Conjugated polymer-based organic solar cells*. Chem. Rev. **107** (4), 2007, 1324–1338.

[15] Y.-J. Cheng, S.-H. Yang, and C.-S. Hsu. *Synthesis of conjugated polymers for organic solar cell applications*. Chem. Rev. **109** (11), 2009, 5868–5923.

[16] A. Kojima, K. Teshima, Y. Shirai, and T. Miyasaka. *Organometal halide perovskites as visible-light sensitizers for photovoltaic cells*. J. Am. Chem. Soc. **131** (17), 2009, 6050–6051.

[17] H.-S. Kim, C.-R. Lee, J.-H. Im, K.-B. Lee, T. Moehl, A. Marchioro, S.-J. Moon, R. Humphry-Baker, J.-H. Yum, J. E. Moser, et al. *Lead iodide perovskite sensitized all-solid-state submicron thin film mesoscopic solar cell with efficiency exceeding 9%*. Sci. Rep. **2**, 2012.

[18] G. Hodes. *Perovskite-based solar cells*. Science **342** (6156), 2013, 317–318.

[19] M. Tao. "Status of Solar Photovoltaics". In: *Terawatt Solar Photovoltaics*. Springer, 2014, 9–20.

[20] S. Pizzini, M. Acciarri, and S. Binetti. *From electronic grade to solar grade silicon: chances and challenges in photovoltaics*. Phys. Status Solidi A **202** (15), 2005, 2928–2942.

[21] A. Istratov, H. Hieslmair, and E. Weber. *Iron and its complexes in silicon*. Appl. Phys. A **69** (1), 1999, 13–44.

[22] A. Istratov, H. Hieslmair, and E. Weber. *Iron contamination in silicon technology*. Appl. Phys. A **70** (5), 2000, 489–534.

[23] G. Coletti, P. C. Bronsveld, G. Hahn, W. Warta, D. Macdonald, B. Ceccaroli, K. Wambach, N. Le Quang, and J. M. Fernandez. *Impact of metal contamination in silicon solar cells*. Adv. Funct. Mater. **21** (5), 2011, 879–890.

[24] T. Buonassisi, A. A. Istratov, M. D. Pickett, M. Heuer, J. P. Kalejs, G. Hahn, M. A. Marcus, B. Lai, Z. Cai, S. M. Heald, T. F. Ciszek, R. F. Clark, D. W. Cunningham, A. M. Gabor, R. Jonczyk, S. Narayanan, E. Sauar, and E. R. Weber. *Chemical natures and distributions of metal impurities in multicrystalline silicon materials*. Prog. Photovolt. Res. Appl. **14** (6), 2006, 513–531.

[25] D. Macdonald and L. Geerligs. *Recombination activity of interstitial iron and other transition metal point defects in p-and n-type crystalline silicon*. Appl. Phys. Lett. **85** (18), 2004, 4061–4063.

[26] A. Hähnel, J. Bauer, H. Blumtritt, O. Breitenstein, D. Lausch, and W. Kwapil. *Electron microscope verification of prebreakdown-inducing α-$FeSi_2$ needles in multicrystalline silicon solar cells*. J. Appl. Phys. **113** (4), 2013, 44505.

[27] A. Istratov, T. Buonassisi, M. Pickett, M. Heuer, and E. Weber. *Control of metal impurities in "dirty" multicrystalline silicon for solar cells*. Mater. Sci. Eng., B **134** (2), 2006, 282–286.

[28] P. Hacke, M. Kempe, K. Terwilliger, S. Glick, N. Call, S. Johnston, S. Kurtz, I. Bennett, and M. Kloos. *Characterization of Multicrystalline Silicon Modules with System Bias Voltage Applied in Damp Heat*, 2010, 3760 –3765.

[29] S. Pingel, O. Frank, M. Winkler, S. Daryan, T. Geipel, H. Hoehne, and J. Berghold. "Potential Induced Degradation of solar cells and panels". In: *Photovoltaic Specialists Conference (PVSC), 35th IEEE*. 2010, 2817–2822.

[30] V. Naumann, D. Lausch, A. Hähnel, J. Bauer, O. Breitenstein, A. Graff, M. Werner, S. Swatek, S. Großer, J. Bagdahn, and C. Hagendorf. *Explanation of potential-induced degradation of the shunting type by Na decoration of stacking faults in Si solar cells*. Sol. Energy Mater. Sol. Cells **120**, 2014, 383–389.

[31] A. Liu, D. Walter, S. P. Phang, and D. Macdonald. *Investigating internal gettering of iron at grain boundaries in multicrystalline silicon via photoluminescence imaging*. IEEE J. Photovolt. **2** (4), 2012, 479–484.

[32] A. Liu, D. Walter, S. P. Phang, and D. Macdonald. "Imaging and modelling the internal gettering of interstitial iron by grain boundaries in multicrystalline silicon". In: *Photovoltaic Specialists Conference (PVSC), 38th IEEE*. IEEE. 2012, 248–253.

[33] D. Macdonald, A. Y. Liu, and S. P. Phang. *External and Internal Gettering of Interstitial Iron in Silicon for Solar Cells*. Solid State Phenom. **205**, 2014, 26–33.

[34] J. Hofstetter, D. P. Fenning, D. M. Powell, A. E. Morishige, and T. Buonassisi. *Iron Management in Multicrystalline Silicon through Predictive Simulation: Point Defects, Precipitates, and Structural Defect Interactions*. Solid State Phenom. **205**, 2014, 15–25.

[35] M. Seibt and V. Kveder. *Gettering Processes and the Role of Extended Defects*. Advanced Silicon Materials for Photovoltaic Applications, 2012, 127–188.

[36] J. Chen, B. Chen, W. Lee, M. Fukuzawa, M. Yamada, and T. Sekiguchi. *Grain Boundaries in Multicrystalline Si*. Solid State Phenom. **156-158**, 2009, 19–26.

[37] D. Macdonald, J. Tan, and T. Trupke. *Imaging interstitial iron concentrations in boron-doped crystalline silicon using photoluminescence*. J. Appl. Phys. **103** (7), 2008, 73710.

[38] A. Liu, Y.-C. Fan, and D. Macdonald. *Interstitial iron concentrations across multicrystalline silicon wafers via photoluminescence imaging*. Prog. Photovolt. Res. Appl. **19** (6), 2011, 649–657.

[39] J. Chen, T. Sekiguchi, D. Yang, F. Yin, K. Kido, and S. Tsurekawa. *Electron-beam-induced current study of grain boundaries in multicrystalline silicon*. J. Appl. Phys. **96** (10), 2004, 5490–5495.

[40] M. Knörlein, A. Autruffe, R. Søndenå, and M. Di Sabatino. *Internal Gettering of Iron at Extended Defects*. Energy Procedia **55**, 2014, 539–544.

[41] V. Ganapati, S. Schoenfelder, S. Castellanos, S. Oener, R. Koepge, A. Sampson, M. A. Marcus, B. Lai, H. Morhenn, G. Hahn, J. Bagdahn, and T. Buonassisi. *Infrared birefringence imaging of residual stress and bulk defects in multicrystalline silicon*. J. Appl. Phys. **108** (6), 2010, 63528.

[42] G. Sarau, S. Christiansen, M. Holla, and W. Seifert. *Correlating internal stresses, electrical activity and defect structure on the micrometer scale in EFG silicon ribbons*. Sol. Energy Mater. Sol. Cells **95** (8), 2011, 2264–2271.

[43] A. Augusto, D. Pera, H. J. Choi, P. Bellanger, M. C. Brito, J. M. Alves, A. M. Vallêra, T. Buonassisi, and J. M. Serra. *Residual stress and dislocations density in silicon ribbons grown via optical zone melting*. J. Appl. Phys. **113** (8), 2013, 83510.

[44] M. Nacke, M. Allardt, P. Chekhonin, E. Hieckmann, W. Skrotzki, and J. Weber. *Investigations on residual strains and the cathodoluminescence and electron beam induced current signal of grain boundaries in silicon*. J. Appl. Phys. **115** (16), 2014, 163511.

[45] K. Suzuki, Y. Yoshida, T. Kamimura, M. Ichino, and K. Asahi. *Iron diffusion in silicon under external stress*. Physica B **404** (23 – 24), 2009, 4678 –4680.

[46] K. Suzuki, Y. Yoshida, K. Hayakawa, K. Yukihira, M. Ichino, and K. Asahi. *Observation of iron impurity diffusion in silicon under bending stress by Mössbauer spectroscopy*. Hyperfine Interact. **197** (1 – 3), 2010, 213–217.

[47] M. Seibt, V. Kveder, W. Schröter, and O. Voß. *Structural and electrical properties of metal impurities at dislocations in silicon*. Phys. Status Solidi A **202** (5), 2005, 911–920.

[48] M. Kivambe, G. Stokkan, T. Ervik, S. Castellanos, J. Hofstetter, and T. Buonassisi. *The Impact of Dislocation Structure on Impurity Decoration of Dislocation Clusters in Multicrystalline Silicon*. Solid State Phenom. **205-206**, 2013, 71–76.

[49] S. Castellanos, M. Kivambe, J. Hofstetter, M. Rinio, B. Lai, and T. Buonassisi. *Variation of dislocation etch-pit geometry: An indicator of bulk microstructure and recombination activity in multicrystalline silicon*. J. Appl. Phys. **115** (18), 2014, 183511.

[50] M. Ieong, B. Doris, J. Kedzierski, K. Rim, and M. Yang. *Silicon Device Scaling to the Sub-10-nm Regime*. en. Science **306** (5704), 2004, 2057–2060.

[51] T. Skotnicki. *Materials and device structures for sub-32 nm CMOS nodes*. Microelectron. Eng. **84** (9–10), 2007, 1845–1852.

[52] M. Seibt, R. Khalil, V. Kveder, and W. Schröter. *Electronic states at dislocations and metal silicide precipitates in crystalline silicon and their role in solar cell materials*. Appl. Phys. A **96** (1), 2009, 235–253.

[53] V. Kveder, M. Kittler, and W. Schröter. *Recombination activity of contaminated dislocations in silicon: A model describing electron-beam-induced current contrast behavior*. Phys. Rev. B **63** (11), 2001, 115208.

[54] K. Lauer, M. Herms, A. Grochocki, and J. Bollmann. *Iron Gettering at Slip Dislocations in Czochralski Silicon*. Solid State Phenom. **178-179**, 2011, 211–216.

[55] J. Lu, X. Yu, Y. Park, and G. Rozgonyi. *Investigation of iron impurity gettering at dislocations in a SiGe/Si heterostructure*. J. Appl. Phys. **105** (7), 2009, 73712.

[56] V. Naumann, D. Lausch, A. Graff, M. Werner, S. Swatek, J. Bauer, A. Hähnel, O. Breitenstein, S. Großer, J. Bagdahn, and C. Hagendorf. *The role of stacking faults for the formation of shunts during potential-induced degradation of crystalline Si solar cells*. Phys. Status Solidi RRL **7** (5), 2013, 315–318.

[57] O. Breitenstein, J. Bauer, and J. Rakotoniaina. *Material-induced shunts in multicrystalline silicon solar cells*. J. Semicond. **41** (4), 2007, 440–443.

[58] G. Ceder, Y.-M. Chiang, D. R. Sadoway, M. K. Aydinol, Y.-I. Jang, and B. Huang. *Identification of cathode materials for lithium batteries guided by first-principles calculations*. Nature **392** (6677), 1998, 694–696.

[59] D. D. Stefano, M. Mrovec, and C. Elsässer. *First-principles investigation of hydrogen trapping and diffusion at grain boundaries in nickel*. Acta Mater. **98**, 2015, 306 –312.

[60] A. Jain, S. P. Ong, G. Hautier, W. Chen, W. D. Richards, S. Dacek, S. Cholia, D. Gunter, D. Skinner, G. Ceder, and K. A. Persson. *Commentary: The Materials Project: A materials genome approach to accelerating materials innovation*. APL Materials **1** (1), 011002, 2013, –.

[61] R. M. Martin. *Electronic Structure: Basic Theory and Practical Methods*. 1st edition. Cambridge, UK ; New York: Cambridge University Press, 2008.

[62] P. Hohenberg and W. Kohn. *Inhomogeneous electron gas*. Phys. Rev. **136** (3B), 1964, B864.

[63] W. Kohn and L. J. Sham. *Self-consistent equations including exchange and correlation effects*. Phys. Rev. **140** (4A), 1965, A1133.

[64] J. P. Perdew and A. Zunger. *Self-interaction correction to density-functional approximations for many-electron systems*. Physical Review B **23** (10), 1981, 5048.

[65] J. P. Perdew, K. Burke, and M. Ernzerhof. *Generalized gradient approximation made simple*. Phys. Rev. Lett. **77** (18), 1996, 3865–3868.

[66] A. V. Krukau, O. A. Vydrov, A. F. Izmaylov, and G. E. Scuseria. *Influence of the exchange screening parameter on the performance of screened hybrid functionals*. The Journal of Chemical Physics **125** (22), 224106, 2006, –.

[67] R. P. Feynman. *Forces in molecules*. Physical Review **56** (4), 1939, 340.

[68] A. Fick. *Über Diffusion*. Ann. Phys. **170** (1), 1855, 59–86.

[69] D. A. Fick. *V. On liquid diffusion*. Philos. Mag. **10** (63), 1855, 30–39.

[70] A. Einstein. *Zur Theorie der Brownschen Bewegung*. Ann. Phys. **324** (2), 1906, 371–381.

[71] M. von Smoluchowski. *Zur kinetischen Theorie der Brownschen Molekularbewegung und der Suspensionen*. Ann. Phys. **326** (14), 1906, 756–780.

[72] G. H. Vineyard. *Frequency factors and isotope effects in solid state rate processes*. J. Phys. Chem. Solids. **3** (1), 1957, 121–127.

[73] P. Hänggi, P. Talkner, and M. Borkovec. *Reaction-rate theory: fifty years after Kramers*. Rev. Mod. Phys. **62** (2), 1990, 251.

[74] G. Henkelman, B. Uberuaga, and H. Jónsson. *A climbing image nudged elastic band method for finding saddle points and minimum energy paths*. J. Chem. Phys. **113**, 2000, 9901.

[75] G. Henkelman, G. Jóhannesson, and H. Jónsson. "Methods for Finding Saddle Points and Minimum Energy Paths". en. In: *Theoretical Methods in Condensed Phase Chemistry*. Ed. by S. D. Schwartz. Progress in Theoretical Chemistry and Physics 5. Springer Netherlands, 2002, 269–302.

[76] H. Monkhorst and J. Pack. *Special points for Brillouin-zone integrations*. Phys. Rev. B **13** (12), 1976, 5188–5192.

[77] A. Bortz, M. Kalos, and J. Lebowitz. *A new algorithm for Monte Carlo simulation of Ising spin systems*. J. Comput. Phys. **17** (1), 1975, 10 –18.

[78] D. T. Gillespie. *A general method for numerically simulating the stochastic time evolution of coupled chemical reactions*. J. Comput. Phys. **22** (4), 1976, 403 – 434.

[79] A. F. Voter. "Introduction to the kinetic Monte Carlo method". In: *Radiation Effects in Solids*. Springer, 2007, 1–23.

[80] Y. Du, J. Rogal, and R. Drautz. *Diffusion of hydrogen within idealized grains of bcc Fe: A kinetic Monte Carlo study*. Phys. Rev. B **86** (13), 17 2012, 174110.

[81] J. P. Dekker, C. A. Volkert, E. Arzt, and P. Gumbsch. *Alloying Effects on Electromigration Mass Transport*. Phys. Rev. Lett. **87** (4), 3 2001, 35901.

[82] K. A. Fichthorn and W. H. Weinberg. *Theoretical foundations of dynamical Monte Carlo simulations*. J. Chem. Phys. **95** (2), 1991, 1090–1096.

[83] M. Sanati, N. Gonzalez Szwacki, and S. Estreicher. *Interstitial Fe in Si and its interactions with hydrogen and shallow dopants*. Phys. Rev. B **76** (9), 12 2007, 125204.

[84] G. W. Ludwig and H. H. Woodbury. *Electronic Structure of Transition Metal Ions in a Tetrahedral Lattice*. Phys. Rev. Lett. **5** (3), 1960, 98–100.

[85] H. H. Woodbury and G. W. Ludwig. *Spin Resonance of Transition Metals in Silicon*. Phys. Rev. **117** (0), 1 1960, 102–108.

[86] M. Seibt, A. Sattler, C. Rudolf, O. Voß, V. Kveder, and W. Schröter. *Gettering in silicon photovoltaics: current state and future perspectives*. Phys. Status Solidi A **203** (4), 2006, 696–713.

[87] S. Narayanan, S. R. Wenham, and M. A. Green. *High efficiency polycrystalline silicon solar cells using phosphorus pretreatment*. Appl. Phys. Lett. **48** (13), 1986, 873–875.

[88] D. Abdelbarey, V. Kveder, W. Schröter, and M. Seibt. *Aluminum gettering of iron in silicon as a problem of the ternary phase diagram*. Appl. Phys. Lett. **94** (6), 2009, 61912.

[89] W. Seifert, O. Vyvenko, T. Arguirov, M. Kittler, M. Salome, M. Seibt, and M. Trushin. *Synchrotron-based investigation of iron precipitation in multicrystalline silicon*. Superlattices Microstruct. **45** (4–5), 2009, 168–176.

[90] T. Buonassisi, A. A. Istratov, M. Heuer, M. A. Marcus, R. Jonczyk, J. Isenberg, B. Lai, Z. Cai, S. Heald, W. Warta, R. Schindler, G. Willeke, and E. R. Weber. *Synchrotron-based investigations of the nature and impact of iron contamination in multicrystalline silicon solar cells*. J. Appl. Phys. **97** (7), 2005, 74901–074911.

[91] P. Gundel, M. C. Schubert, F. D. Heinz, W. Kwapil, W. Warta, G. Martinez-Criado, M. Reiche, and E. R. Weber. *Impact of stress on the recombination at metal precipitates in silicon*. J. Appl. Phys. **108** (10), 2010, 103707.

[92] J. Chen, T. Sekiguchi, and D. Yang. *Electron-beam-induced current study of grain boundaries in multicrystalline Si*. en. Phys. Status Solidi A **4** (8), 2007, 2908–2917.

[93] J. Chen, T. Sekiguchi, S. Nara, and D. Yang. *The characterization of high quality multicrystalline silicon by the electron beam induced current method*. en. J. Phys.: Condens. Matter **16** (2), 2004, S211.

[94] J. Chen, D. Yang, Z. Xi, and T. Sekiguchi. *Recombination activity of Σ3 boundaries in boron-doped multicrystalline silicon: Influence of iron contamination*. J. Appl. Phys. **97** (3), 2005, 33701–33701.

[95] J. Chen, T. Sekiguchi, R. Xie, P. Ahmet, T. Chikyo, D. Yang, S. Ito, and F. Yin. *Electron-beam-induced current study of small-angle grain boundaries in multicrystalline silicon*. Scripta Mater. **52** (12), 2005, 1211–1215.

[96] T. Buonassisi, A. A. Istratov, M. D. Pickett, M. A. Marcus, T. F. Ciszek, and E. R. Weber. *Metal precipitation at grain boundaries in silicon: Dependence on grain boundary character and dislocation decoration*. Appl. Phys. Lett. **89** (4), 2006, 42102–42103.

[97] M. C. Schubert, H. Habenicht, and W. Warta. *Imaging of metastable defects in silicon*. IEEE J. Photovolt. **1** (2), 2011, 168–173.

[98] J. Thibault, J.-L. Putaux, A. Jacques, A. George, and M. Elkajbaji. *Plasticity of a silicon bicrystal: a HREM study*. Microsc. Microanal. Microstruct. **1** (5-6), 1990, 395–404.

[99] N. Sakaguchi, H. Ichinose, and S. Watanabe. *Atomic structure of faceted Σ3 CSL grain boundary in silicon: HRTEM and Ab-initio calculation*. Mater. Trans., JIM **48** (10), 2007, 2585–2589.

[100] A. P. Sutton and R. W. Balluffi. *Interfaces in Crystalline Materials*. Oxford: Clarendon Press, 1995.

[101] M. Reiche, M. Kittler, M. Schmelz, R. Stolz, E. Pippel, H. Übensee, M. Kermann, and T. Ortlepp. *Single-electron transitions in one-dimensional native nanostructures*. en. J. Phys. Conf. Ser. **568** (5), 2014, 52024.

[102] M. Reiche, M. Kittler, H. Uebensee, E. Pippel, and W. Erfurth. *(Invited) Single Dislocations as Nanostructure Devices: Physics and Applications*. en. ECS Trans. **64** (11), 2014, 267–281.

[103] K. Hartman, M. Bertoni, J. Serdy, and T. Buonassisi. *Dislocation density reduction in multicrystalline silicon solar cell material by high temperature annealing*. Appl. Phys. Lett. **93** (12), 2008, 122108.

[104] H. Choi, M. Bertoni, J. Hofstetter, D. Fenning, D. Powell, S. Castellanos, and T. Buonassisi. *Dislocation Density Reduction During Impurity Gettering in Multicrystalline Silicon*. IEEE J. Photovoltaics **3** (1), 2013, 189–198.

[105] J. P. Hirth and J. Lothe. *Theory of Dislocations*. Englisch. Auflage: Reprint. Malabar, FL: Krieger Publishing Company, 1991.

[106] M. Seibt, D. Abdelbarey, V. Kveder, C. Rudolf, P. Saring, L. Stolze, and O. Voß. *Interaction of metal impurities with extended defects in crystalline silicon and its implications for gettering techniques used in photovoltaics*. Mater. Sci. Eng., B **159–160**, 2009, 264–268.

[107] R. Jones, P. R. Briddon, S. Öberg, A. T. Blumenau, and N. Fujita. *A Theoretical Study of Copper Contaminated Dislocations in Silicon*. Solid State Phenom. **131**, 2008, 259–264.

[108] J. Rabier, L. Pizzagalli, and J. Demenet. *Dislocations in silicon at high stress*. Dislocations in Solids **16**, 2010, 47–108.

[109] L. Pizzagalli, P. Beauchamp, and J. Rabier. *Undissociated screw dislocations in silicon: calculations of core structure and energy*. Philos. Mag. **83** (10), 2003, 1191–1204.

[110] C.-Z. Wang, J. Li, K.-M. Ho, and S. Yip. *Undissociated screw dislocation in Si: Glide or shuffle set?* Appl. Phys. Lett. **89** (5), 2006, 51910.

[111] A. Valladares and A. P. Sutton. *The equilibrium structures of the 90° partial dislocation in silicon*. en. J. Phys. Condens. Matter **17** (48), 2005, 7547.

[112] C.-y. Wang, Z.-q. Wang, Q.-y. Meng, C.-l. Li, and H.-w. Zheng. *Atomic simulation of the dynamic properties for a double period structure with 90° partial dislocation in Si*. Superlattices Microstruct. **50** (2), 2011, 157–163.

[113] H. Zhang. *Calculation of shuffle 60° dislocation width and Peierls barrier and stress for semiconductors silicon and germanium*. English. Eur. Phys. J. B **81** (2), 2011, 179–183.

[114] M. Matsubara, J. Godet, and L. Pizzagalli. *Theoretical study of hydrogen stability and aggregation in dislocation cores in silicon*. Phys. Rev. B **82** (2), 2010, 24107.

[115] M. Matsubara, J. Godet, and L. Pizzagalli. *Investigation of the interaction between hydrogen and screw dislocation in silicon by first-principles calculations*. en. J. Phys.: Condens. Matter **22** (3), 2010, 35803.

[116] A. Antonelli, J. F. Justo, and A. Fazzio. *Interaction of As impurities with 30° partial dislocations in Si: An ab initio investigation*. J. Appl. Phys. **91** (9), 2002, 5892–5895.

[117] A. Antonelli, J. F. Justo, and A. Fazzio. *Arsenic segregation, pairing and mobility on the cores of partial dislocations in silicon*. en. J. Phys.: Condens. Matter **14** (48), 2002, 12761.

[118] J. Zhang, C.-Z. Wang, and K.-M. Ho. *Finding the low-energy structures of Si[001] symmetric tilted grain boundaries with a genetic algorithm*. Phys. Rev. B **80** (17), 2009, 174102.

[119] T. Shi, Y. Li, Z. Ma, G. Qu, F. Hong, F. Xu, Y. Yan, and S.-H. Wei. *First-principles study of iron segregation into siliconon Σ5 grain boundary*. J. Appl. Phys. **107** (9), 2010, 93713.

[120] W. L. Huang, W. Ge, C. Li, C. Hou, X. Wang, and X. He. *Atomic and electronic structures of Si [001](130) symmetric tilt grain boundaries based on first-principles calculations*. Comput. Mater. Sci. **58**, 2012, 38–44.

[121] V. Y. Lazebnych and A. Mysovsky. *Theoretical modeling of the structure of tilt grain boundaries in crystalline silicon*. Phys. Solid State **54** (12), 2012, 2357–2361.

[122] V. Y. Lazebnykh and A. S. Mysovsky. *Local structure and defect segregation on the tilt grain boundaries in silicon*. arXiv preprint arXiv:1308.3802, 2013.

[123] M. Kohyama. *Computational studies of grain boundaries in covalent materials*. Modell. Simul. Mater. Sci. Eng. **10** (3), 2002, R31.

[124] A. Suvitha, N. S. Venkataramanan, R. Sahara, H. Mizuseki, and Y. Kawazoe. *First-Principles Calculations on Σ3 Grain Boundary Transition Metal Impurities in Multicrystalline Silicon*. Jpn. J. Appl. Phys. **49** (4S), 2010, 04DP02.

[125] S. K. Estreicher, M. Sanati, and N. Gonzalez Szwacki. *Iron in silicon: Interactions with radiation defects, carbon, and oxygen*. Phys. Rev. B **77** (9), 12 2008, 125214.

[126] V. Lazebnykh and A. Mysovsky. *Ab initio study of the distribution of point defects at grain boundaries in crystalline silicon*. English. JETP Lett. **98** (2), 2013, 76–79.

[127] C. B. Feng, J. L. Nie, X. T. Zu, M. M. Al-Jassim, and Y. Yan. *Structure and effects of vacancies in Σ3 (112) grain boundaries in Si*. J. Appl. Phys. **106** (11), 2009, 113506.

[128] J. Schön, H. Habenicht, W. Warta, and M. C. Schubert. *Chromium distribution in multicrystalline silicon: comparison of simulations and experiments*. Prog. Photovolt. Res. Appl. **21** (4), 2013, 676–680.

[129] J.-L. Maurice and C. Colliex. *Fast diffusers Cu and Ni as the origin of electrical activity in a silicon grain boundary*. Appl. Phys. Lett. **55** (3), 1989, 241–243.

[130] M. F. Chisholm, A. Maiti, S. J. Pennycook, and S. T. Pantelides. *Atomic configurations and energetics of arsenic impurities in a silicon grain boundary*. Phys. Rev. Lett. **81** (1), 1998, 132.

[131] M. M. Mandurah, K. C. Saraswat, C. R. Helms, and T. I. Kamins. *Dopant segregation in polycrystalline silicon*. J. Appl. Phys. **51** (11), 1980, 5755–5763.

[132] Y. Miyamura, H. Harada, S. Ito, J. Chen, and T. Sekiguchi. *Structural Study of Small Angle Grain Boundaries in Multicrystalline Si*. Mater. Sci. Forum **725**, 2012, 157–160.

[133] W. Read and W. Shockley. *Dislocation models of crystal grain boundaries*. Phys. Rev. **78** (3), 1950, 275.

[134] *Handbook of semiconductor silicon technology*. Noyes Publications, 1990.

[135] A. Jain, S. P. Ong, G. Hautier, W. Chen, W. D. Richards, S. Dacek, S. Cholia, D. Gunter, D. Skinner, G. Ceder, and K. A. Persson. *The Materials Project: A materials genome approach to accelerating materials innovation*. APL Materials **1** (1), 2013, 11002.

[136] M. A. Hopcroft, W. D. Nix, and T. W. Kenny. *What is the Young's Modulus of Silicon?* J. Microelectromech. Syst. **19** (2), 2010, 229–238.

[137] G. A. Baraff and M. Schlüter. *Migration of interstitials in silicon*. Phys. Rev. B **30** (6), 1984, 3460–3469.

[138] W. Frank, C. Elsässer, and M. Fähnle. *Ab initio Force-Constant Method for Phonon Dispersions in Alkali Metals*. Phys. Rev. Lett. **74** (10), 1995, 1791–1794.

[139] A. Togo, F. Oba, and I. Tanaka. *First-principles calculations of the ferroelastic transition between rutile-type and CaCl2-type SiO2 at high pressures*. Phys. Rev. B **78**, 13 2008, 134106.

[140] G. Kresse, J. Furthmüller, and J. Hafner. *Ab initio Force Constant Approach to Phonon Dispersion Relations of Diamond and Graphite*. en. Europhys. Lett. **32** (9), 1995, 729.

[141] W. Frank, U. Breier, C. Elsässer, and M. Fähnle. *First-Principles Calculations of Absolute Concentrations and Self-Diffusion Constants of Vacancies in Lithium*. Phys. Rev. Lett. **77** (3), 1996, 518–521.

[142] J. H. Westbrook and R. L. Fleischer, eds. *Intermetallic Compounds: Principles and Practice, Vol. 1: Principles*. 1st. Chichester ; New York: John Wiley and Sons Ltd, 1995.

[143] P. Schwalbach, S. Laubach, M. Hartick, E. Kankeleit, B. Keck, M. Menningen, and R. Sielemann. *Diffusion and isomer shift of interstitial iron in silicon observed via in-beam Mössbauer spectroscopy*. Phys. Rev. Lett. **64** (0), 11 1990, 1274–1277.

[144] D. Seif, G. Po, M. Mrovec, M. Lazar, C. Elsässer, and P. Gumbsch. *Atomistically enabled nonsingular anisotropic elastic representation of near-core dislocation stress fields in α-iron*. Phys. Rev. B **91** (11), 18 2015, 184102.

[145] J. Hornstra. *Dislocations in the diamond lattice*. J. Phys. Chem. Solids **5** (1), 1958, 129–141.

[146] M. Reiche, M. Kittler, W. Erfurth, E. Pippel, K. Sklarek, H. Blumtritt, A. Hähnel, and H. Übensee. *On the electronic properties of a single dislocation*. J. Appl. Phys. **115** (19), 2014, 194303.

[147] F. Liu, M. Mostoller, V. Milman, M. F. Chisholm, and T. Kaplan. *Electronic and elastic properties of edge dislocations in Si*. Phys. Rev. B **51** (23), 1995, 17192–17195.

[148] T. Kaplan, F. Liu, M. Mostoller, M. F. Chisholm, and V. Milman. *First-principles study of impurity segregation in edge dislocations in Si*. Phys. Rev. B **61** (3), 2000, 1674–1676.

[149] T.-L. Chan, D. West, and S. B. Zhang. *Limits on Passivating Defects in Semiconductors: The Case of Si Edge Dislocations*. Phys. Rev. Lett. **107** (3), 2011, 35503.

[150] E. Clouet, L. Ventelon, and F. Willaime. *Dislocation core energies and core fields from first principles*. Phys. Rev. Lett. **102** (5), 2009, 55502.

[151] W. Cai, V. V. Bulatob, J. Chang, J. Li, and S. Yip. *Periodic image effects in dislocation modelling*. Philos. Mag. **83** (5), 2003, 539–567.

[152] J. R. Chelikowsky. *30° Partial Dislocations in Silicon: Absence of Electrically Active States*. Phys. Rev. Lett. **49** (0), 21 1982, 1569–1572.

[153] J. Bennetto, R. W. Nunes, and D. Vanderbilt. *Period-Doubled Structure for the 90° Partial Dislocation in Silicon*. Phys. Rev. Lett. **79** (2), 1997, 245–248.

[154] W. H. Press. *Numerical recipes in Fortran 77: the art of scientific computing*. Vol. 1. Cambridge University Press, 1992.

[155] K. Wünstel and P. Wagner. *Interstitial iron and iron-acceptor pairs in silicon*. en. Appl. Phys. A **27** (4), 1982, 207–212.

[156] K. Nakashima and M. Chijiiwa. *Optical and Thermal Ionization of Iron-Related Defects in Silicon*. en. Jpn. J. Appl. Phys. **25** (2R), 1986, 234.

[157] O. O. Awadelkarim and B. Monemar. *A study of iron-related centers in heavily boron-doped silicon by deep-level transient spectroscopy*. J. Appl. Phys. **64** (11), 1988, 6306–6310.

[158] A. Rohatgi, J. R. Davis, R. H. Hopkins, P. Rai-Choudhury, P. G. McMullin, and J. R. McCormick. *Effect of titanium, copper and iron on silicon solar cells*. Solid-State Electron. **23** (5), 1980, 415–422.

[159] V. Kveder, V. I. Orlov, M. Khorosheva, and M. Seibt. *Influence of the Dislocation Travel Distance on the DLTS Spectra of Dislocations in Cz-Si*. Solid State Phenom. **131-133**, 2008, 175–182.

[160] A. Castaldini, D. Cavalcoli, A. Cavallini, and S. Pizzini. *Experimental Evidence of Dislocation Related Shallow States in p-Type Si*. Phys. Rev. Lett. **95** (7), 2005, 76401.

[161] M. Legros, G. Dehm, E. Arzt, and T. J. Balk. *Observation of Giant Diffusivity Along Dislocation Cores*. en. Science **319** (5870), 2008, 1646–1649.

[162] O. Breitenstein, J. Bauer, K. Bothe, W. Kwapil, D. Lausch, U. Rau, J. Schmidt, M. Schneemann, M. C. Schubert, J.-M. Wagner, et al. *Understanding junction breakdown in multicrystalline solar cells*. J. Appl. Phys. **109** (7), 2011, 71101–71101.

[163] S. Koch, D. Nieschalk, J. Berghold, S. Wendlandt, S. Krauter, and P. Grunow. "Potential Induced Degradation Effects on Crystalline Silicon Cells with Various Antireflective Coatings". In: *27th European Photovoltaic Solar Energy Conference, Frankfurt, Germany*. 2012, 1985–1990.

[164] P. Hacke, K. Terwilliger, R. Smith, S. Glick, J. Pankow, M. Kempe, S. K. I. Bennett, and M. Kloos. "System voltage potential-induced degradation mechanisms in PV modules and methods for test". In: *Photovoltaic Specialists Conference (PVSC), 2011 37th IEEE*. 2011, 814–820.

[165] J. Bauer, V. Naumann, S. Großer, C. Hagendorf, M. Schütze, and O. Breitenstein. *On the mechanism of potential-induced degradation in crystalline silicon solar cells*. Phys. Status Solidi RRL **6** (8), 2012, 331–333.

[166] E. Aerts, P. Delavignette, R. Siems, and S. Amelinckx. *Stacking fault energy in silicon*. J. Appl. Phys. **33** (10), 1962, 3078–3080.

[167] H. Föll and C. Carter. *Direct TEM determination of intrinsic and extrinsic stacking fault energies of silicon*. Philos. Mag. A **40** (4), 1979, 497–510.

[168] Y.-M. Juan and E. Kaxiras. *Generalized stacking fault energy surfaces and dislocation properties of silicon: a first-principles theoretical study*. Philos. Mag. A **74** (6), 1996, 1367–1384.

[169] R. Shannon. *Revised effective ionic radii and systematic studies of interatomic distances in halides and chalcogenides*. Acta Crystallogr. Sect. A **32** (5), 1976, 751–767.

[170] V. Naumann, D. Lausch, K. Ilse, O. Breitenstein, J. Bauer, S. Großer, J. Bagdahn, and C. Hagendorf. *PID-shunting: Understanding from nanoscale to module level*. 2014.

[171] M. Schutze, M. Junghanel, M. Koentopp, S. Cwikla, S. Friedrich, J. Muller, and P. Wawer. "Laboratory study of potential induced degradation of silicon photovoltaic modules". In: *Photovoltaic Specialists Conference (PVSC), 2011 37th IEEE*. IEEE. 2011, 821–826.

[172] V. Naumann, K. Ilse, and C. Hagendorf. "On the discrepancy between leakage currents and potential-induced degradation of crystalline silicon modules". In: *Proc. 28th EU PVSEC 2013*. 2013, 2994–2997.

[173] J. Chen and A. Milnes. *Energy levels in silicon*. Annu. Rev. Mater. Sci. **10** (1), 1980, 157–228.

[174] A. Urban, M. Reese, M. Mrovec, C. Elsässer, and B. Meyer. *Parameterization of tight-binding models from density functional theory calculations*. Phys. Rev. B **84** (15), 2011, 155119.

[175] C. Freysoldt, B. Grabowski, T. Hickel, J. Neugebauer, G. Kresse, A. Janotti, and C. G. Van de Walle. *First-principles calculations for point defects in solids*. Rev. Mod. Phys. **86** (1), 2014, 253.

[176] J. Schön, F. Schindler, W. Kwapil, M. Knörlein, P. Krenckel, S. Riepe, W. Warta, and M. Schubert. *Identification of the most relevant metal impurities in mc n-type silicon for solar cells*. Sol. Energy Mater. Sol. Cells, 2015.

[177] L. Bengtsson. *Dipole correction for surface supercell calculations*. Phys. Rev. B **59** (19), 1999, 12301.

[178] P. Giannozzi, S. Baroni, N. Bonini, M. Calandra, R. Car, C. Cavazzoni, D. Ceresoli, G. L. Chiarotti, M. Cococcioni, I. Dabo, A. D. Corso, S. de Gironcoli, S. Fabris, G. Fratesi, R. Gebauer, U. Gerstmann, C. Gougoussis, A. Kokalj, M. Lazzeri, L. Martin-Samos, N. Marzari, F. Mauri, R. Mazzarello, S. Paolini, A. Pasquarello, L. Paulatto, C. Sbraccia, S. Scandolo, G. Sclauzero, A. P. Seitsonen, A. Smogunov, P. Umari, and R. M. Wentzcovitch. *QUANTUM ESPRESSO: a modular and open-source software project for quantum simulations of materials*. J. Phys.: Condens. Matter **21** (39), 2009, 395502.

[179] D. Vanderbilt. *Soft self-consistent pseudopotentials in a generalized eigenvalue formalism*. Phys. Rev. B **41** (11), 1990, 7892.

[180] J. M. Soler, E. Artacho, J. D. Gale, A. García, J. Junquera, P. Ordejón, and D. Sánchez-Portal. *The SIESTA method for ab initio order-N materials simulation*. en. J. Phys.: Condens. Matter **14** (11), 2002, 2745.

[181] N. Troullier and J. L. Martins. *Efficient pseudopotentials for plane-wave calculations*. Phys. Rev. B **43** (3), 1991, 1993.

[182] S. R. Bahn and K. W. Jacobsen. *An object-oriented scripting interface to a legacy electronic structure code*. English. Comput. Sci. Eng. **4** (3), 2002, 56–66.

[183] *Python Language Reference*. Python Software Foundation. URL: `http://www.python.org`.

[184] S. Behnel, R. Bradshaw, L. Dalcín, M. Florisson, V. Makarov, and D. S. Seljebotn. *Cython*. URL: `http://www.cython.org`.

Acknowledgments

First of all I would like to thank my two advisers, Christian Elsässer and Peter Gumbsch, for the personal support and for the scientific exchange which made this thesis possible. During my time at the Fraunhofer IWM I also crucially benefited from scientific discussion with Matous Mrovec and Francesco Colonna. I also highly appreciated the work on the battery project with Britta Lang and the countless hours we spent to work on a project proposal together with Francesco.

My Nerf-Gun fights with Davide Di Stefano (thanks for proofreading) and Nathalia Bedoya-Martínez on Friday afternoons will never be forgotten. Thanks to a lot of people here, the atmosphere in the office was always warm and welcoming, this includes Gianpietro Moras (for always spending his coffee break in our offices with his incredible positive look on the world, kind of), Daniel Urban (for performing the best song of the institute ♫), Wolfgang Körner (for eating tons of pastries the whole day), Georg Krugel (for endless writing of magnet proposals), Jamel Khamassi (for always sharing a room at the DD-seminar), Kerstin Falk (for always being hungry at 12 o'clock), Pedro Romero (for showing me that the real Mexican burrito has its origin in Hamburg), Lars Pastewka (for taking care of my old desk buddy), Davide Di Stefano (No, we are not married!), Andreas Klemenz (sorry for spoiling your PhD hat with too much super glue), Anke Peguiron (for keep trying to invite me to choir concerts), Nils Beckmann (for introducing me to the most complicated board game in my life), Leonhard Mayrhofer (for making me feel bad buying an Ikea kitchen instead of carpentering it myself), Julian von Lautz (for drinking someone else's Bierschnaps without knowing), Dariush Seif (for deciding whose pronunciation is correct), сушки (for feeding me during my time of writing), and many others which are too many to list here.

Thanks to my mom for believing in me since 27 years. Above all that I would like to thank Anna-Lena for the constant support and encouragement that helped me to write this thesis.

The financial support by the Hans L. Merkle foundation is highly acknowledged. Moreover, the work of the thesis would have been impossible without the computational resources of the Steinbuch Centre for Computing at the KIT, coffee machines, and a variety of different scientific software packages including Quantum Espresso, Siesta, Atomic Simulation Environment, VESTA, atomeye, Phonopy, Scipy/Numpy, matplotlib, and LaTeX.